DISSERTATION

FABRICATION AND ANALYSIS OF VANADIUM OXIDES AND VANADIUM OXIDE BASED MAGNETIC HYBRID STRUCTURES

Submitted by

Logan Sutton

Department of Physics

In partial fulfillment of the requirements

For the Degree of Doctor of Philosophy

Colorado State University

Fort Collins, Colorado

Spring 2021

Doctoral Committee:

Advisor: Mingzhong Wu

Jose de la Venta Granda
Kathryn Ross
Amy Prieto

ABSTRACT

FABRICATION AND ANALYSIS OF VANADIUM OXIDES AND VANADIUM OXIDE BASED MAGNETIC HYBRID STRUCTURES

Vanadium oxide films and vanadium oxide-based magnetic hybrid structures are fabricated using various techniques and studied optically, electrically, structurally, and magnetically for their potential applications into magnetic recording, room temperature refrigeration, and optical switches. The different types of behavior seen in the transitions of the vanadium oxide class of compounds can be altered and optimized according to desirable qualities for these applications.

Several different techniques were used for the fabrication of vanadium oxide-ferromagnetic (FM) composites with the goal of causing magnetic coupling and the optimization of coupling between the vanadium oxide compound and the FM compound. The ball milling process was used as the primary step in formation of the composites, but was shown to be ineffective at causing coupling between the compounds if used alone. The addition of a sintering process was shown to successfully couple V_2O_3 and Ni, with an optimization of the process determined to be primarily dependent on temperature. Optimized composites showed up to 56% changes in coercivity at the transition temperature of the V_2O_3. VO_2 based composites were unable to be coupled due to problems with the reduction and oxidation of the compounds involved, and a lack of diffusion.

A sol-gel technique for the fabrication of VO_2 layers was optimized for large transitional properties and refined for reproducibility. Magnetic hybrid structures formed from the sol-gel

fabricated films were shown to have comparable properties to their sputtered counterparts. W doped films fabricated using the sol-gel technique, when compared to doping using a sputtering technique, were demonstrated to allow for larger control over the ideal doping range. Doping was shown to have negligible effect on the morphology of the films, but produced several W based impurities. Although doping produced expected shifts and decreases in the transitional electrical transport properties, there were also unexplained shifts in the absolute resistance for higher doping. Magnetic hybrid structures based on doped films still produced large changes in the magnetic properties of the FM layer, but these changes were shifted to lower temperatures and reduced.

Transmission and reflection of VO_2 films fabricated using different techniques were shown to have different qualitative and quantitative behaviors at different optical wavelengths of incidence. Most films were shown to have downward switching in both the transmission and reflection at the transition, however thinner films sometimes showed upward switching in the transmission. Downward bumps caused by interference were seen in the reflection at 980 nm, as well as at 635 nm for two other films. The model that was developed to try to reproduce this behavior is successful for 60% of the films, and able to reproduce all of the qualitative behaviors described. However the trends in the fitted refractive index do not help elucidate what physical mechanism is responsible for the differences seen between samples.

ACKNOWLEDGEMENTS

First and foremost, I would like to thank my advisor Prof. Jose de la Venta Granda. It was his guidance and patience that allowed me to attain my research goals so efficiently. Allowing me the freedom to make mistakes, while providing guidance when necessary, was the main driving force in my growth as a researcher throughout grad school.

I would next like to thank the members of my committee: Prof. Kathryn Ross, Prof. Mingzhong Wu, and Prof. Amy Prieto, not only for providing valuable questions and suggestions while on my committee, but also for facilitating my research projects through use of equipment and other resources. Thanks to my lab mate Josh Lauzier for always lending a helping hand when I needed it, and for providing me with some very good suggestions on my research. Thanks to all of the other professors, fellow graduate students, postdocs, researchers, and technical staff that provided me with help and resources throughout my research, with a special thanks to: Brian Newell, Pat McCurdy, Roy Geiss, Jamie Nielson, Annalise Maughan, Ramesh Pandey, Emmet Randel, Jesse Brown, Kerry Neal, Tao Liu, Matt Ballinger, Martin Gelfand, Jacob Schneider, Chris Rom, Meenakshi Singh, Kellen Malone, Peng Li, Weston Maughan, Jinjun Ding, August Demann, and Robert Adame.

Finally, I would like to thank my family for all of the love and support they have provided over the years.

TABLE OF CONTENTS

ABSTRACT ii
ACKNOWLEDGEMENTS iv
Chapter 1. Introduction 1
1.1 Vanadium Oxides 1
1.2 Metal to Insulator and Structural Phase Transitions in Vanadium Oxides 4
1.2.1 Vanadium Sesquioxide (V_2O_3) 7
1.2.2 Vanadium Dioxide (VO_2) 13
1.3 Optical Transition in VO_2 19
1.4 W Doping in VO_2 22
1.5 Magnetic Hybrid Structures 25
1.6 Magnetostriction and Inverse Magnetostriction 28
Chapter 2. Fabrication and Characterization Techniques 33
2.1 Introduction 33
2.2 Ball Milling 35
2.3 Annealing and Sintering 38
2.4 Sol-gel Synthesis 40
2.5 Thin Film Deposition 42
2.6 DC Electrical Transport Measurements 46
2.7 X-ray Diffraction 49
2.8 Electron Microscopy Techniques 56
2.8.1 Scanning Electron Microscopy 56
2.8.2 Energy Dispersive X-ray Spectroscopy 61
2.9 Profilometry 62
2.9.1 Stylus Profilometry 62
2.9.2 Atomic Force Microscopy 62
2.10 Magnetometry 65
2.10.1 Vibrating Sample Magnetometry 66
2.10.2 Superconducting Quantum Interference Device Based Magnetometry 69
2.11 Optical Wavelength Reflectometry 71
Chapter 3. Magnetic Properties of Hybrid Vanadium Oxide/FM Composites 75

3.1 Motivation 75
3.2 Milling of VO_2 and $CoFe_2O_4$ 76
3.3 Sintering of Vanadium Oxide Composites as a Fabrication Technique for VO_2/Ni 83
3.4 Fabrication of V_2O_3/Ni Composites and Optimization of Magnetic Coupling 88
3.5 Conclusions 100
Chapter 4. Effects of W Doping in VO_2 on the Magnetic Properties of Sol-gel Synthesized VO_2/Ni Heterostructures 102
4.1 Introduction to Fabrication Techniques and Goals 102
4.2 Sol-gel Synthesis of VO_2 films and Use in Fabrication of VO_2/Ni Bilayers 104
4.3 W Doping Using Both Sol-gel and Sputtering Techniques 116
4.4 Magnetic Measurements of W Doped VO_2/Ni Heterostructures 126
4.5 Conclusions 130
Chapter 5. Optical Properties of VO_2 133
5.1 Motivation 133
5.2 Transmission and Reflection From VO_2 Films 134
5.3 Modeling VO_2 Optical Transition For R and T 146
5.4 Comparison of Data and Model 156
5.5 Conclusions 164
Chapter 6. Summary 166
6.1 Summary of Results 166
6.2 Outlook 167
References 169
Appendix 176

Chapter 1. Introduction

1.1 Vanadium Oxides

The transition metal oxides are an important class of compounds due to their large variety of physical and chemical properties, along with their high potential for being tuned to exhibit specific effects.[1–3] There are many famous examples of these compounds exhibiting useful and unique properties. The discovery of high temperature superconductivity in cuprates lead to an entire dedicated field of study in modern day condensed matter physics. Magnanites have shown both colossal magnetoresistance and impressive catalytic activity.[4,5] Beyond this, transition metal oxides have shown promise in the areas of resistive memory devices and photocatalysis,[6–8] many have been shown to be multiferroic[9] and have different forms of ferroic order,[10] with others showing exotic types such as ferroelasticity and ferroelectricity.[11,12] These are strongly electron-electron correlated systems most of the time, making the exact physical mechanisms behind these phenomena complex and difficult to explain. Other interesting phenomena many of such compounds have are phase transitions, with effects that may be structural,[13,14] electronic,[13,15] optical[16] and or magnetic[17,18] in nature. It is also possible that the changes in these properties may be coupled through the transition.

There has been much interest in the vanadium oxide family of materials specifically, due to their well-studied and varied transitions that occur across a wide range of operating conditions. These transitions can be driven by temperature,[13] voltage,[19–21] current, [22–24] electromagnetic waves, [25,26] stress,[27,28] etc., and have a wide degree of tunability, making them ideal for a multitude of technological applications. Some of these applications have included

electrical and optical switching devices,[29,30] medical implants,[31,32] infrared modulators,[33] light detectors,[34] and temperature sensors.[35,36]

The vanadium oxide family has a large variety of physical and chemical states, one of the reasons that they are able to have the varied properties described above. There are two interrelated aspects of the vanadium oxide family which allow them to have such variation. First, the formal oxidation states of vanadium oxide can vary across +2 to +5. And second, ions show several different types of coordination geometries: tetrahedra, octahedra, square pyramids, or pentagonal bipyramids. The compounds in the family can also have both single and multiple valency states, as well as mixed valence states. In this thesis we will mainly be concerned with compounds that have single valence states, specifically V_2O_3 and VO_2, however we will briefly discuss other compounds in the family. Figure 1.1 shows a phase diagram of several of the more common oxidation states. This multitude of different oxidation states and crystal structures makes it challenging to fabricate pure phases of any given vanadium oxide, as there will more than likely either be contamination from either another oxide phase, or a different crystal phase. This will be discussed with more specific details in later sections. One of the main trends seen in the fabrication process is that when most vanadium oxides are exposed to air they undergo oxidation, which means that over time samples prefer to oxidize to the more stable V_2O_5 state. Similarly, under reduction processes, vanadium oxides prefer to reduce to the more stable V_2O_3 state.

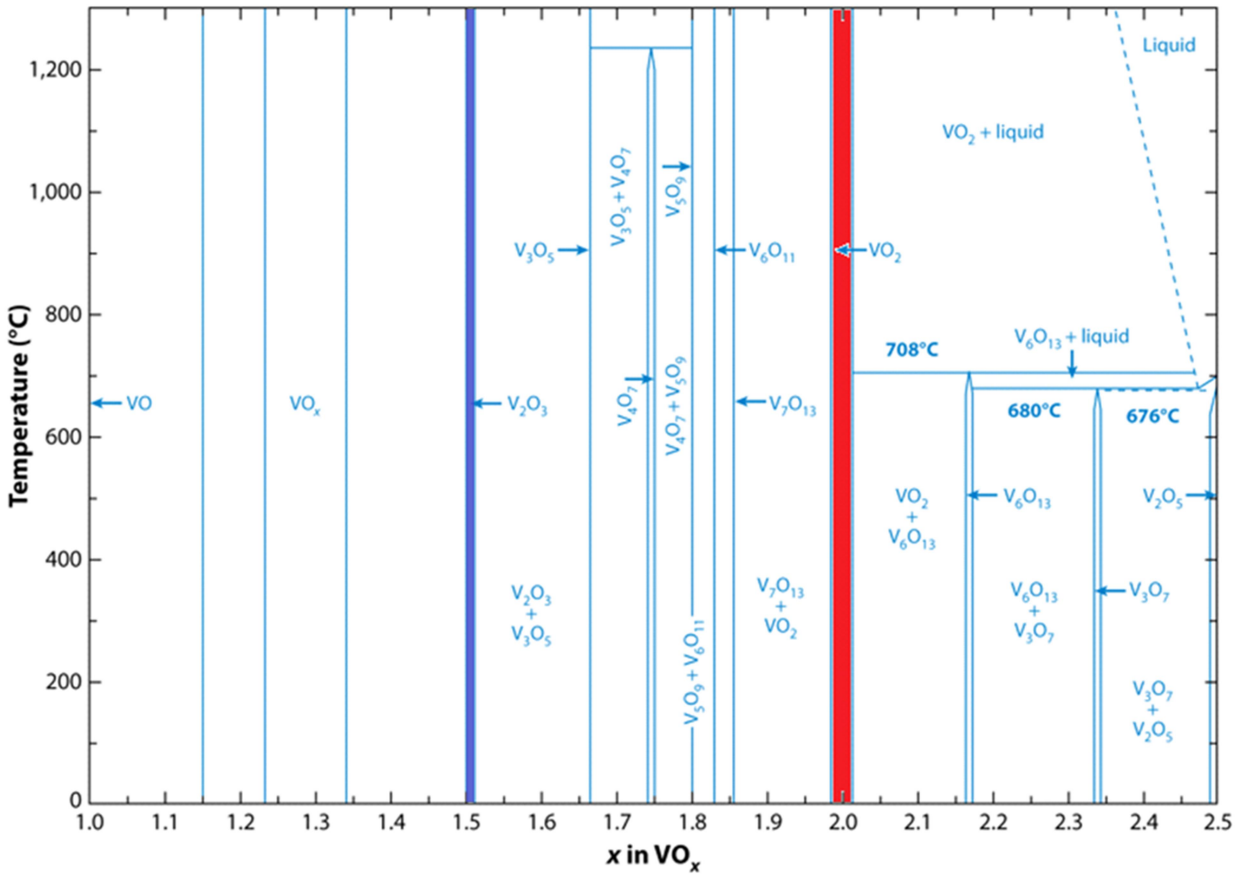

Figure 1.1. Vanadium oxide phase diagram with temperature as a function of oxygen concentration. VO_2 region highlighted in red, V_2O_3 region highlighted in blue. Modified from [37].

The single valence states of vanadium oxide are VO, V_2O_3, VO_2, and V_2O_5, which all share a common octahedral VO_6 unit cell. Different structures arise from the distortion of this unit cell and differences in the connectivity of the units. Monoxide VO forms a cubic rocksalt lattice, sesquioxide V_2O_3 forms a monoclinic crystal lattice below 150 K and has a rhombohedral phase above this temperature, dioxide VO_2 forms a monoclinic lattice below 340K and has a rutile phase above this temperature, and V_2O_5 forms an orthorhombic lattice.

Mixed valence states can be categorized into different homogulous series, the more common and well-studied of such being the Magnéli phases. Magnéli phases can be represented by a stoichiometric formula V_nO_{2n-1}(or V_nO_{2n+1})[38,39], which can be more generally written as

$$V_nO_{2n-1} = V_2O_3 + (n-2)VO_2, \text{ where } 2 \leq n \leq 9$$

As is clear from the above equation, these represent oxides between V_2O_3 and VO_2. For n = 9 it forms a compound which is only metastable, while n > 9 has not been seen in any studies and is considered theoretically unlikely.[40] Compounds in this series have many related properties, such as often having metal to insulator transitions and sharing many chemical properties. The crystal structures of these compounds can be formed from blocks of the rutile VO_2 structure and the V_2O_3 corundum structure.[41] Another homogulous series, although less studied, are known as the Wadsley phases.[42] These are given by the stoichiometric formula $V_{2n}O_{5n-2}$, where n > 2, and represents oxides between VO_2 and V_2O_5. Many studies have reported fractional valence charges, but are generally actually mixes of these various phases.[43,44]

1.2 Metal to Insulator and Structural Phase Transitions in Vanadium Oxides

As stated in the previous section, one of the most striking qualities of the vanadium oxide family of compounds is the prevalence of metal to insulator transitions in many of the compounds at a variety of different temperatures. Figure 1.2 illustrates this very well, showing many of the vanadium oxides known to have phase transitions and their respective transition temperatures, as compared to other compounds with phase transitions. Morin was the first to discover the metal to insulator transition (MIT) in vanadium oxides over 60 years ago.[45] Vanadium oxide MITs are always concurrent to a structural phase transition (SPT), since they are first order phase transitions. There is still debate over the exact nature of the relationship between the MIT and the SPT, with different compounds having different mechanisms and relationships behind these phenomena. We will discuss these relationships and mechanisms in more detail for the specific compounds of interest below.

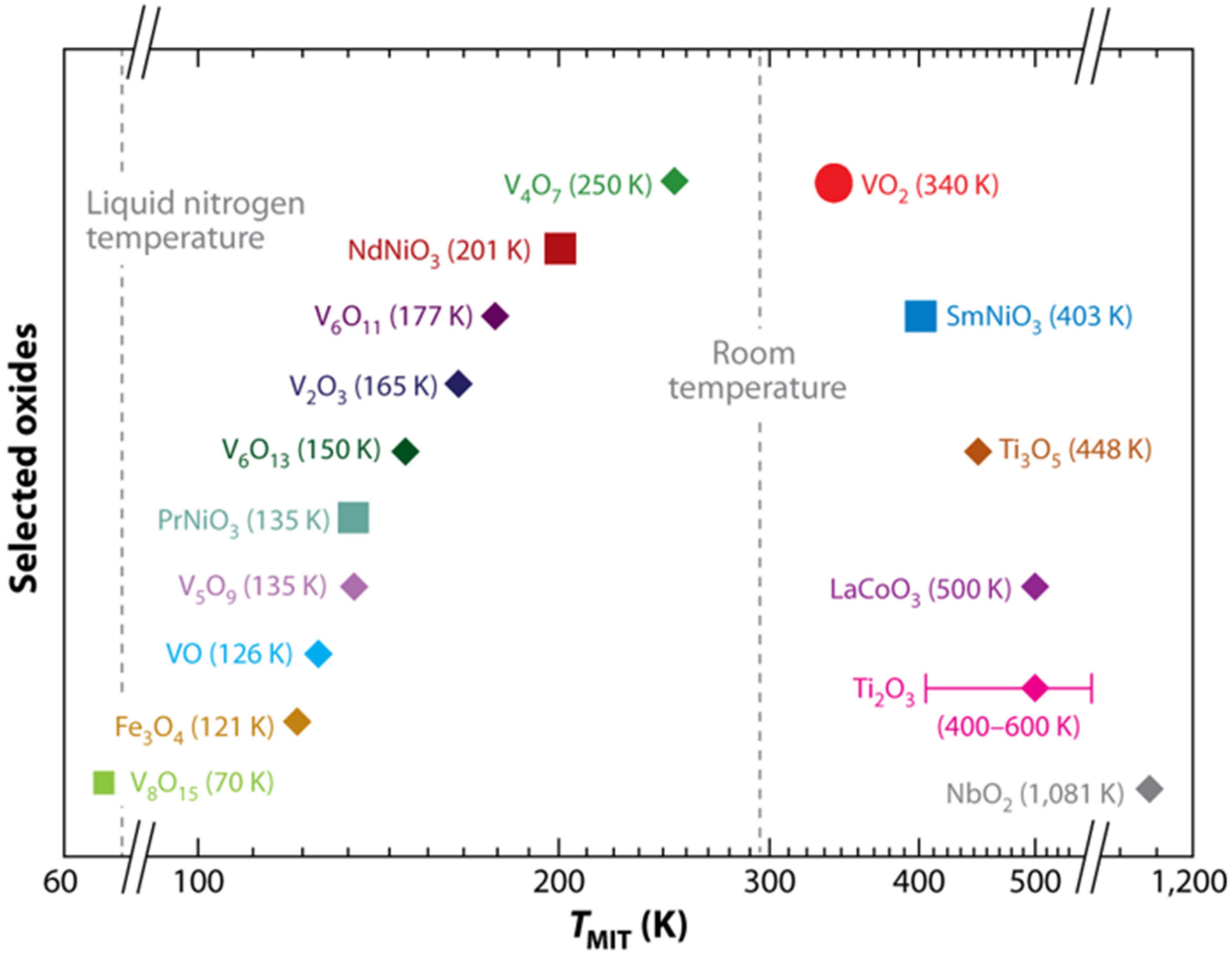

Figure 1.2. Critical temperatures for various oxides' MIT's. Dashed lines represent liquid nitrogen and room temperature. Y-axis is arbitrary increments. Reprinted from [46].

As shown in Figure 1.2 and Figure 1.3, the MITs of the various vanadium oxides span across a variety of different temperature ranges and have different magnitudes of change in resistivity associated with them. It is clear from Figure 1.3 that two of these compounds, V_2O_3 and VO_2, stand out from the rest. V_2O_3 has the largest magnitude of change in resistivity MIT of the vanadium oxides (with a change in resistivity of around 7-10 orders of magnitude), and is one of the most well studied due to this and its ease of fabrication without phase impurities in comparison to most of the vanadium oxides. VO_2 has the transition temperature which is closest to room temperature at 340K, making it the most ideal for applications, as well as one of the

most well-studied of the vanadium oxides. The magnitude of its transition is also relatively large (around 5 orders of magnitude resistivity change). This thesis shall primarily focus on structures made with one of these two compounds, and so further discussion of vanadium oxides shall be limited to them.

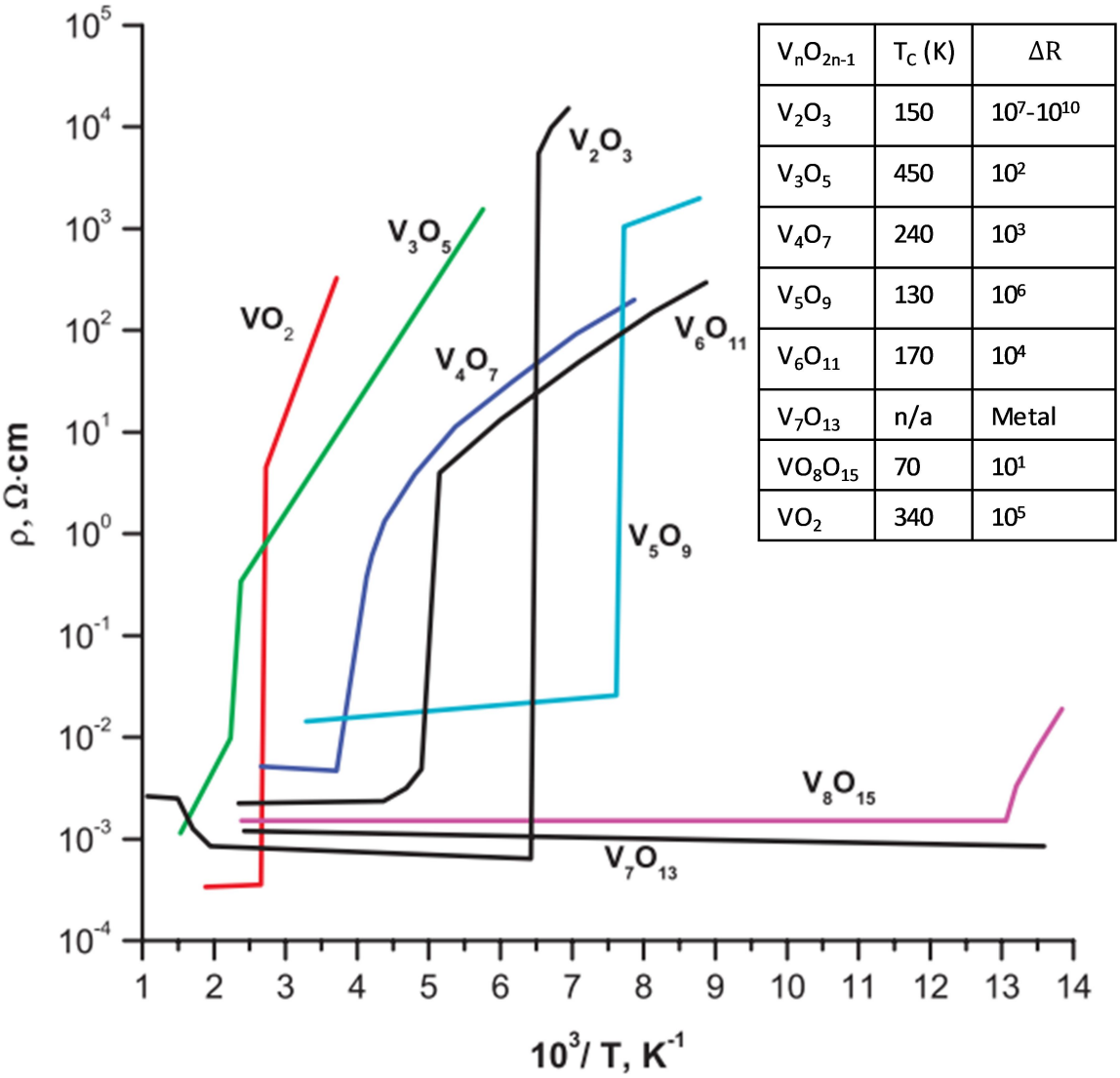

V_nO_{2n-1}	T_C (K)	ΔR
V_2O_3	150	10^7-10^{10}
V_3O_5	450	10^2
V_4O_7	240	10^3
V_5O_9	130	10^6
V_6O_{11}	170	10^4
V_7O_{13}	n/a	Metal
VO_8O_{15}	70	10^1
VO_2	340	10^5

Figure 1.3. Resistivity as a function of inverse temperature for several vanadium oxides. Inset shows critical temperature and size for the associated MIT. Figure modified from [47–49].

1.2.1 Vanadium Sesquioxide (V_2O_3)

V_2O_3's phase transition occurs around 150 – 165 K, with a 7 – 8 K thermal hysteresis. Below the transition temperature it is an insulating material and above it is a conducting material, with a change in resistance of up to 10 orders of magnitude depending on the fabrication technique. As shown in Figure 1.4, it goes from a low temperature monoclinic state to a high temperature rhombohedral state. This SPT/MIT also has a magnetic transition concurrent with it, going from a low temperature antiferromagnetic (AF) phase into a paramagnetic (PM) phase above the transition temperature. An example of the MIT in a thin film sample is shown in Figure 1.5. This transition is well known to be a Mott-Hubbard transition, and is considered to be a rare case of a perfect Mott insulator.

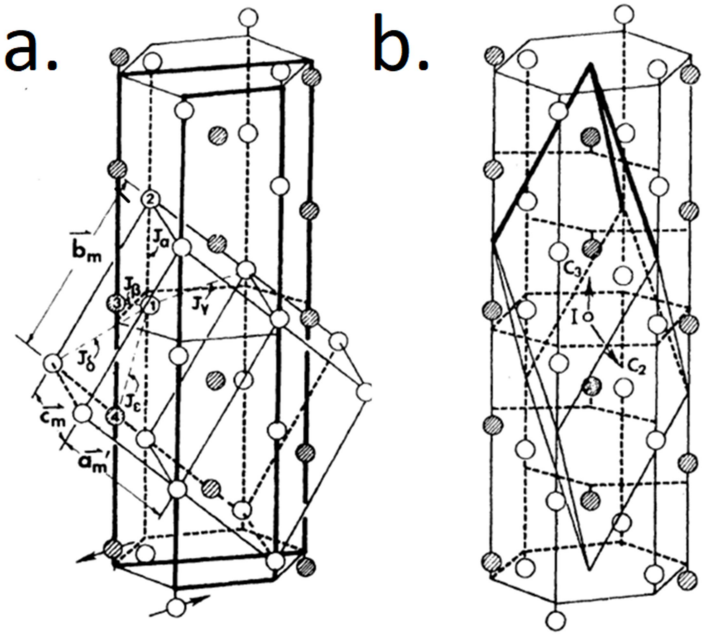

Figure 1.4. Crystal structure of V_2O_3. a. Low temperature monoclinic structure **b.** High temperature rhombohedral structure. Adapted from [50].

A Mott insulator is a type of insulator which, if traditional band theory applied, would be a conductor. However Mott insulators are strongly correlated systems, meaning that the Coulomb

repulsion between the electrons will contribute to the potential energy of the system, causing a splitting of the band gap. A Mott-Hubbard transition is a transition based on these electron-electron correlation effects. Put simply, it is a transition in a material from a strongly correlated metal to a Mott insulator. This occurs due to a change in the potential energy from added electron correlation, where the exact nature of these correlation effects changing can be exceedingly complicated. At its simplest, a change in energy per electron site due to temperature can cause the electron correlation effects to become strong enough to cause the transition. However, these transitions may occur in many other situations, and a full model describing these transitions often requires very complicated techniques such as Dynamic Mean Field Theory (DMFT) and/or Density Functional Theory (DFT) techniques.

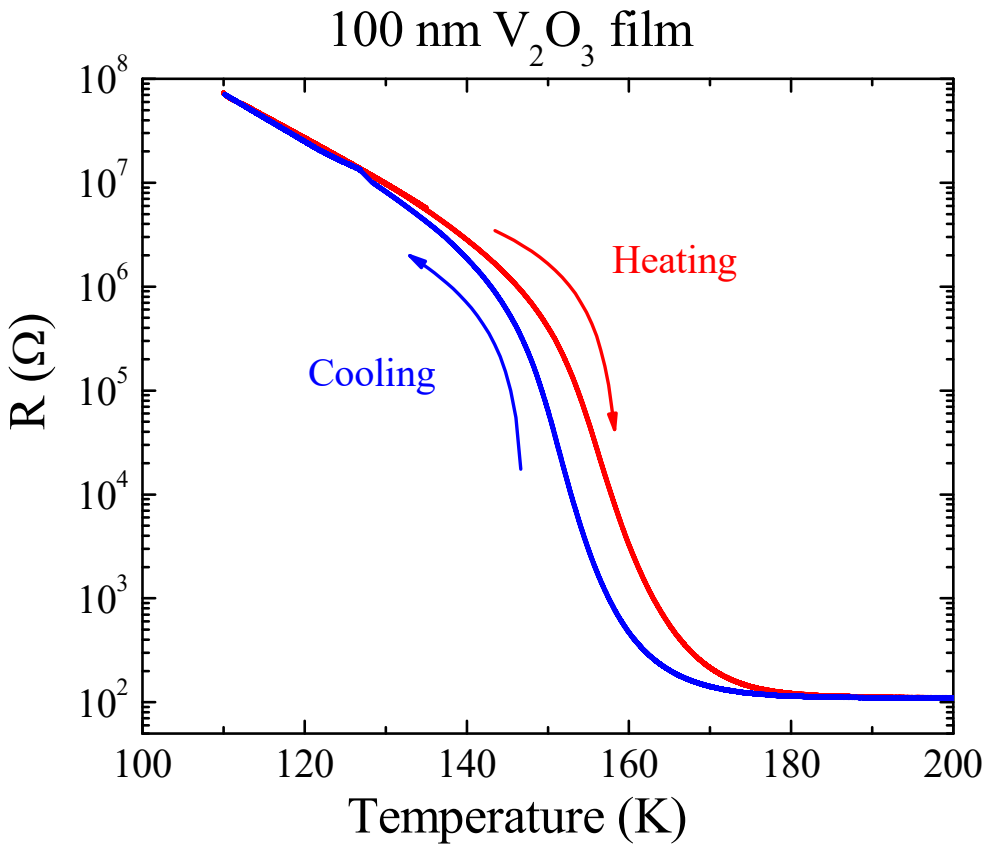

Figure 1.5. MIT of V_2O_3 in 100 nm film. Large resistance drop over ~30 K with ~8 K thermal hysteresis. Adapted from [51].

Generally, the theory behind V_2O_3's specific Mott transition is understood as follows. The electronic configuration of atomic vanadium is $[Ar]3d^34s^2$, so for V_2O_3, which has a +3-oxidation state, the vanadium is in the $3d^2$ configuration. When in the corundum phase, oxygen ligands coordinate the vanadium atoms in a trigonally distorted octahedral manner. The cubic part of the crystal field splits these d states into a higher energy e_g state and a lower energy t_{2g} state. The distortion effectively causes a compression along one of the octahedral axes, and so the t_{2g} states degeneracy is lifted and the states are split into an a_{1g} state and lower energy degenerate $e_{\pi g}$ states. Figure 1.6 illustrates the splitting of these electron states. Specific occupation of these t_{2g} states by the 2 d electrons is extremely important in understanding the

MIT, but the discussion required for such is beyond the scope of this thesis. The discussion centers around the fact that simpler models that assume strong V-V hybridization predict strong bonding-antibonding splitting of the a_{1g} state, in turn implying the degenerate $e_{\pi g}$ state contains only 1 electron. This would correspond to a quarter filled S = ½ Hubbard model. Experimental evidence,[52,53] however, suggests the electron occupation is a mix of the two levels in an S = 1 state. More advanced LDA models, DMFT models, and hybrid LDA-DMFT models have to be used to attain a more accurate picture of the system.

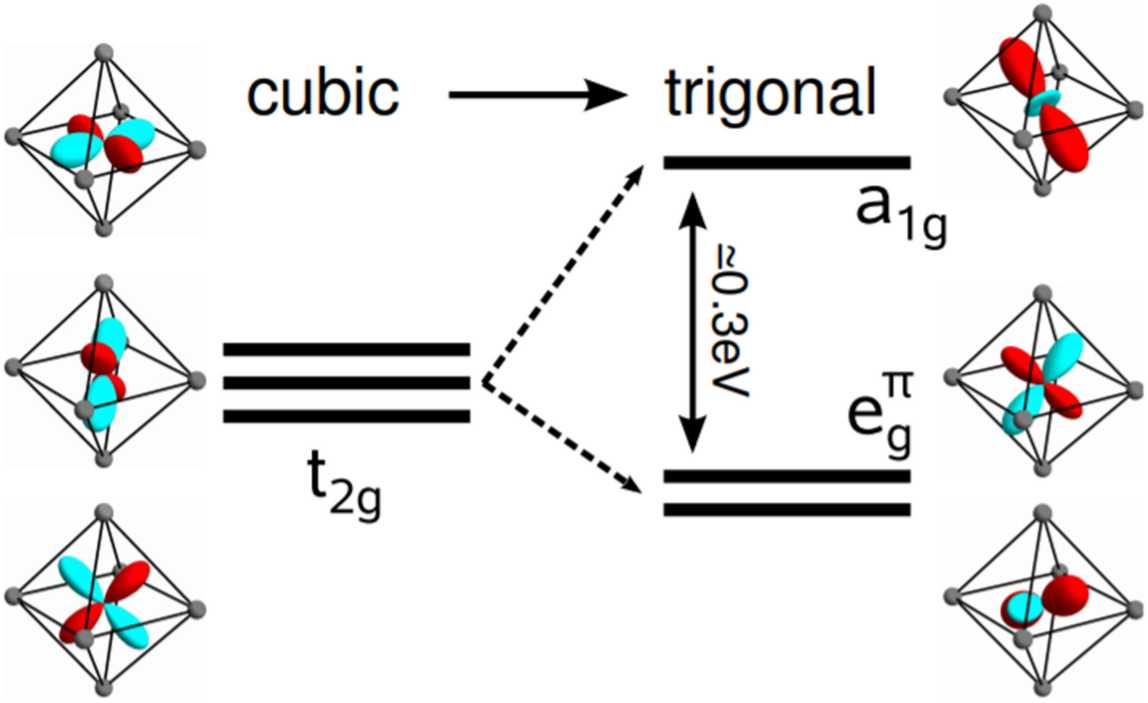

Figure 1.6. Splitting of electron states in V_2O_3. Left are the relevant energy states of the cubic structure and right are the relevant energy states of the trigonal structure. The states split into a single higher energy state and 2 lower energy states with a 0.3 eV gap. Adapted from [54].

Although for a long time V_2O_3 had been considered an ideal Mott insulator, and its transition a perfect example of a Mott-Hubbard transition,[55] several recent theoretical studies,[54,56] as well as recent experimental results (although partially disputed),[57,58] have shown flaws in this

interpretation and there is now debate over the exact mechanism of this transition. Regardless of this recent debate, there are well established results, encapsulated by the phase diagram shown in Figure 1.7, about how the V_2O_3 electronic and crystalline structures behave under different influences. Specifically, we see in this figure how doping with Cr corresponds to negative pressure on the crystal lattice and how doping with Ti corresponds to positive pressure, and also how these different pressures on the lattice drastically effect how the MIT in V_2O_3 evolves with temperature.

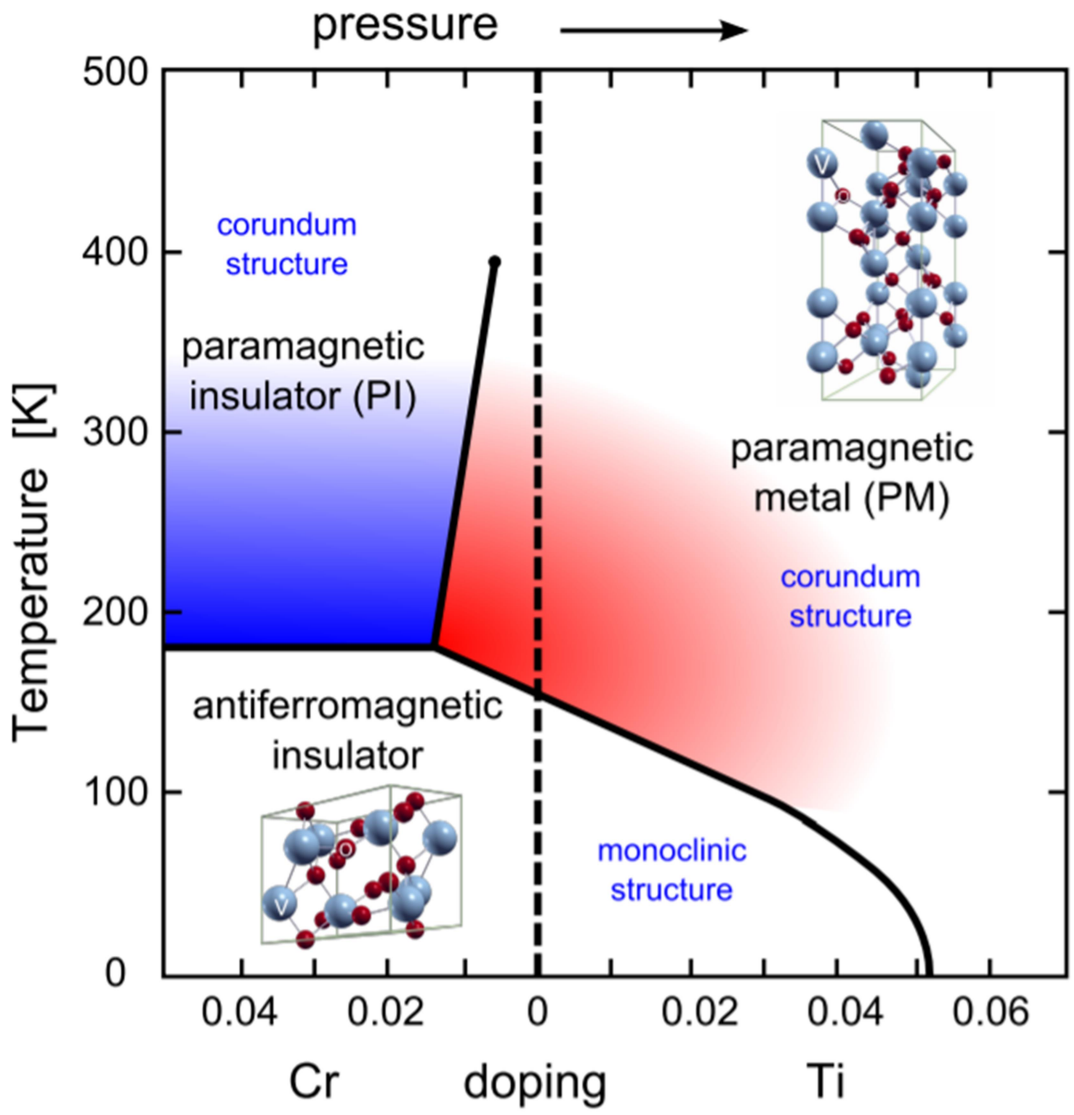

Figure 1.7. Phase diagram of V_2O_3. X-axis is simultaneously doping concentration and applied pressure to the lattice, while y-axis is temperature. Solid lines show a separation of the various insulating and metallic phases, as well as the different magnetic phases. Colors illustrate the difference between the insulating and metallic states above the transition temperature. Modified from [54].

As is the case with most transitions in transition metal oxides, it is clear that doping with other transition metals has an effect on the transition temperature. It is also clear that under 0 applied pressure or positive applied pressure V_2O_3 will have the previously discussed behavior during the MIT, going from an AF monoclinic insulator to a PM rhombohedral metal. However enough negative pressure will make it so that it no longer transitions from an insulator to a metal

with increased temperature, but instead has the structural change solely coincide with the AF-PM transition. What is less obvious is that this also suggests is the possibility of decoupling the MIT from the SPT, since there is also a region in which V_2O_3 will not have an SPT (stay in its rhombohedral state) but will transition from a metal to an insulator with increasing temperature. This has been a very compelling point in the argument that V_2O_3 undergoes an ideal Mott-Hubbard transition. However, some theoreticians have argued that more refined models, using combined DMFT/LDA techniques, suggest that there can both be formations of other intermediary phases not represented in Figure 1.7 and also mixes of phases that may present themselves as completely separate phases when studied experimentally.[54]

1.2.2 Vanadium Dioxide (VO_2)

VO_2's phase transition occurs around 340 K, with a similar thermal hysteresis to V_2O_3's transition (about 7 – 8 K). It is also an insulating material below the transition and a conducting material above, another similar trait to V_2O_3. The change in resistance in this case is smaller, around 4-6 orders of magnitude depending on the fabrication technique. As shown in Figure 1.8, it goes from a low temperature monoclinic state to a high temperature rutile state. There is no magnetic transition in VO_2 concurrent with the SPT/MIT like there was in V_2O_3's transition, it is PM across the whole range of the transition. An example of the metal-insulator transition in a thin film sample is shown in Figure 1.9. Due to its proximity to room temperature, there has been much interest into researching it for potential applications, such as metamaterials,[59,60] transistors,[61,62] temperature and chemical sensors,[63,64] and IR switches[65]. The VO_2 transition, like the V_2O_3 transition, is classically induced thermally. However studies into external stimuli's influence on the transition has shown that ultrafast laser pulses[66],voltage and current,[67] and applied pressure[68,69] can also drive the transition.

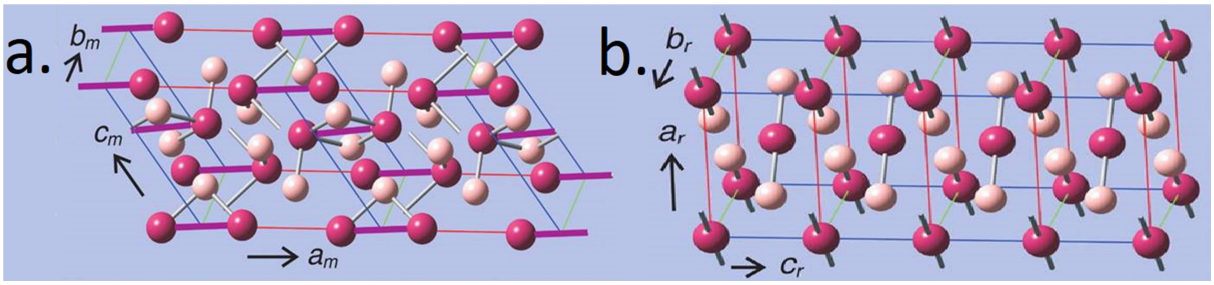

Figure 1.8. Crystal structure of VO_2. a. Monoclinic phase b. Rutile phase. Purple atoms are vanadium and pink are oxygen. Adapted from [70].

The electronic theory behind the two VO_2 states is also similar to the V_2O_3 situation. d-levels of the V ions are split into lower lying t_{2g} states and empty higher level e_g states. The t_{2g} is split into an a_{1g} state and two e^{π}_g states by the crystal field of the tetragonal state. For the monoclinic phase, V-V pairs dimerize and tilt. This causes the a_{1g} band to split into bonding and antibonding states and also pushes the V_d-O_p antibonding e_g states higher. So the single d electron will end up occupying the a_{1g} bonding, resulting in band gap.

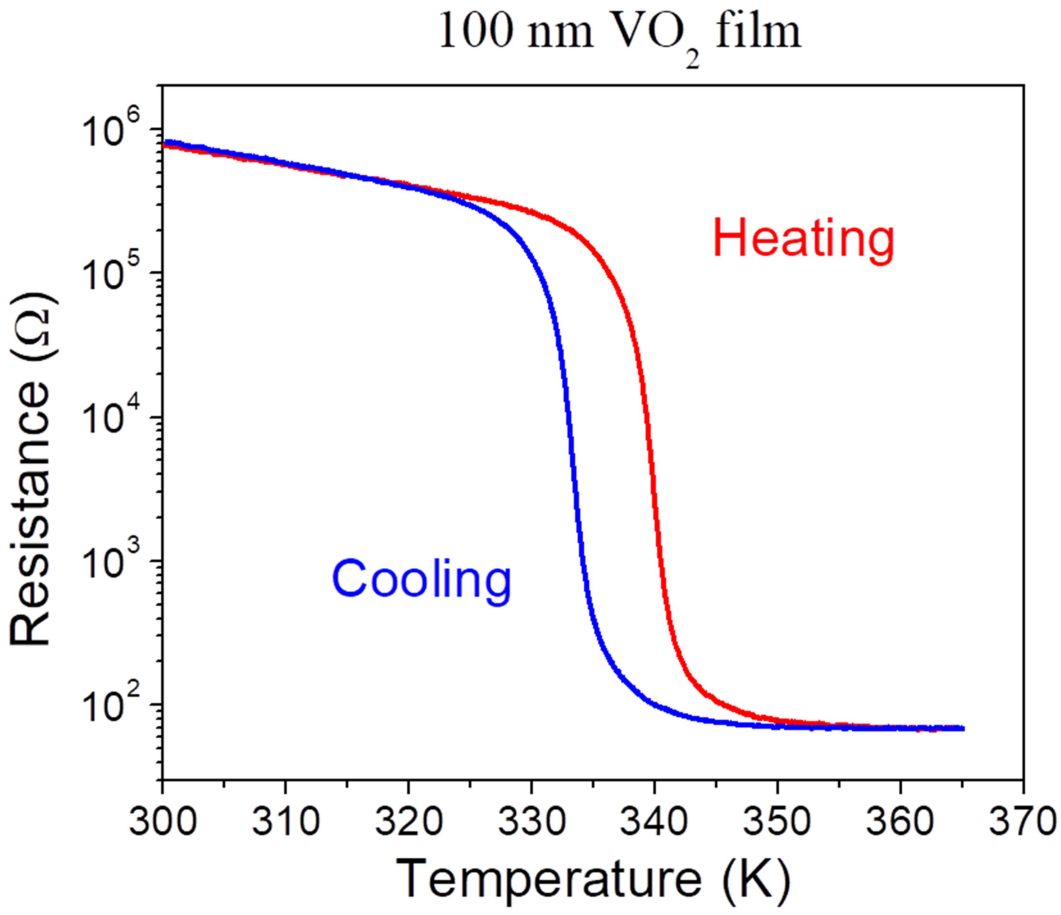

Figure 1.9. Example MIT of 100 nm VO_2 film. Large resistance drop over 15 K accompanied with 8 K thermal hysteresis.

From the preceding discussion it is clear that there are many similarities between V_2O_3's transition at 150 K and VO_2's transition at 340 K, with their biggest difference being their respective transition temperatures. However, although it may seem like the properties of these transitions are very similar, their mechanisms are quite different. As discussed in the previous section, V_2O_3 behaves close to an ideal Mott insulator in the manner in which it transitions, and has been a well understood system for many years. VO_2, on the other hand, is a much more complicated system, and there has been a large amount of debate over the exact mechanism behind the transition. Mainly, there is debate over whether the transition arises due to

electron-electron interactions (a Mott-Hubbard transition as in V_2O_3)[13,71] or if a band theory approach (Peierls transition)[72,73] is more appropriate.

The Peierls transition is a type of metal to insulator transition that is able to be explained with simpler band theory considerations. Above a certain temperature, known as the Peierls Temperature (T_P), atoms in a quasi-one dimensional metal will order equally spaced in one direction. When the temperature decreases below T_P, what's known a Peierls distortion occurs due to electron-phonon interactions in the conduction band. This means that the atoms will dimerize and the periodicity of the lattice will double. There will thus be a shift in the states at the 1st Brillouin zone to the highest occupied state, and the band will split due to the new energy gap. The dimerization will lower the electronic energy, which is what makes this possible, but it will cost elastic energy. Thus this will only occur at a temperature in which the electronic energy gain will be greater than the cost of the elastic energy.

In the case of VO_2, vanadium atoms dimerize like in a Peierls transition, as described above. The band gap that opens, as described previously, is considered to be Peierls-like and is measured to be ~0.6-0.7 eV.[74,75] Various experiments have tried to probe whether this is a Mott or Peierls like transition. An example supporting the Mott perspective was a study showing that a nanosecond voltage induced the transition.[67] This suggests that, without causing large amounts of Joule heating, the charge density in VO_2 can exceed the critical density for Mott transition.[13] This in turn implies the transition can be purely electronic, and thus the SPT and MIT can be decoupled. Another example in support of the Mott point of view is the existence of the M2 phase of VO_2. This is a separate insulating monoclinic phase, stabilized through either uniaxial stress or doping with Cr.[76] Unlike M1 phase VO_2, there is little doubt M2 phase is a Mott insulator. It has been argued that this is suggestive of M1 also being a Mott insulator.[71] On the

other hand, femtosecond pump probe experiments provide evidence that the mechanism could be due to various other factors, such as Joule heating, electron-phonon thermalization, or coherent phonons.[66,77,78]

Goodenough was able to form a qualitative model which accurately reproduces the band structure changes of VO_2, in line with the Peierls interpretation of the transition. Figure 1.10 illustrates the band structure proposed by this theory. In this theory, it is argued that it is more convenient to separate the t_{2g} orbital in relation to its band structure, with the highly overlapping states designated as the $d_{||}$ band/orbital and the less overlapping bands designated as a π^* antibonding band/orbital. The density of states can then be represented as both a partially filled π^* antibonding orbital and a $d_{||}$ orbital in the metallic state at the Fermi energy. We see that once we go below the transition temperature dimerization of the vanadium atoms causes a splitting of the $d_{||}$ orbitals. There will also be a shift in the π^* to higher energy due to the change in geometric structure. Consistent with a Peierls transition as described above, the now split $d_{||}$ orbital is completely filled in the lower energy state, while the new higher energy $d_{||}^*$ state and the π^* state are shifted above the Fermi energy and contain all of the empty energy states.

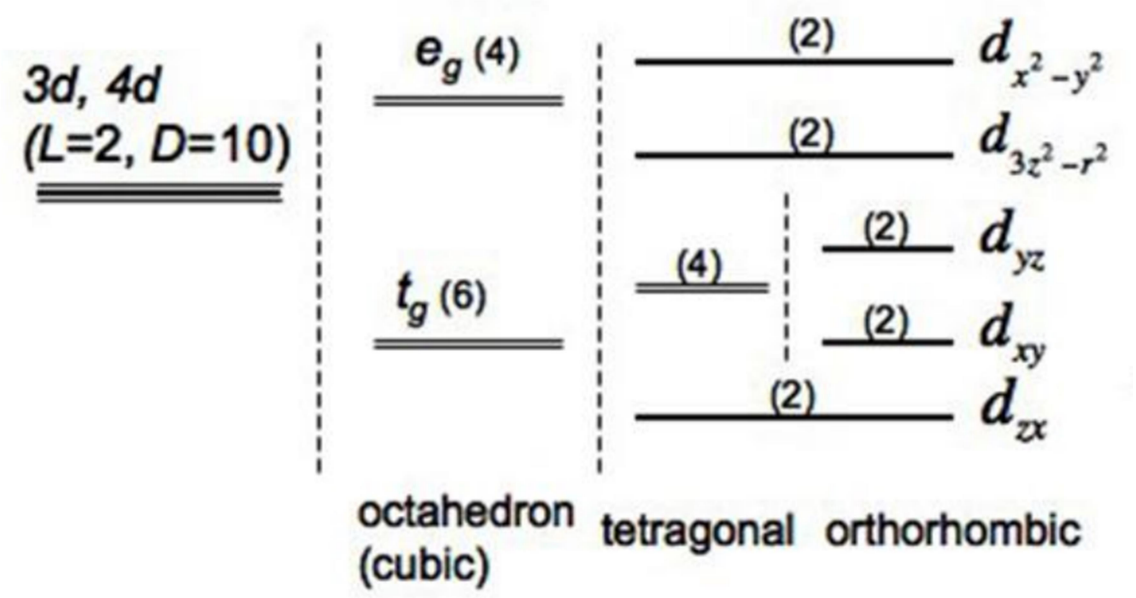

Figure 1.10. Splitting of electron states in VO_2. Left are the energy states of the cubic structure and right are the relevant energy states of the orthorhombic structure. The lower cubic states split into a single lower energy state and two higher energy states. Reprinted from [79].

Although electronic structure calculations using LDAs have been able to support pieces of Goodenough's model,[80] there are several important properties of the VO_2 transition which are not reproduced. For example, the opening of the band gap that has been measured to be 0.6 eV has not been able to be accurately portrayed in any calculations using this model. There is debate over both the conclusions and interpretations of the experimental results supporting either interpretation, as well as the validity of the various theories used to describe this transition. More recent studies have shown that Mott-Peierls hybrid models[81,82] may be better at modeling the system than treating it as a solely Mott style or Peierls like system.[83] This is further backed up by experimental results suggesting the presence of both Mott and Peierls like transitions existing simultaneously in VO_2.[84]

1.3 Optical Transition in VO_2

VO_2's transition is also known to have an influence on its optical properties as well. The effect is particularly dramatic and well-known in the IR region, but the transition affects the optical properties across a wide spectrum. VO_2 films have been used in many optical applications due to these properties, such as thermochromic windows, IR switches, optical modulators and photonic memory devices.[85–87] Although there is plenty of research into the optical transition in several forms of VO_2, such as VO_2 nanoparticles and microstructures, we will restrict our discussion only to thin film VO_2. Because of the more dramatic effects in the IR region, most studies have focused on investigating the behavior with wavelengths above 1 μm, and most device fabrication has been optimized for this region as well. An example of how a film behaves optically across the transition in the near IR region is shown in Figure 1.11.

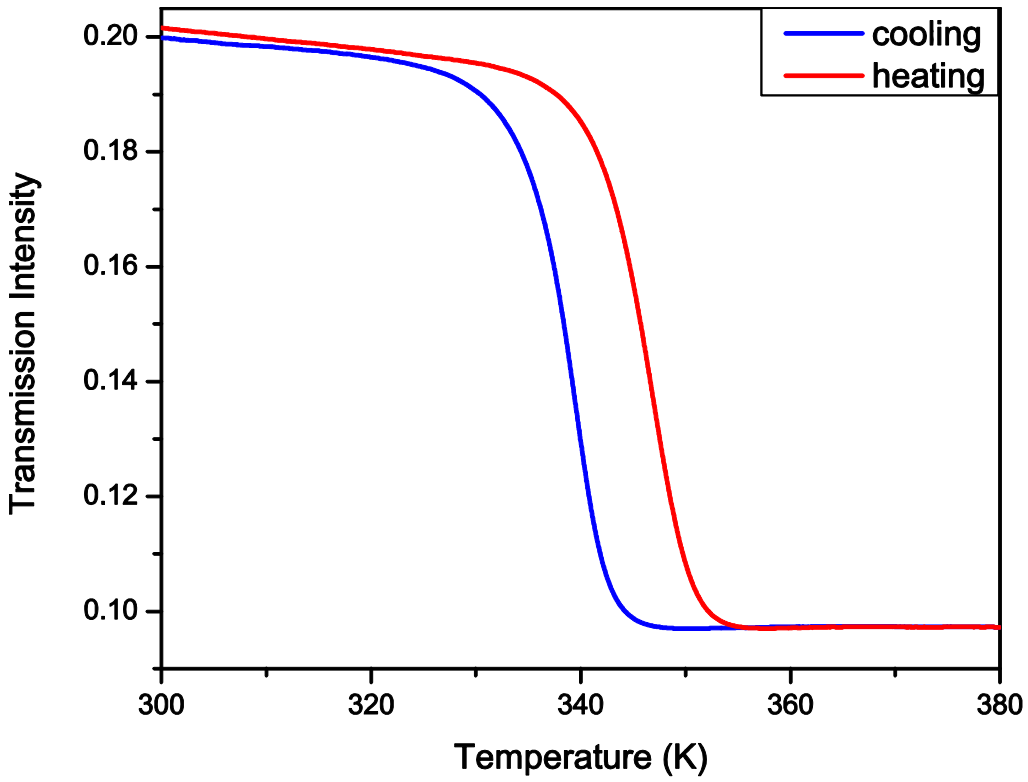

Figure 1.11. Example of the VO_2 optical transition at 345K. Measurement taken with 980 nm wavelength on a 100 nm film grown on r-cut sapphire. Thermal hysteresis is similar to that seen in electrical transport properties of VO_2 films

The response of electrons to incident radiation and the transition between electronic states are the primary origins of a material's optical properties. Also, the way that the complex refractive index is dependent on wavelength is intricately tied to the band and electronic structure of the solid. Because VO_2's transition is due to both band structure and electron correlations, the optical properties are heavily influenced by the transition and can be very complicated. Figure 1.12 illustrates this well, showing the complex and nonlinear trends that the index of refraction follows as a function of wavelength. The reason the IR region has such large changes during the MIT is due to free carrier absorption (or Drude absorption) becoming the dominant absorption in the metallic phase. The Drude model predicts that a metal's dielectric function needs to follow

$$\varepsilon = \frac{{\omega_p}^2 \tau}{\omega(\omega^2 + \tau^2)} i - \frac{{\omega_p}^2}{\omega^2 + \tau^2} \qquad 1.1$$

where ω_p is the plasma frequency and τ is the collision frequency. [88] The consequence of this relationship is that there will be more absorption below ω_p and less above it (the drop off we see in Figure 1.12). Because the insulating phase's permittivity varies on such a smaller scale, when the metallic phases permittivity diverges from it towards higher absorption at lower frequencies there is a large difference between the two, giving rise to the effects described above. Of course the Drude model does not fully predict the behavior seen in Figure 1.12 as it does not account for band gaps; the insulating state as well as finer details in the conducting state are due to band structure (for example the absorption peaks seen at larger wavelengths). Even near the plasma frequency other oscillator terms can be more important than the Drude contributions, and thus more complicated models have to be applied.

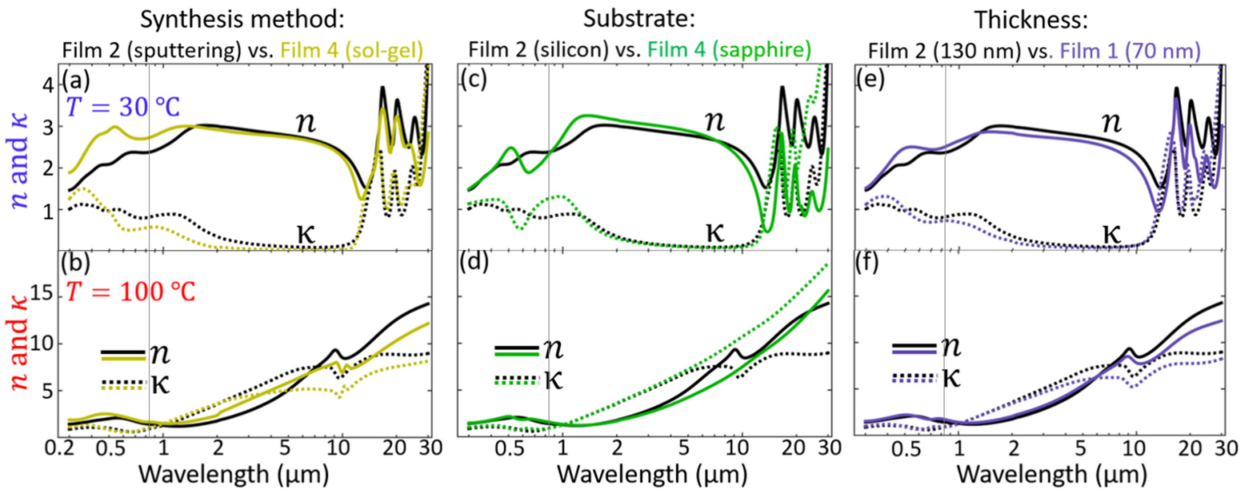

Figure 1.12. Refractive index as a function of wavelength for different fabrication conditions below and above the transition temperature. Top is below transition, bottom is above. Left is sputtering vs. sol-gel, middle is silicon vs. sapphire substrates, and right is a 130 nm thick film vs. 70 nm thick film. All graphs have solid lines for the real part of the refractive indices and dashed lines for the attenuation constants. The plasma frequency corresponds to approximately 830 nm, and this is indicated with a vertical grey line in all three plots. Adapted from [89].

Fabrication conditions of the VO_2 films are also very important when creating devices or analyzing the properties of such films. Figure 1.12 also does a good job at illustrating how six different fabrications cause variations in the refractive index across different wavelength ranges. It is well known that microstructural characteristics, such as morphology and impurities, as well as thickness play a large part in the reflectivity and absorption of thin films. This will be discussed in further detail in a later section.

1.4 W Doping in VO_2

Although VO_2's transition temperature is already close to room temperature, there has been much interest in finding ways to lower it even further to room temperature. The main way this has been done is by fabricating the VO_2 in a strained state so there is internal pressure to help shift the transition. The two ways this is most effectively done is by either depositing the VO_2 onto a substrate with a mismatch such that the crystal lattice is strained from the substrate clamping effects, or to use a dopant which will cause the crystal lattice to distort. Although the former is better at maintaining good quality VO_2 crystallinity with fewer impurities,[90] to shift the transition temperature further in temperature doping is required. However, doping also tends to decrease the change in electrical properties, a phenomenon which has been generally concluded to be because of the added carrier concentration. Several different dopants, such as W, Ti, F, Mo, Nb, Cr, Li, Al, among others, have been used to shift the transition of VO_2. Among these, the most effective dopant at lowering the temperature has been W. W has been shown to lower the phase transition ~22 K per 1% W,[91–93] and has been shown to be a substitutional dopant in the VO_2 lattice.[94] The effect of tungsten doping on the transition temperature is illustrated in Figure 1.13. Decrease in magnitude of the MIT as well as broadening is also illustrated in Figure 1.14.

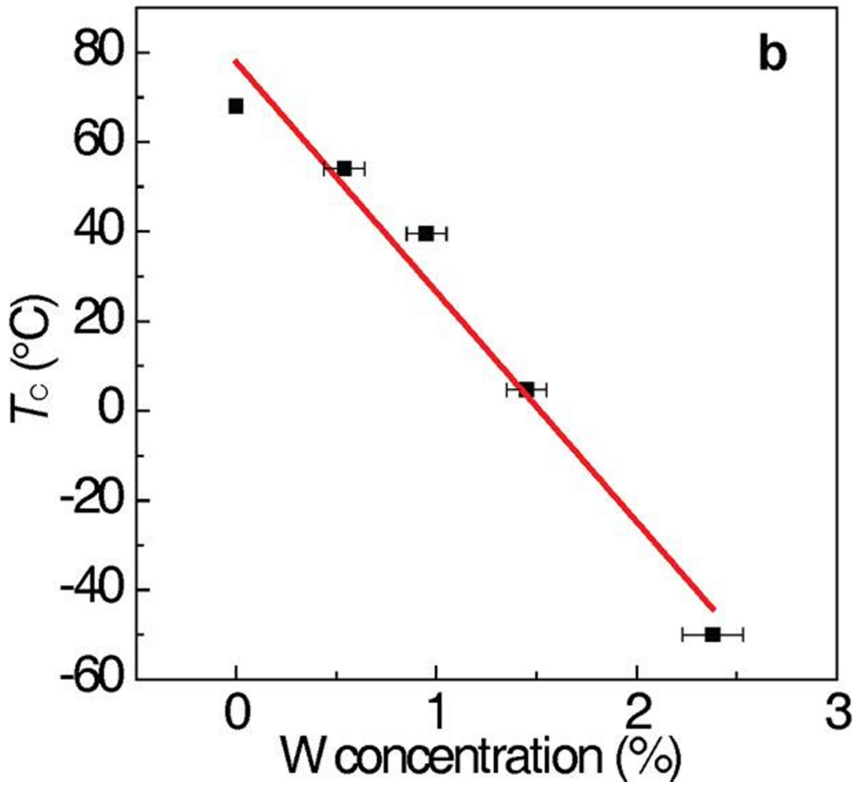

Figure 1.13. Change in transition temperature as a function of doping concentration. Adapted from [92].

$W_xV_{1-x}O_2$ systems have had several studies attempt to discover and present some mechanism behind the observed effects of the doping.[95–97] Tang et al.[96] suggested that the charge transfer from W ions decreases the bond strength between the V-V pairs, citing small-angle X-ray scattering and X-ray absorption results. Booth et al.'s[95] results support this view, showing that specific crystal axes expanded due to the introduced W dopants, breaking the Peierls-paired V ions. Both studies only investigated high doping concentrations at room temperature however, which means that they only focused on the effect of W on the rutile lattice. W atomic distances are shorter when higher doping concentrations are added, which means that, unfortunately, the strong coupling between the neighboring W atoms makes the study of single W atoms structure extremely difficult. The actual local structure around the W atom, as well as its effect on the surrounding VO_2 matrix and how it changes though the SPT, is thus still not clear. Several XAFS

studies and static lattice simulations have suggested that a local structural distortion towards the more symmetric rutile phase is caused by the introduction of the dopant to the system.[98,99] This concept has become the generally accepted view on the matter.

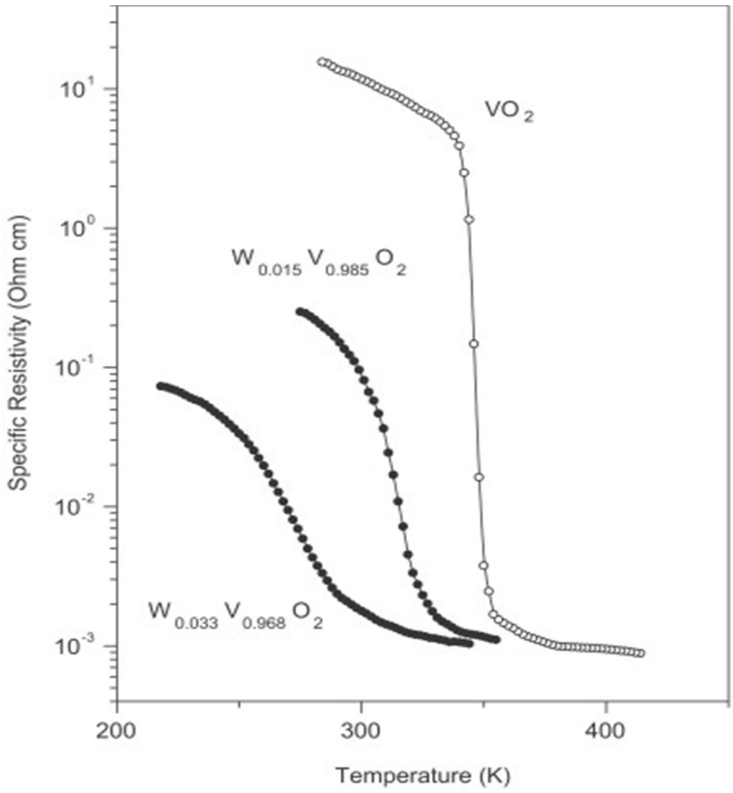

Figure 1.14. VO_2 MIT with several different doping concentrations. Only cooling curves shown. Adapted from [100].

Several techniques may be employed in doping W into VO_2 films. The easiest way to attain accurate and effective doping is to use chemical methods, such as sol-gel or CVD. However, co-sputtering or metal doped targets allow for sputtering or PLD to also be a feasible technique, although control of doping is more difficult in these instances. Bulk or nanoparticle VO_2 may also be doped easily using chemical techniques during the synthesis, such as addition of tungsten oxide compounds during hydrothermal synthesis and then partial reduction. However physical techniques, such as ball milling, may also be used, although they are less effective at introducing dopants to the system.

1.5 Magnetic Hybrid Structures

Magnetic hybrid structures are a type structure that is formed when a ferromagnetic material is bound to another solid which has coupled properties to the ferromagnet. There has been long lasting scientific interest in these materials due to the fact that these materials can both have a change in the coupled material properties on the application of an external applied field or can have a change in magnetic properties due to influence on the coupled material properties. There are many ways in which to couple the materials, such as directly coupling magnetic properties (FM-FM or FM-AF coupling). Another way is to electrically couple to piezoelectrics, ferroelectrics, or materials which undergo a MIT. They can also be coupled due to strain changes at the boundaries of the materials. Materials which undergo a SPT allow for a large amount of change in the strain between the materials, so these are obvious choices for this specific mechanism. This last case is the one in which we will focus.

These strain-coupled materials can take many forms. It is common for them to be formed by either making composites or by forming multilayers between of a material with an SPT and a ferromagnet.[101–103] There have also been cases where nanostructures involving the two types of materials were formed.[104] The mechanism behind the strain coupling of the materials to magnetic effects is the magnetostrictive effect and its inverse. For example, when there is a large volume change in a material due to its SPT, the expansion will either cause the materials to be forced together and experience isotropic stress or have a change in stress at the interface. This will also happen at an interface when there is linear dimensional change during the SPT. Details about the magnetostrictive effect will be discussed further in a later section.

A specific example of this which has seen an increase interest is the mixture of a vanadium oxide, which has an SPT, and a ferromagnet. This was first accomplished by

magnetron sputtering either VO_2 or V_2O_3 and coating them with either Ni or Co.[105] These results have been shown to be able to be tuned, with enhancements of coercivity at the transition temperature of more than 200%.[51,105–108] There has also been a proof of concept study on expanding the breadth of this system to bulk mixtures, using a mixture of V_2O_3 and Ni.[109] An example of two bilayer films is shown in Figure 1.15.

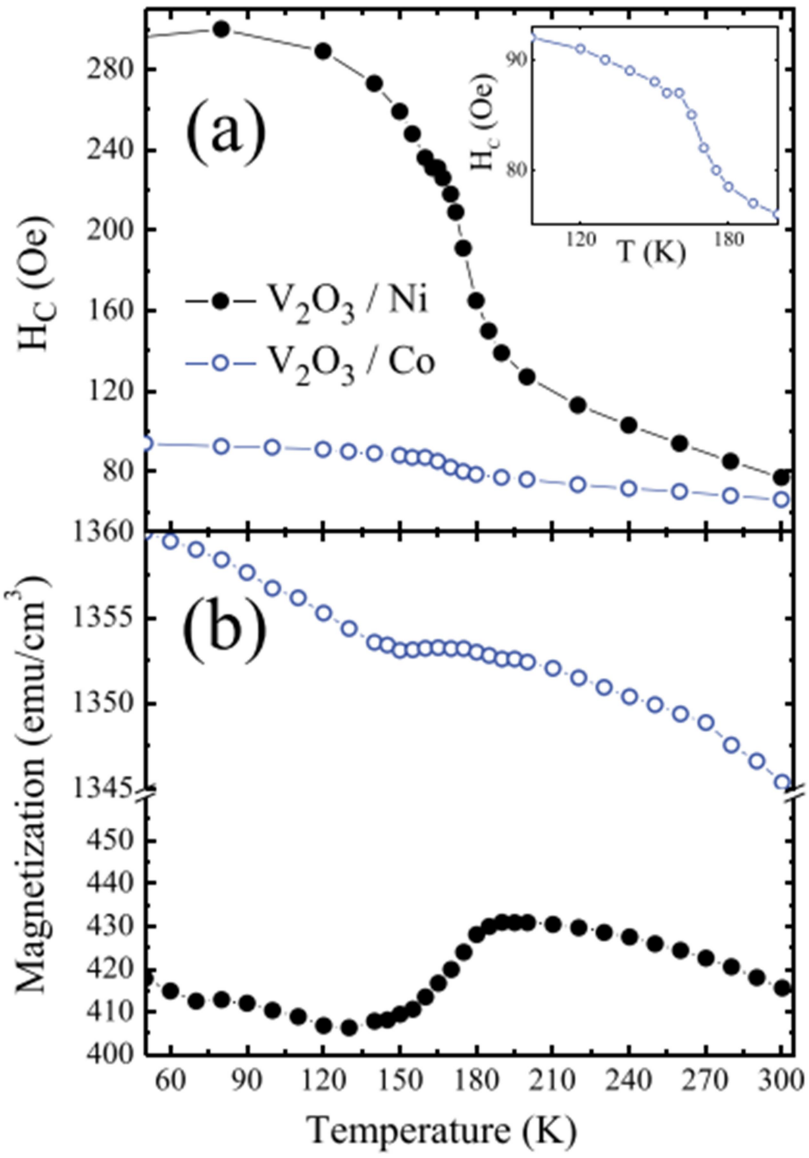

Figure 1.15. Changes in both coercivity and magnetization across VO_2 transition. a. Coercivity as a function of temperature, with inset zoomed in on the change in coercivity of the V_2O_3/Co bilayer around the transition temperature. b. Magnetization as a function of temperature. Blue data points are data for a V_2O_3/Co bilayer and black are for a V_2O_3/Ni bilayer. Adapted from [105].

One of the reasons these materials have excited such interest is there capability to be used in some important applications. These include pressure sensors,[110] magnetic field sensors,[111,112] optical sensors,[113] magnetic refrigeration,[114] biomedical diagnostics,[115,116] among many others. One of the most high profile applications that has recently had many advances is heat assisted

magnetic recording (HAMR). As data storage density needs to be increased, one of the problems that arise is that the smaller the domains get the harder it is to keep them from spontaneously flipping, so high stability is required. However, if there is strong stability higher fields are required to magnetize the bits, and these fields are both inefficient to produce and also may be impossible to produce on such small scales. HAMR technology has been one of the main ways to resolve this limitation. By using a material with a room temperature (RT) state which has higher coercivity, the storage can remain stable, while having a high temperature (HT) state with lower coercivity allows the material to be heated for writing data.

1.6 Magnetostriction and Inverse Magnetostriction

The magnetostrictive effect, also known as Joule magnetostriction, is a property of materials in which an external applied field, causing magnetization in the material, will also cause a change in size or shape. It was first identified in 1842 by Joule during his study of iron. What is normally described as Joule magnetostriction is a longitudinal magnetostriction, which is what will be elaborated on here. There are other types of magnetostriction that involve changes in shape, but these are actually just special cases of longitudinal effects anyway. The fractional change in length for this effect is known as the magnetoelastic constant λ, give as follows:

$$\lambda = \frac{\Delta l}{l} \qquad 1.2$$

where Δl is the change in length and l is the length of the material. When discussing the effect, usually λ_s is what is relevant, which is just λ at the saturation magnetization of the material. It is clear from the above equation that if the magnetoelastic constant is negative there is a contraction and if it is positive there is an expansion.

There also exists an inverse magnetostrictive effect, also called the Villari effect after the researcher who discovered it, in which an applied strain to a ferromagnetic material will cause a change in magnetization and other magnetic properties. Even though the magnetostrictive effect causes only small strains to be produced, this inverse effect causes the permeability, the magnitude of magnetization in an applied field, and the shape/width hysteresis loops to be strongly dependent on the stress applied to material with stronger magnetostrictive effects. This effect is illustrated in Figure 1.16 for a Ni thin film. There are thus many practical applications that can result from magnetostriction, and there has been a large amount of research devoted to it and how it can be used in devices.

Magnetostriction manifests in all pure substances, but even for stronger ferromagnets the constant is quite small (on the order of 10^{-5}). As an example, polycrystalline nickel (which is the ferromagnetic compound which will be discussed the most in this thesis) has a magnetostrictive constant of $\lambda_p^{si} = -34 \cdot 10^{-6}$. Here the superscript s refers to saturation magnetization as above, the superscript i refers to the fact that the measurement to determine the constant was performed in an ideal magnetized state, and the subscript p refers to the crystalline orientation (polycrystalline in this case). Ni has one of the largest values of magnetostriction for a pure element ferromagnet. The exception is rare earth metals, which have such strong spin orbital coupling that the effect can greatly influence their electron orbitals. Unfortunately, they are costly and have low availability as a resource, making them not ideal for longer term consideration in applications. There are alloys which include rare earth metals that have shown giant magnetostriction, namely Terfenol-D ($Tb_xDy_{1-x}Fe_2$) and Galfenol ($Fe_{1-x}Ga_x$). Although the magnetostrictive effect in these compounds is orders of magnitude larger than for nickel, they

are difficult to fabricate and have low chemical stability, making them difficult to incorporate in devices for potential applications.[117]

A simplified description of the spin-orbit coupling based mechanism behind magnetostriction is as follows. In a ferromagnet, the spontaneous magnetization will tend to align the atoms, and the extent of this alignment is directly dependent upon the strength of spin-orbital coupling in the material. The exact manner in which the alignment occurs is dependent upon the crystalline anisotropy. This also determines the easy axis of the material. If we then apply a field along another axis, the spins and the electron clouds would rotate along this axis (the exact extent dependent on both spin-orbital coupling as well as the applied field strength). This change in orientation will change the distance between the nuclei of the atoms, and thus they will be in a strained state. On a larger scale this is causing domains themselves to be stretched or contracted, thus leading to a change in strain at the domain boundaries in the material.

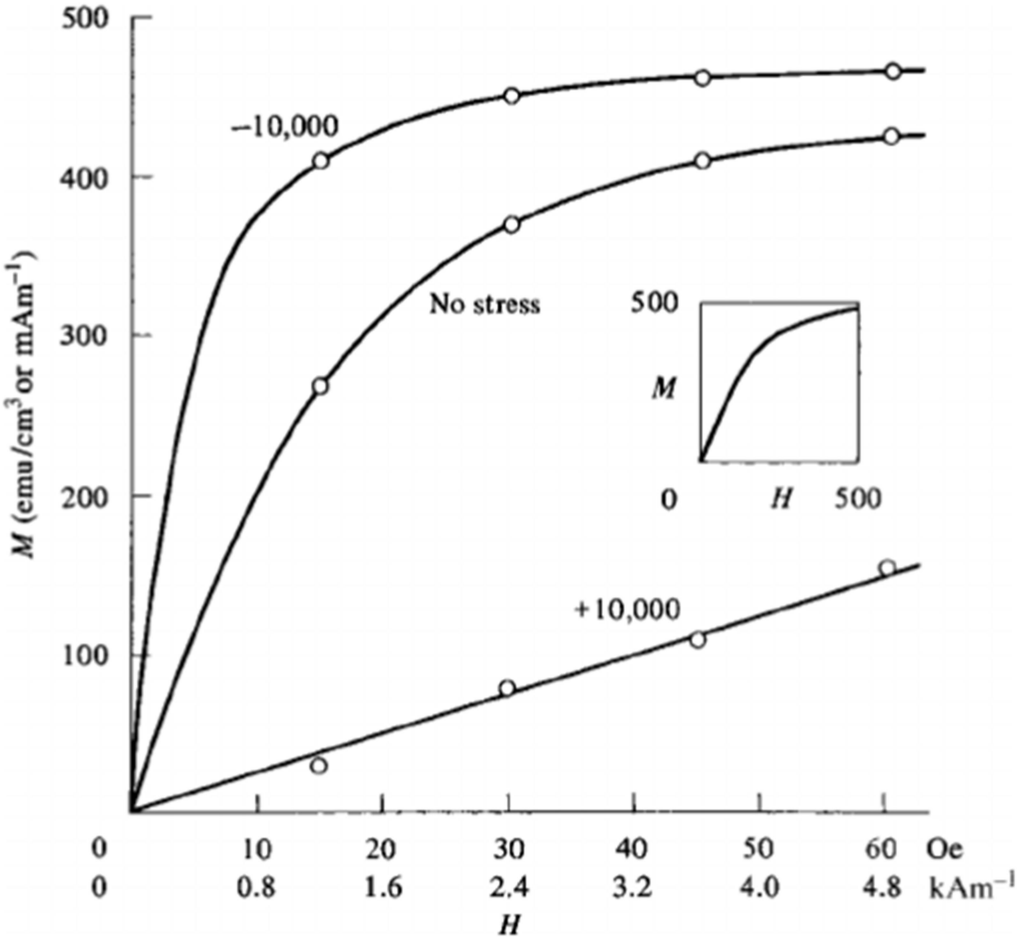

Figure 1.16. Magnetization as a function of applied field of a polycrystalline Ni film, with different applied stresses. Compressive stress causes an increase in magnetization and tensile stress causes a decrease. Modified from [118].

It is known that stress in and of itself can induce a magnetic easy axis. So, when stress exists in a ferromagnet, any stress anisotropy must be taken into account. To determine what this is dependent on for polycrystalline Ni, we look at the anisotropy energy for a cubic crystal. The energy is given as an expansion of the deformations in the crystal, which in a highly symmetric cubic crystal simplifies to:

$$E_{anis} = -\frac{3}{2}\lambda_{100}\,\sigma(\alpha_1^2\gamma_1^2 + \alpha_2^2\gamma_2^2 + \alpha_3^2\gamma_3^2) - 3\,\lambda_{111}\,\sigma(\alpha_1\alpha_2\gamma_1\gamma_2 + \alpha_2\alpha_3\gamma_2\gamma_3 + \alpha_3\alpha_1\gamma_3\gamma_1). \quad 1.3$$

Here λ are the magnetoelastic constants for different crystallographic orientations, σ is the applied stress, γ are the direction cosines for the stress relative to the crystal axes, and α are the direction cosines for the magnetization. In a polycrystalline film, it is reasonable to assume that $\lambda_{100} = \lambda_{111} = \lambda_p^{si}$, since it is a mixture of the different crystalline orientations. This simplifies the energy anisotropy to be

$$\mathrm{E_{anis}} = \frac{3}{2}\,\lambda_p^{si}\sigma\,\sin^2(\theta) \qquad 1.4$$

neglecting a constant term, where θ is the angle between the magnetization and the stress vector. It is a uniaxial anisotropy and can be related to the uniaxial anisotropy equation $\mathrm{E_{anis}} = \mathrm{K_\sigma}\,\sin^2(\theta)$. Thus, we see that the stress anisotropy constant in this case is given by $\mathrm{K_\sigma} = \frac{3}{2}\,\lambda_p^{si}\sigma$, and we can plug this into the relationship between M and H for a uniaxial crystal to get[118]

$$\mathrm{M} = \frac{\mathrm{M_S}^2\,\mathrm{H}}{2\,\mathrm{K_\sigma}} = \frac{\mathrm{M_S}^2\,\mathrm{H}}{3\,\lambda_{\mathrm{si}}\sigma} \qquad 1.5$$

for $\mathrm{M_s} \geq \mathrm{M}$. When $\mathrm{M} = \mathrm{M_S}$, we can now solve for what is called the anisotropy field $\mathrm{H}_{K\sigma}$, as

$$\mathrm{H}_{K\sigma} = \frac{3\,\lambda_{\mathrm{si}}\sigma}{\mathrm{M_S}}. \qquad 1.6$$

Chapter 2. Fabrication and Characterization Techniques

2.1 Introduction

The fabrication of phase pure VO_2 and V_2O_3 in various physical forms has been of high interest due to their unique properties. Bulk methods of synthesis have included thermolysis,[119,120] hydrothermal synthesis,[121] and annealing of V_2O_5 under different atmospheric conditions.[122] Sol-gel synthesis followed by a coating technique,[123] sputtering,[124] pulsed laser deposition,[125] and chemical vapor deposition[126] are all techniques that have been shown to produce high quality films for both VO_2 and V_2O_3. Annealing is often used as a step in these synthesis techniques to alter the chemical makeup of the materials, but many of the techniques for both bulk and film fabrication also require a post annealing to properly crystallize materials.

To adapt film growth for the scalability needed for industrial use, both sol-gel and sputtering have several advantages over the others. Both techniques have a simplicity which allows for this scalability. Sputtering has the benefit of allowing for great control over fabrication parameters, such as atmosphere and temperature, resulting in high quality films with desired specific properties. Thickness can also be controlled with ease, allowing for films of thicknesses ranging from nanometers to microns. Sol-gel synthesis, although not allowing for as much control over any of these properties in comparison to sputtering, is both a cheaper and an even more scalable technique. Although sol-gel synthesis' lack of parameter control produces more impurities and less uniformity than sputtering, it also has other advantages that sputtering lacks, such as a more precise control when adding dopants or alloying materials.

In our work we used a newer technique for our bulk synthesis which allows for the vanadium oxides precursor to be formed into a composite before the annealing step to form the desired compounds. This relied on forming composites using ball milling, a technique commonly used for precise chemical mixing, alloying, and forming nanoparticles. For our films we used a mixture of sputtering and sol-gel synthesis for different samples, exploiting the strengths of each depending on when they were needed. Characterization of composites was done mainly using powder x-ray diffraction techniques (PXRD). This data was important to collect for bulk solids due to the likelihood of forming impurities and possible introduction of contaminations during the fabrication. However, VO_2 films were mainly characterized using electrical transport measurements, with x-ray diffraction used as a confirmation of the crystalline structure. This is possible because of the large dependence the electrical transition in vanadium oxide films have to the crystalline quality and introduction of impurities. Even slight changes in fabrication parameters can shift the magnitude, sharpness, and hysteresis of the VO_2 MIT dramatically. Thus samples were generally optimized for both larger magnitudes and sharper transitions, which meant at least 4 orders of magnitude for sputtered films and at least 2.5-3 orders of magnitude for sol-gel synthesized films. Furthermore, when dopants were introduced electrical measurements were a key factor in determining whether the introduced dopants had effectively doped the VO_2, by showing how much the transition was shifted upon their introduction. Crystallinity was confirmed using x-ray diffraction (XRD), and impurities in the sol-gel determined. Thicknesses were determined by using x-ray reflectometry (XRR) for sputtered films and contact profilometry for sol-gel films.

As the morphology of both bulk solids and films is important for understanding the interface between vanadium oxide compounds and the ferromagnetic compounds they are in

proximity to, microscopy measurements were also taken. For bulk solids scanning electron microscopy (SEM) was the most useful option for visualizing the mixture of vanadium oxide and Ni, with energy dispersive x-ray spectroscopy (EDS) used in tandem to visualize how the different compounds and impurities were dispersed throughout the solid. Atomic force microscopy (AFM) was used to image the films surfaces, allowing for determination of both grain sizes and roughnesses.

To determine the behavior of the ferromagnetic component in the composites and the ferromagnetic layer of our heterostructures, two different types of magnetometry were used. Vibrating sample magnetometry (VSM) has the advantage of being a quick technique, so it was used for magnetization measurements as a function of field. However, due to the nature of the technique, it's less suitable for high accuracy magnetic moment measurements over long periods of time; magnetic moment measurements as a function of temperature were instead collected using a superconducting quantum interference device (SQUID). To test the optical properties of pure VO_2 films simple reflectometry measurements were taken as a function of temperature. Details about both the fabrication and measurement techniques will be further elaborated upon in the rest of this chapter.

2.2 Ball Milling

Ball milling is a simple mechanical process which has its roots in ancient times.[127] It is a grinding technique in which balls are used to impact a material over time to break it into smaller pieces. A ball mill typically consists of a hollow cylinder which is rotated so that the balls fall from the top to crush and grind the material. A simple diagram showing this process is seen in Figure 2.1. Ball mills are capable of grinding cements, silicates, rocks, ceramics, rocks, and

many other hard materials, owed to the high speeds generated in the grinding medium. Ball mills have several advantages over other mixing, grinding, and alloying systems. For one, the cost is extremely low. Another is that the system can be easily modified for different particle sizes and product capacities. It can also be easily modified to continuously operate for alloying. The use of ball milling as a scientific tool has allowed for alternative ways to catalyze chemical reactions without the use of a heating process, instead relying on the high impact energies of the process, effectively lowering reaction temperatures. It can also be used as a way to induce physical transformations to a solid mixture, notably in the amorphization of a material. There are, however, several considerable drawbacks as well. Contamination at the interface of the milling tools and the material can prevent the milling process form progressing efficiently. There is also no control over the particle morphology, and unwanted agglomeration of particles often occurs.

The material the balls are made of is important for a variety of reasons. Smaller balls will result in smaller final particles, but are unsuitable for grinding larger pieces of material efficiently. The density of the balls needs to be higher than the sample material or else it won't impact through the material. Hardness of the balls needs to be high enough to actually grind the material in question, however not so hard that it can damage the system components. Any possible chemical reactions need to be taken into account as well when matching the ball (grinding media) material with the sample material. We should also note that while the grinding media used here is often referred to as "balls", it can often be other shapes depending on the specifics of a system.

During the process the sample material goes through several stages. First the particles are flattened by compressive forces, and there are changes in shape to individual particles, while clusters are broken into smaller clusters. Next there is what is effectively a cold welding process

that takes place, shortening the diffusion distance to the micrometer range. After this step, alloying starts to take place and particle sizes become considerably reduced. Finally, the particles will have taken a deformed metastable structure, and a true alloy is formed. It's important to note that the milling process can be stopped at any of these stages depending on the desired result. Another important note is that, although the stages described above are a general overview of what happens in the process, due to the large variability of how different grinding media will physically and chemically interact with different sample materials, actual theories behind the ball milling process must be worked out in more of a case by case manner to fully understand what happens with specific combinations.

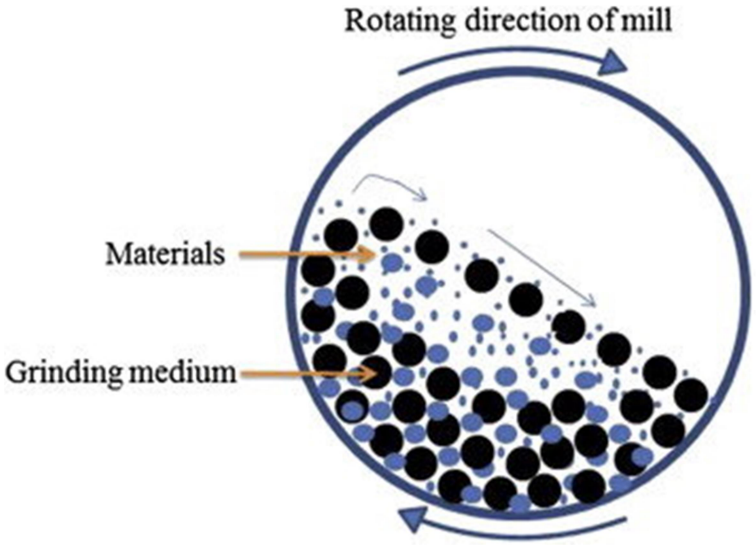

Figure 2.1. Diagram of Ball Milling Process. Grinding media and sample material are rotated together at high speeds to produce impacts. Adapted from [128].

The ball milling set up used was a Spex Sample Prep 8000M Mixer/Miller high energy ball mill. The milling jars were 45 ml, with a 2.25" diameter and 2.69" in length, and were made of zirconia ceramic to prevent the magnetic contamination that would be involved with using the usual milling jar material of steel. Two zirconia ceramic balls (12.7 mm in diameter) were used as the grinding media for all samples for this same reason. Corprene (a mixture of cork and

neoprene) gaskets were used as a seal for the cap to the milling jar. Zirconia is made with trace amounts of magnesium and hafnium (<0.5%), although these do not have much of an effect on the process due to the low contamination rate. This mill combines both the traditional axial rotation of the sample jar with a vibratory motion, such that the jar will go through a figure 8 motion at a frequency of 18 cycles per second. During milling, the system is typically given 10 min relaxation periods every 100 minutes to protect the system from damage. All milling is performed in air with STP conditions. Samples loaded into the jar never exceeded the recommended maximum load limit of 40% of the jar's volume.

2.3 Annealing and Sintering

Annealing and sintering both have several definitions common to different fields. To avoid confusion, we will define what we mean by both of these terms when they are used in the rest of this work. Annealing is a heat treatment process that causes microstructural changes in a material, resulting in alteration of either mechanical and/or electrical properties, and possible crystallization of the material. The crystallization, or recrystallization, process involved here can also change the grain structure of the material considerably, either through changing the size of the grains or promoting growth of new grains. Chemical changes may also occur and be promoted during this process. Sintering is essentially the same process, but with material that has been put under pressure at some point in the fabrication process. Sintering not actively done under pressure is considered pressureless sintering, which is what was used exclusively in our research. Cold isostatic pressing with a hydraulic press was used to form our compacted materials before the heat treatment itself. Sintering causes physical changes similar to those described for annealing. A large difference lies in the fact that sintering can cause atoms in

separate materials to diffuse across the boundaries of the particles, possibly fusing particles into larger pieces.

Films were the primary type of sample material used in the annealing processes. We either used the same chamber used for sputtering (which will be described in detail below) or used a three zone tube furnace. For the sputtering chamber we kept the pressure at 4 mTorr and annealed in an atmosphere of argon gas. When using the three zone furnace, the sample was placed in the center of the furnace with all three zones set to the same temperature so that the center would have very rigorous temperature stability. The tube was a quartz tube with an 18 cm diameter. Heat resistant foam blocks were placed on the ends to help insulate the inside of the furnace. Separate heating coils were used to heat each zone, with thermocouples at the center of each zone to measure the temperature. The inside of the furnace itself was similarly insulated with heat resistant foam. Annealing was done under vacuum without any introduced gases by using a simple electric pump to keep the chamber in the 10^{-3} Torr range. In this setup, the pressure was not rigorously controlled.

Bulk solids pressed into pellets were used as the sample material in our sintering processes. A smaller tube furnace was used for the sintering process, a diagram of which is shown in Figure 2.2. A smaller quartz tube with 8 cm diameter was used in the furnace in these cases. Besides this, and the lack of the two extra zones, the furnace setup was identical to the previous one described above. Because there was only one zone of temperature control, the temperature stability inside of the furnace was significantly less rigorous, especially if care wasn't taken to place samples directly above the thermocouple. Samples were placed in either a quartz or alumina ceramic 'boat' inside of the tubes during these processes. The vacuum was provided by a simple oil pump, with a system of valves and a digital pressure gauge to more

rigorously control the pressure than in the larger system. Samples that were sintered in vacuum were typically kept between 3 mTorr and 100 mTorr, with a stability of 5 mTorr. Other samples were sintered under Ar, N_2, or O_2 gas at room pressure, using a water-locked bubbler to prevent air contamination.

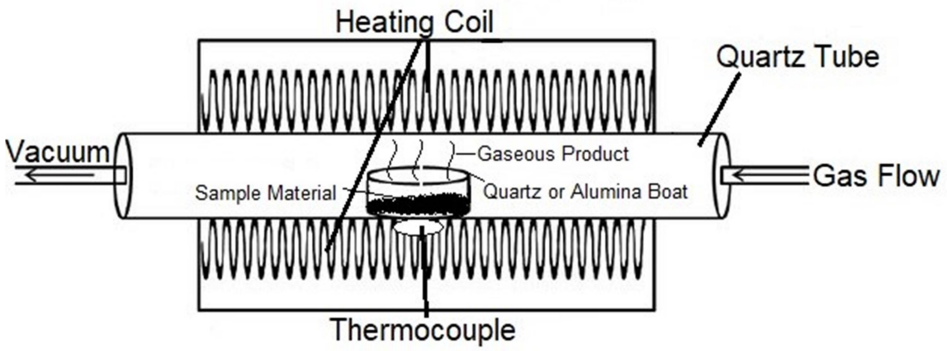

Figure 2.2. Diagram of a furnace system set up for annealing process. The tube is heated up with heating coils, which in turn heats a sample holder known as a 'boat' to bring the sample material to the correct temperature.

2.4 Sol-gel Synthesis

Sol–gel synthesis is the preparation of inorganic polymers or ceramics from solution, by converting liquid precursors to a sol, and then into a gel. A sol is a dispersed solution of colloids, and a gel is a diphasic system of solid and liquid. Specific to this technique, gel formation is the stabilization of a colloidal matrix of metal oxides. The gel phase morphologies can range from discrete particles to continuous polymer networks. Precursors are typically either a metal alkoxide or a metal chloride, both of which undergo hydrolysis and polycondensation reactions to form the gel. In simple terms, this means that the metal complex is split into a smaller metal oxide monomer, which is then joined together with other monomers to make metal oxide polymer chains.

Once the gel is formed, there are different routes that can be taken to form different final products. Films can be coated and heated to form dense films, the gel can be evaporated into dense ceramics, or uniform particles can be precipitated from the gel. Ceramic fibers can even be formed if the gel is treated in a furnace appropriately. For depositing on a film, either dip coating or spin coating may be used. The dip coating process is when a device is used to immerse a substrate into the gel at a specific frequency, whereas spin coating is when the gel is dropped onto the substrate and the substrate is rotated at a specific frequency. Spin coating results in much more uniform films, as dip coating tends to leave a much larger amount of gel at the lower end of the substrate. This is one of the reasons we chose spin coating for this step in our process.

An overview of the specific process used for this work is shown in Figure 2.3. The precursor is continuously stirred until a gel is formed, and then the gel is dropped onto a substrate to be spin coated. Frequency of the spin coater was varied depending on the desired sample. After spin coating the film is heated to dry the gel and stabilize the structure of the film. Spin coating and drying is repeated several times until the film is of the desired thickness. After the desired thickness is reach there is an annealing in a furnace to both finish the drying process and crystallize the new film.

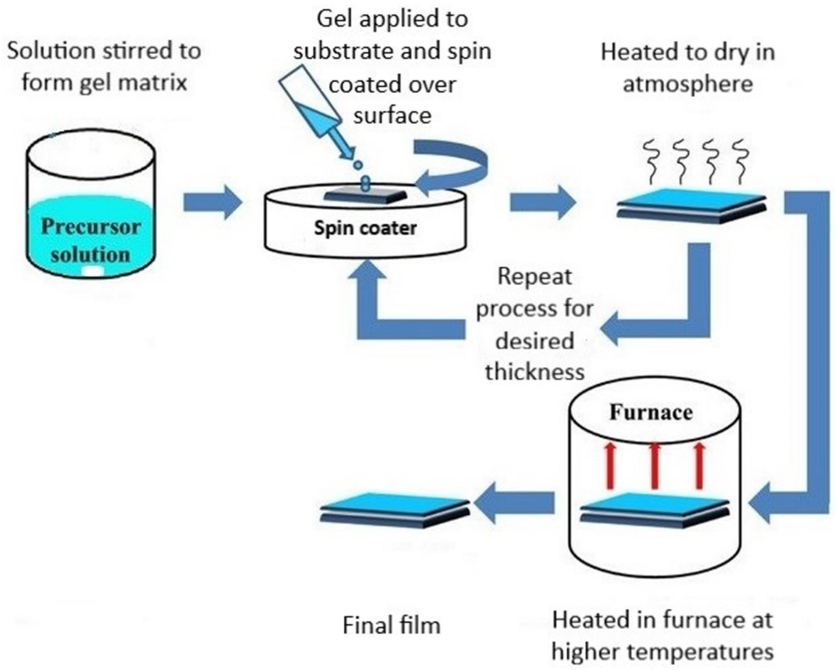

Figure 2.3. Overview of a sol-gel synthesis process using the spin coating method. Redrawn from [129].

2.5 Thin Film Deposition

Thin film deposition techniques can be divided into categories based on the different power source technologies and physical mechanisms. This includes direct current (DC) diode, triode, radio-frequency (RF), pulsed plasma, ion beam, among others, for power sources, and most commonly either evaporation or sputtering for the coating technique to be used. We will limit this discussion to the two methods used, DC and RF diode sputtering.

Diode sputtering is a technique wherein atoms of a target material for deposition are ejected through a collision with ions due to an applied potential. The target material has a voltage applied such that it acts as a cathode, with the walls of the sputtering gun as the anode. Electrons in the atmosphere around the gun are accelerated by this potential difference can then interact with the atmosphere near the gun, ionizing it if they have enough energy. Typically Ar gas is used as the working gas, however many other inert gases are used as well. Once Ar gas is ionized

into a plasma of Ar^+ ions, they will be drawn towards the cathode and impact the target. If this collision is of high enough energy, atoms of the target will be released, allowing them to be deposited on a substrate material. An illustration of this simplistic description of sputtering is shown in Figure 2.4.

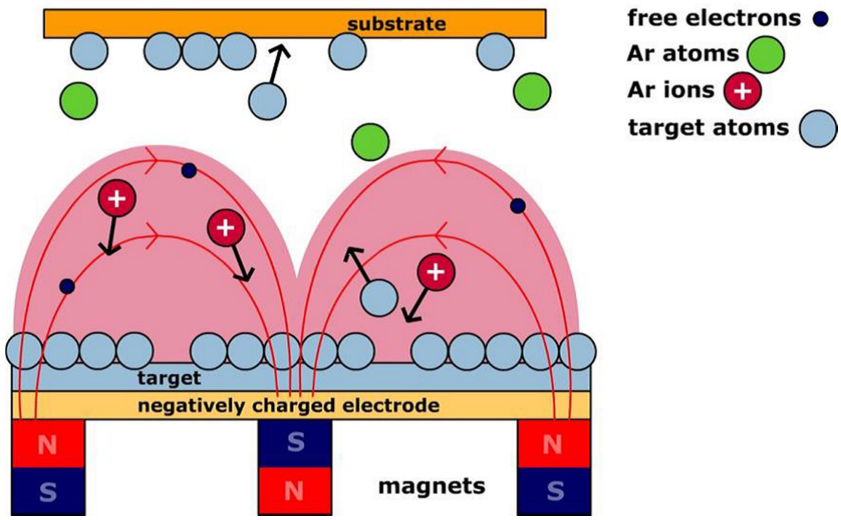

Figure 2.4. Diagram of the sputtering process using a magnetron sputtering technique. The Ar atoms become ionized and impact the target, which releases them to be deposited on a substrate material. (Courtesy of AJA)

We also see in Figure 2.4 that there is a magnetic arrangement near the target. Known as magnetron sputtering, magnets are placed near the target to confine the ions to the magnetic field around it. There are several benefits to adding this arrangement to a diode sputtering system. The main benefit is that the confinement of the ions allows for higher density plasma to be formed and a larger number of collisions to occur, increasing the deposition rate. An added benefit is that the confinement also decreases the number of stray electrons that could damage the substrate and depositing film.

The two different power supply modes for our sputtering procedures were DC and RF. DC sources apply a voltage constantly in one direction, whereas RF sources alternate at a

frequency of 13.56 MHz. DC power supplies are sufficient for conducting targets because charges are free to move throughout the material. However for semiconducting and insulating targets positive charge will collect on the surface and will both decrease the efficiency of the collision processes and can damage/crack the target. RF power supplies circumvent this problem by reversing the polarity of the current with periodicity, removing the excess charge that builds up. There are two main drawbacks of using this method however. One is that deposition rate is halved by the alternating nature of the power source, which could be an issue for the fabrication of thicker films. The other is that the circuitry required in maintaining an RF source is much more complicated. RF sources require a much higher voltage to sustain, and is best utilized by equipping shielding for the extra heat that is produced, a blocking capacitor for DC self-bias, and a matching network for optimal power transmitted. This circuitry can be quite expensive when compared to the requirements of a DC setup, an important consideration when processes need to be scaled.

One last thing to note in terms of sputtering options is the ability to add gases into the sputtering atmosphere beyond the working gas. Nitrogen, oxygen, and hydrogen are several additives which are commonly used in this way. They are sometimes added for catalytic effects, but are most commonly added to react with the atoms being deposited to change their stoichiometric and crystalline structures in some way. Use of this option is known as “reactive sputtering”, and can allow for greater control over the deposit than simply relying on a ceramic target with the desired stoichiometry.

The system used for our work was a custom Orion system by AJA international. A simple diagram of one of these systems is displayed in Figure 2.5. The sputtering environment is contained in an ultra-high vacuum chamber. A turbopump is used in tandem with an adjustable

gate valve to maintain the desired pressure for the system. This typically ranges from 3 mTorr to 50 mTorr during a sputtering process, and can provide a base pressure below 10^{-7} Torr. Mass flow controllers control the atrial pressure of input gases to the system, with the capability of using Ar, O_2, and N_2. As seen in the figure, a load lock system is utilized to circumvent having to open the main chamber of the system after every deposition, which allows for the maintenance of a higher quality base vacuum before sputters. Four 2" diameter sputtering guns are arranged in a confocal geometry at the bottom of the chamber. They are placed in adjustable mounts which allow for control over both the sputtering angle and proximity to the substrate. The substrate holder is mounted at the top of the system above the guns in the center of the confocal geometry. There is a motor which allows for continuous rotation during the sputtering process, which helps homogenize deposited films, and the sample mounts distance from the guns can be varied. Heating lamps and a thermocouple behind the substrate holder maintain the desired deposition temperature of the substrate.

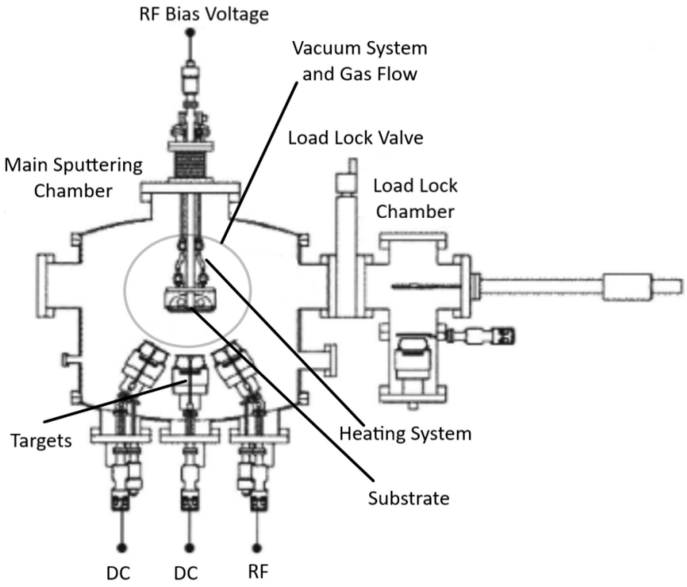

Figure 2.5. Schematics of a typical AJA sputtering system. Both RF and DC power supplies are used for the guns in this setup. The details of the vacuum and gas control systems are omitted. Redrawn from [130].

There are two RF sources and a DC source available, allowing for the ability to sputter more than one material at once. An RF bias is attached to the sample holder, which allows for the substrate or deposited film to be sputtered off of for cleaner and higher quality surfaces. The RF sources use an automatically adjusting load and tuning set of capacitors in an 'L' configuration, with a matching network that has the ability to detect the magnitude and phase of the incoming RF signal from the plasma and adjust the impedance load accordingly.

2.6 DC Electrical Transport Measurements

Transport measurements are a way to measure the carriers in a system, which can determine many valuable pieces of information about the material that is being measured. This includes resistivity, hall coefficients, dielectric constants, carrier concentration, and many other important physical attributes. Which of these qualities can be measured, and how accurate the measurement will be, depends on the type of measurement setup, the sample geometry, and the

measurement probe geometry. In our work we were solely concerned with the electrical transport properties with respect to vanadium oxide phase transitions, which manifest themselves with a strong change in resistivity, so we will focus on these types of measurements.

There has been much literature, and some debate, over the most efficient ways of measuring the resistivity of thin films.[131–133] Most commonly a simple collinear geometry is used; however, either etching films into a thin bar geometry, or using van der Pauw geometry (perpendicular applied current and voltage measurement probes), are both considered measurement geometries which produce more accurate results. Many groups use a hybrid of these to geometries by etching films into clover leaf patterns, sometimes with branches only connected by thin strips similar to the bar technique, with a probe on each branch. These types of geometries also help minimize the effects of contact resistance; however care still needs to be taken with contact size, shape and adhesion for optimal accuracy.

For our research we were mainly concerned with the quality of the VO_2 or V_2O_3 transitions; because the transition is so large, simply measuring the resistance change is sufficient to get an accurate reading of the transition. The high resistance of VO_2 and V_2O_3, even in their respective metallic states, means that contact resistance can be considered negligible in comparison, assuming care is taken with the probes.[134,135] Because of this, we are able to use a simple two probe setup instead of any of the more accurate 4 probe setups described above. Probes are directly attached to the samples using indium solder.

Most resistance vs. temperature measurements were taken in atmosphere with VO_2 films adhered to the sample holder with conductive tape. For this case a heating element was affixed to the bottom of the sample holder and a platinum RTD temperature sensor was used. We used a thermally insulated box to reduce noise due to thermal fluctuations. A Lakeshore Model 335

Temperature Controller was used to control the heater and the thermometer, and temperature was changed at a rate of 1 K/min for both heating and cooling. Because there is no cooling system for this option at temperatures close to room temperature, below 310 K this rate is much slower. This does not affect the consistency of measurements since it's 20 K away from the VO_2 transition temperature range. Resistance measurements were taken by applying a current using a Keithley Model 6221 Current Source, measuring the voltage response using a Model 2182A Nanovoltmeter, and then using the simple Ohm's Law, $R = \frac{V}{I}$. The current was usually set at 10 μA, however some more conductive samples required a smaller current of 1 μA. All electronic systems were simultaneously controlled using a custom LabVIEW program.

For bulk solids, doped samples with transitions closer to room temperature, and samples which required optical measurements simultaneous to the resistance measurements, a separate sample setup inside of an optical cryogenic capable vacuum chamber was used. The chamber is a part of a commercial cryogenics system, Cryostation by Montana Instruments, which can provide a ~1 mTorr level vacuum and can reach temperatures between 3 K and 400 K. The resistance measurements were performed identically to the in air setup. Vacuum was kept below 300 mTorr for all measurements, often on the order of 10 mTorr for lower temperature measurements. Temperature was still controlled with the Lakeshore Temperature controller, however the thermometer in this case was a Cernox style thermometer with a working temperature between 20 K and 380K. Both a heating element and a helium cooling system was available, allowing for precise temperature control both above and below room temperature. A different custom LabVIEW program was built to control the electronics for these types of measurements.

2.7 X-ray Diffraction

Since the early 20th century it has been known that x-rays focused on crystalline solids reveal a characteristic diffraction pattern, which corresponds to specific atomic orders in a crystal. X-rays wavelengths are on the order of atomic spacings, making them ideal for the probing of crystalline solids. They can also be chosen to be low enough energy to be relatively nondestructive. W. L. Bragg first explained x-ray diffraction with a simplistic model where he considered the crystal as being formed of planes of atoms. Figure 2.6 shows an illustration of simple Bragg diffraction, where d is the distance between lattice planes, and θ is the incident angle of the x-ray. According to this model, constructive and destructive interference between x-rays reflected by planes and their nearest neighbors occur when the path length difference is integer or half integer multiples (respectively) of the incident wavelength. The well-known expression that Figure 2.6 represents is

$$2\,\mathrm{d}\sin(\theta) = \mathrm{n}\,\lambda \qquad 2.1$$

Here n is any positive integer corresponding to the order of diffraction, and λ is the wavelength of the incident x-rays. Any given crystalline structure can have many different possible crystalline planes, therefore by looking at different angles a unique pattern emerges based on these unique crystalline planes.

A more generalized method of considering this phenomenon was given by von Laue. This method involves considering the crystal to be a 3 dimensional lattice of discrete points where atoms are located, called a Bravais lattice, as well as looking at the relationship between the primitive lattice vectors (**a**, **b** and **c**) and the incoming and diffracted wavevectors of the x-rays ($\mathbf{k_{in}}$ and $\mathbf{k_{out}}$). The primitive lattice vectors are what describe where atoms are located in the

lattice, where atoms are located at points given by $\mathbf{x} = p\mathbf{a} + q\mathbf{b} + r\mathbf{c}$ and p, q, and r are any integers. The change from incoming to diffracted wavevectors, $\mathbf{\Delta k}$, is called the scattering wavevector. Certain conditions between these properties must exist for constructive interference to occur. These are known as the Laue equations,

$$\begin{aligned} \mathbf{a} \cdot \Delta\mathbf{k} &= 2\pi h \\ \mathbf{b} \cdot \Delta\mathbf{k} &= 2\pi k \\ \mathbf{c} \cdot \Delta\mathbf{k} &= 2\pi l \end{aligned} \qquad 2.2$$

Where h, h and l have to be integers for the constructive interference to occur. These are known as the Miller Indices, and are often used to relate peaks in the diffraction pattern to the crystalline plane.

Crystallite sizes are also able to be estimated using x-ray diffraction using the Scherrer Equation,

$$B = \frac{K\lambda}{L\cos\theta} \qquad 2.3$$

where B is the Lorentzian peak broadening, λ is the wavelength of x-ray, θ is the angle, and K is the Scherrer constant, which is dependent on the shape of the crystallites. The derivation[136] of this formula is simple, but requires discussion of the structure factor, which is a complicated subject. Therefore this derivation will be omitted. Given this formula, peaks can be fitted for angular position and broadening, and thus with the knowledge of the incident x-ray wavelength the particle size L can be estimated. Some knowledge of the shapes of the crystallites is preferred of course, as depending on how spherical or elliptical the crystallites are, K can vary from

0.85-0.99. Perfectly spherical would correspond to 1, however most crystallites can be approximated as being around 0.94-0.98.[137] Crystallites with high deformation can of course have much lower K, but this is a more rare case.

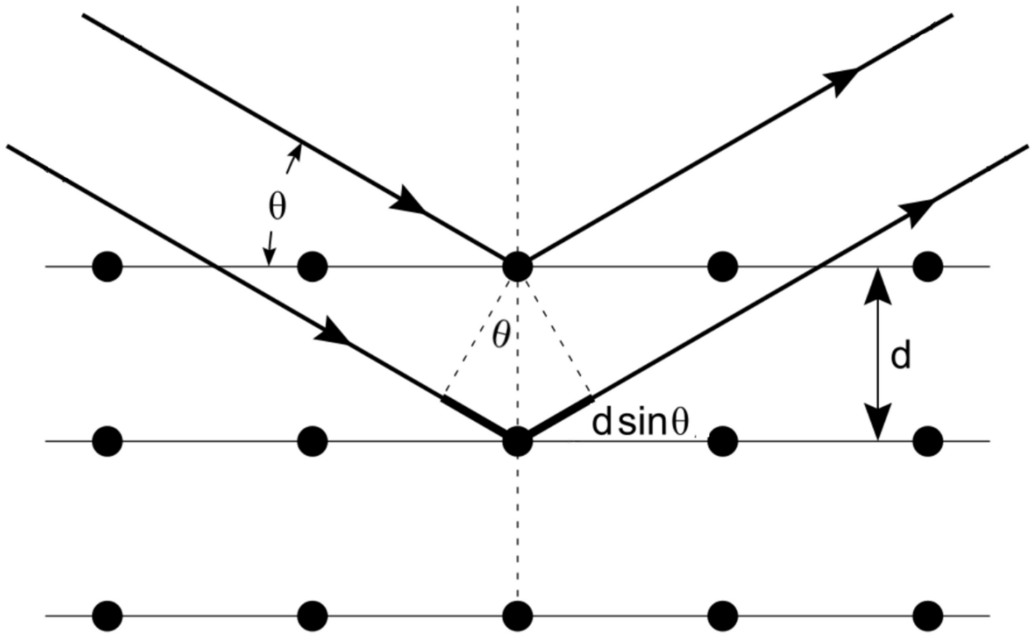

Figure 2.6. Illustration of Bragg diffraction. The incident x-ray comes in at an angle of θ, and reflects off planes of atoms with spacing d between them.

Equipment setups for XRD can range from extremely simple to quite complicated. In the simplest incarnation, a setup will consists of an X-ray source, a sample holder, and a detector; however more complicated setups can add features like temperature control, vacuum chambers, and filters. A simple setup, which includes the most common types of collimating slits, is displayed in Figure 2.7. For our analysis, two different setups had to be used for the different types of samples that were measured in our work.

For thin films we used a Bruker D8 Series-I X-ray Diffractometer. X-rays are produced with a copper source using a cathode ray tube. The Cu source emits 3 different wavelengths, $K_{\alpha 1}$, $K_{\alpha 2}$ and K_{β}. K_{β} is eliminated with a Ni filter, however the two K_{α} lines are too close together to

separate practically. For this same reason, distortions in the signal are not typically noticeable unless higher angles are used. After the beam is filtered, Söller slits are used to absorb stray beams in a way that does not fluoresce in the energy range of interest. This decreases the intensity but improves the quality of the incident x-ray beam significantly. These incident x-rays are next spatially collimated using a divergence slit, which is a slit used to limit the divergence of the incoming beam. Next, the rays reflect upon a Göbel mirror with a divergence of 0.05°. A Göbel mirror is a type of parabolic mirror that reflects the divergent rays of the beam into a parallel set of rays, allowing for precise alignment to thin film samples. The x-rays will then be incident upon the sample itself. The sample holder consists of a low diffraction Al backplate with a vacuum system attached that allows for directly affixing samples without the use of adhesives; the system is also equipped with a full Eulerian cradle, allowing for the sample holder to rotate along all 3 possible axes. The beam next passes through another slit called an anti-scatter slit, which serves to both reduce divergence in the scattered beam and get rid of any diffusely scattered x-rays. After this, a receiving slit is used to further reduce divergence and diffuse scattering. Although the slit widths can be varied from .1-2 mm depending on the type of measurement and sample being measured, a general rule is to always make the anti-scatter slit larger than the receiving slit. A second Söller slit is used before the detector with the same purpose as the first. The scattered rays finally collect in a NaI detector. Both source and detector arms of the setup are capable of 180° rotational movement in the x-z plane of the system. The Eulerian cradle allows for 0.005° increments of adjustment in the angular directions for the sample holder and the detector arm, while the sample holder allows down to 0.01 mm Cartesian adjustments.

The use of a Göbel mirror puts this system in the Parallel Beam Geometry, which means there is no limit on the measurement orientations available. Typically measurements are taken using a θ/2θ configuration, wherein the x-ray source and detector arms are coupled in rotation about a fixed radius to maintain the θ/2θ geometry. This produces a simple x-ray profile across a wide range of rotation angles. There are many other orientations that are possible and are more useful for other types of data collection, such as 2θ measurements for 2-D crystal structure and ω(perpendicular-beam angle)/2θ for grain size. However in our work we solely analyzed samples using the θ/2θ measurement technique. A problem arises when measuring thin films, in that the crystalline structure of the much thicker substrate will drown out the thin film measurement. To maximize the signal to noise ratio for film measurements several steps must be taken. First a scan of a pure substrate must be taken so that we can understand which peaks belong to the substrate only. Next, we must align the x-ray beam to the film itself as accurately as possible in the x, y and z axes. Then a rocking curve scan must be collected, which is a scan that involves leaving the source and detectors fixed at angles which should correspond to a crystalline peak we would expect to observe for this sample, and then varying the ω angle (the sample holder's angle) around this to find the maximum intensity. Adjusting the ω for maximum intensity in turn adjusts the θ/2θ geometry slightly, making the incident rays more aligned with the film instead of the substrate. Finally, collection time and step size of the angle change can be varied to adjust for either quicker less detailed scans or higher resolution data that takes longer periods to collect.

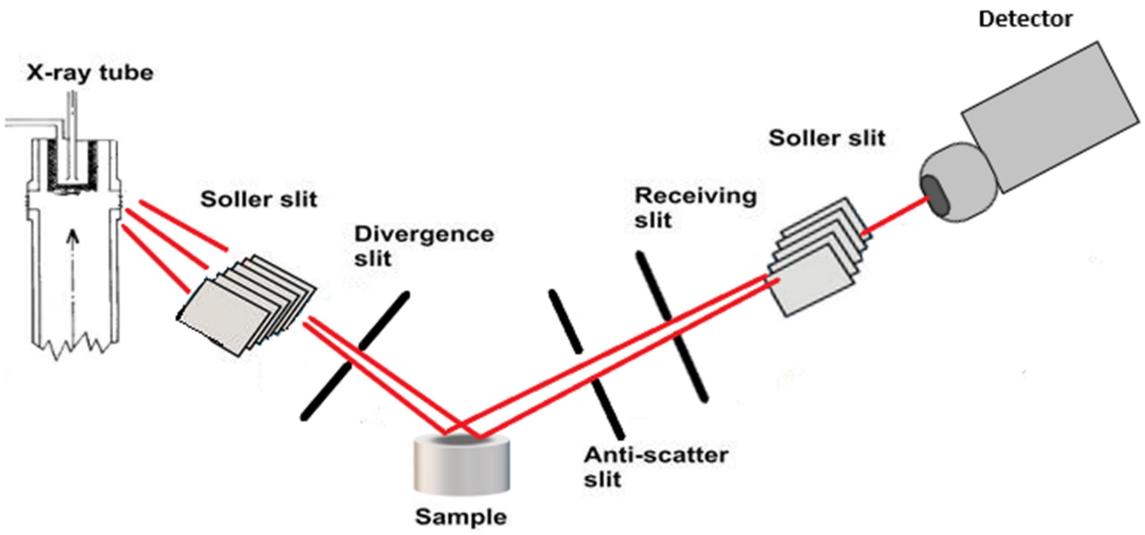

Figure 2.7. Diagram showing the basics of an x-ray diffraction setup. Söller slits are not always necessary, and the divergence, anti-scatter, and receiving slits need to have certain widths for different types of measurement scans. Oftentimes monochromators will be used before the detector as well.

The second system used in our work was a state of the art Bruker D8 Discover DaVinci. This setup is very similar to the Series I with a few key differences. The DaVinci system used is intended mainly for powder samples, therefore there is no reason to include a Göbel mirror. This is the most common form of x-ray geometry, known as the Bragg-Brentano geometry, where divergent beams are focused on the sample and then refocused into the detector. The detector is a state of the art LYNXEYE-XE-T energy discriminating detector. This is a compound silicon strip detector with 192 channels that has internal monochromators, allowing for extremely high resolution data to be collected very quickly. The sample holder is also significantly different, allowing for up to 9 samples to have data collected in series. However there is little control over the position of the sample holder in this system, as it will only allow for changes in the ω angle and rotation in the x-y plane. The sample pucks themselves are what hold the sample in this system, and we used a zero diffraction plate for each sample. Samples were affixed by soaking

them in a solvent and letting them dry on the plate. A knife edge is used to reduce low angle noise and the sample plane rotation is used to reduce the effects of preferential orientation.

Before we close this section, there is one more technique of interest to discuss, X-ray Reflectivity (XRR). XRR is usually used to determine film thickness, but can also be used to determine information about the surface and interface roughness, as well as the chemical composition. All XRR measurements were taken using the Series I system. Alignment procedures are repeated at higher resolution for XRR due to its much higher sensitivity. The rocking curve scan is performed with 0.1 mm slits across angles lower than critical angle (usually less than 0.5°). The measurement scan is still a θ/2θ scan but the range is typically much lower angles, from 0.1-5°; however thinner films may need to collect data up to 10°. In the case of XRR, data collected is an effect of the reflection, and what is observed are oscillations of decreasing intensity, referred to as Kiessig fringes. These fringes can be interpreted as interference due to a path difference between the rays reflected at the surface of the film and the interface between the substrate and the film. This phase difference can be calculated as

$$\Delta = 2t\sin(\theta) \qquad 2.4$$

where t is the thickness of the film and theta is the angular difference between fringes. Thus this formula can be used to estimate the thickness given XRR data. More complicated analysis using advanced software can be used to fit XRR data; however we will omit that discussion here because this was not used on the samples that will be presented.

2.8 Electron Microscopy Techniques

2.8.1 Scanning Electron Microscopy

The advent of electron microscopy is one of the most important developments of a measurement technique that took place in the 20th century. It brought the ability to image materials down to the nanometer scale, increasing the possible magnification from the 1500x possible for light microscopes by three orders of magnitude to 100000x. There are many different types of electron microscopy, such as transmission electron microscopy (TEM), scanning electron microscopy (SEM), scanning tunneling electron microscopy (STEM), reflection electron microscopy (REM) and several other possible techniques that are actively under development. This discussion will be limited to SEM, as it is a cheaper and more user friendly technique than the others, and can give us valuable information about morphology more quickly than its counterparts. SEM is a surface sensitive technique, allowing for the imaging of the surfaces of samples of interest. SEM is typically only used to measure solids, because the high vacuum required would cause immediate evaporation of any liquids. These can be either inorganic or organic solids, including dry biological samples.

The mechanism behind imaging in SEM is the interaction between an electron beam with some material. There are many different types of interactions that can occur. The main interactions that occur are elastically scattered electrons, which scatter of the surface in elastic collisions. If they scatter back from the surface, they are referred to backscattered electrons (BSE), and can be used as a signal for imaging the sample. They are most useful for determining roughnesses and atomic order of samples, and are energetically defined as having energies above 50 eV. The most widely used signal for imaging comes from the secondary electrons (SE), which

are electrons that were loosely bound in the sample material that will be released by the energy imparted by the electron beam. Conventionally they are defined as possessing much lower energies than the BSEs, typically far less than 50 eV, with an average around 3-5 eV. Because the energy is so low, they can only escape from surfaces up to a few nanometers in depth, and are thus ideal for topographic mapping. SEs are able to resolve structures down to about 10 nm. There are several other processes that occur besides BSEs and SEs, but the one that has the most effect for SEM measurements is Auger electrons. When electrons are released from an atom, a higher energy level electron will fill it and release energy, which occasionally is released in the form of an electron instead of a photon; these are called Auger electrons, and must be accounted for when trying to collect a signal. The same process also generates x-rays due to excitation, which can be used for a spectroscopic technique; this will be described in more detail in the next subsection.

The source for the electrons is an electron gun, which can emit and then accelerate electrons to energies from 0.1-30 keV. Traditionally tungsten filament cathodes were used for this, however in modern times improved sources known as field emission sources were designed and used to create the field emission gun (FEG). FEGs have both enhanced current and lowered energy dispersion compared to their predecessors. FEGs have a single crystal W wire with an electrolytically etched fine tip. Because such strong fields are created at this tip, electrons will be drawn towards anodes instead of having to be thermionically released. The most common type of FEG is called a thermal field emission (TFE) source, which is heated both to improved electron emission stability and reduce the absorption of gas molecules. As mentioned previously, a high-vacuum environment is required, both because the gun needs to remain extremely clean in order

for it to not be contaminated, and also because the electrons need to accelerate unimpeded through the sample chamber for emission and detection.

The electron beam will disperse as it moves towards the sample, so electromagnetic lenses and apertures have to be used to collimate and focus the electrons onto the collection area. Magnetic lenses are used to change the beam diameter, effectively allowing for a variable focal length. These lenses are usually just pole magnets generated electromagnetically with variable field, placed so that the electron beam passes directly through the strongest area of the field. Generally, there are two main lenses that are used, a condenser lens and an objective lens. After passing through the anode from the electron gun, the beam will start to diverge. The condenser lens converges and collimates the beam so that it is effectively parallel. The objective lens is used to focus the beam onto the sample surface in the specific area which is to be imaged. Depending on the design of the instrument, several apertures may be used. Apertures main role are to block scattered electrons, however they also help correct spherical aberrations. These components still leaves aberrations however, and an elliptical spot is produced; this will cause overfocusing along one axis and underfocusing along the perpendicular axis. This is known as astigmatism. Another component, a series of coils called a stigmator, is added to correct for this. One last thing to consider in this part of the setup is the working distance, which is the distance from the front of the objective lens to the surface of the sample when it is in sharp focus. This mainly influences depth of field, which is the depth of the sample structure that is able to be focused. Working distance basically determines whether the depth is shallow or deep, and should be changed depending on whether a sample is flatter or has more roughness (or out of plane structures).

Several detectors are used to collect the different signals in an SEM. SE detectors are typically Everhart-Thornley detectors, which are filtered for the SEs energy range. Scintillation is used to convert the signal into photons, which then travel through a light pipe outside of the chamber to be converted to electrons once again by a photomultiplier tube. The voltage produced is what is used to construct the image. SE detectors are placed at different points throughout the sample chamber depending on the design, trying to optimize signal to noise ratio. BSE detectors are often left retracted unless needed, and are also placed at a point for optimal signal to noise ratio depending on the sample chamber design.

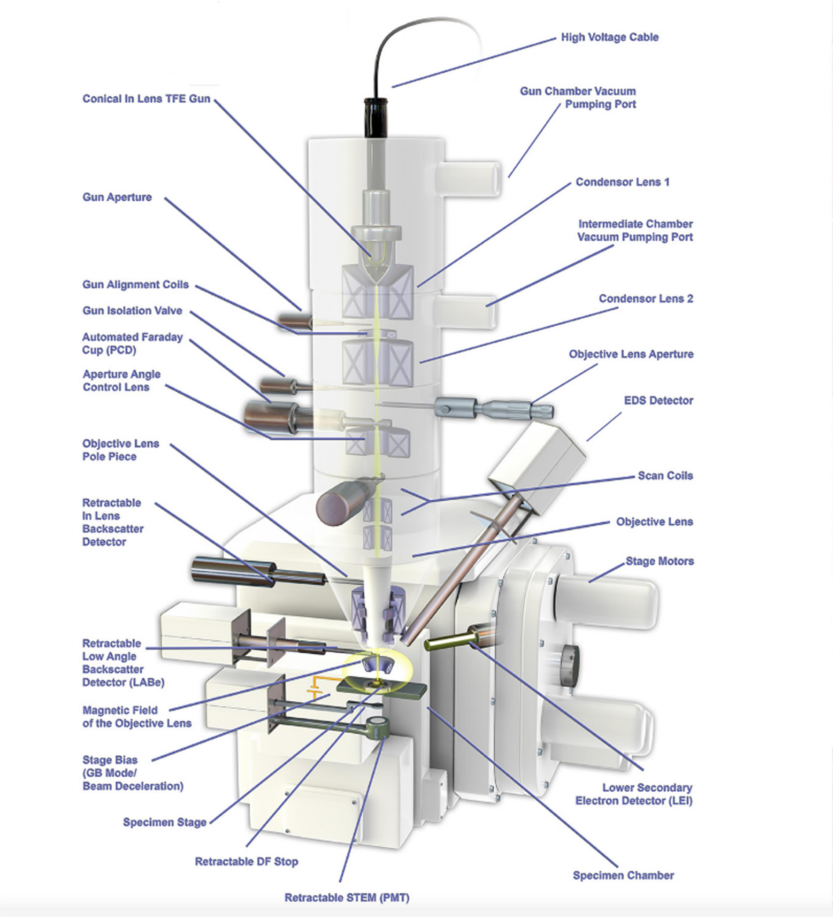

Figure 2.8. An example of a JEOL SEM system with EDS option installed. (Courtesy: JEOL)

The system used in our research was a JEOL JSM-6500F. An example of a typical JEOL SEM setup is shown in Figure 2.8, with detailed schematics on the components. A conical in lens TFG is used as the electron source, with two condenser lenses and one objective lens. Three apertures are used across the column. Two SEs and two retractable in lens BSEs are installed. The sample stage is a eucentric large-specimen stage with full in plane sample control to move the collection area, and out of plane rotation abilities from -10-90°. Pressure in the sample chamber is typically less than 2×10^{-4} Pa, as this is what is required for the gun to operate safely. An EDS detector is installed, which will be discussed in greater detail in the next subsection.

Samples themselves have to be prepared properly for the measurements to be successful. As discussed above, only dry samples may be measured due to the high vacuum requirements. Biological samples must be properly dehydrated before any measurements can take place; the different ways of preparing these samples will not be discussed, since only dry inorganic samples were measured. Sample surfaces must also be conducting. This is very important, as electrons must be able to freely travel across the surfaces for SE production to take place. However, this does not mean that only conducting materials can be measured. Insulating materials simply need to be coated in a conducting material while also preserving the structures that are desired to be imaged. This must be done carefully, for if the material is not conductive enough then this will result in charge buildup, which ultimately results in either the destruction of samples as they are imaged, or too low of contrast. This is normally done, and in our research this is no exception, by sputter coating gold onto the samples. A tabletop sputtering chamber was used to sputter 2-3 nm of gold on our samples. Once samples are coated they are affixed to aluminum pin stubs, and placed in the sample holder. Insulating samples, or films with insulating substrates, must be grounded to the sample holder or charge buildup will occur.

2.8.2 Energy Dispersive X-ray Spectroscopy

Energy dispersive x-ray spectroscopy (EDS) is a technique that is used for elemental analysis of surfaces with spatial resolution. It is very similar to other x-ray spectroscopy techniques in principle, but by combining it with the surface imaging capabilities of SEM it allows for elemental analysis of specific structures in the sample. Like similar techniques, it relies on specific elements having a unique electron structure, so that there is a unique x-ray excitation spectrum characteristic to each element. Some of the electrons incident on the sample from SEM will excite the sample at specific wavelengths, and the resulting x-ray emissions can then be correlated to the same sample area that was being imaged. To get a full spectroscopic scan of an area, the electron energy is varied from 0 eV to the desired maximum, usually that max rated to the system. Probe current is usually increased to get better quality x-ray signal. Our data was analyzed using the INCA software package. For all samples, the total elemental analysis is taken first, and then several points of interest. A full area scan follows depending on results.

It is important to note that many researchers also consider this technique useful for determining the percent composition for different elements. This type of analysis requires the samples collection to be very ideal in comparison to the process we chose. Usually only films or other high quality surfaces are chosen, and even then they often need to be polished in order for accurate analysis to be performed on the resulting data. Thus all percent composition data shown should not be trusted as a rigorous analysis of the percent composition.

2.9 Profilometry

2.9.1 Stylus Profilometry

There are many different techniques beyond electron microscopy to determine surface properties of films. One of the simplest techniques is stylus profilometry, wherein a stylus probe is physically moved along the surface in order to acquire the surface height. This is done purely mechanically, while a feedback loop monitors force from the sample pushing up against the probe as it moves across the surface. The feedback system keeps the arm with a specific amount of torque on it so that changes in the z position of the arm holder are then directly able to record the z positions across the surface. Because this technique requires a force to be applied while physically touching the surface, the probe can become contaminated by softer surfaces, and the surfaces can even be damaged. It is also slower than most other techniques since it involves physical movements along all three axes of the sample while maintaining physical contact with the surface. The stylus' tip's size and shape also have an influence on the measurements and can limit the degree of lateral resolution. Although this technique is simple, and it is quite easy to perform and analyze the data, the resolution for smaller surface structures is not very high compared to many other comparable techniques. Therefore this technique was only used in our work to test sample thicknesses of our thicker sol-gel samples, while other techniques were used to analyze smaller surface structures and roughnesses. The machine used was a Tencor P-10 Stylus Profilometer, with a tip radius of 12 μm used.

2.9.2 Atomic Force Microscopy

The higher resolution surface imaging technique known as atomic force microscopy (AFM) was used to analyze the grain size and shape, as well as the roughness, of our thin film samples. AFM actually stems from another technique called Scanning Tunneling Microscopy (STM), which uses a sharp tip held at a certain voltage and measures the change in tunneling current across the surface to measure the surface features z-positions instead of directly contacting them. Unfortunately this can only be used when the surface being measured is conducting. AFM was developed by instead using a profilometer tip with the STM setup, and unlike stylus profilometry relies on changes in the van der Waal force coupled with a piezoelectric to detect changes in the surface structure. Thus it overcomes the limitation of conducting surfaces. AFM has developed to be able to be used in a large variety of ways to measure different types of samples, including metals, insulators, nanoparticles, biological samples, and samples dispersed in liquids. Magnetic tips can even be used to modify an AFM into a Magnetic Force Microscopy setup, which is able to map out magnetic domains of ferromagnetic surfaces, among other things. AFM systems currently available can have lateral resolutions down to 5nm, and z-axis resolutions down to 30 pm. AFM has several different modes of collection, with the main two modes being contact mode and tapping mode. Contact mode is when the tip is directly against the surface, whereas in tapping mode the tip oscillates at a set frequency against the surface. Tapping mode has the advantage of not wearing the tip (or the surface) since it only makes contact at the bottom of the oscillation. It also reduces the chance of the tip breaking when there are larger z changes. Our discussion will be limited to tapping mode, as this was the method used for all data sets collected.

Figure 2.9 shows the basics of an AFM setup, with the inset showing the difference between tapping and contact mode. The surface probe is a cantilever with a micromachined tip

on one end. This cantilever is vibrated by the piezoelectric element at the resonant frequency of the installed tip. As seen in Figure 2.9, the actual measurement is taken by shining a laser on the back of the cantilever, from which the reflection is sent to the photodiode. The change in this reflection as the cantilever oscillates is a measurement of the z-position. Basically, an AC voltage is produced and converted to a DC current. This DC current varies with the surface height since the deflection of the cantilever will vary depending on how far the cantilever tip has to go to reach the surface. There is a piezo controller below the sample which controls the motion of the sample through the scan.

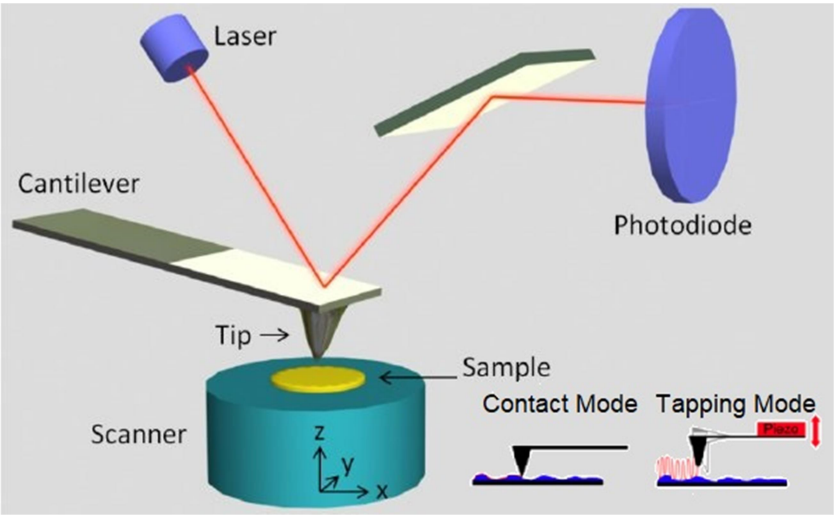

Figure 2.9. Illustration of basic AFM system components and the two main modes of operation. Inset shows the two different operating modes. Modified from [138].

Two different systems were used for our measurements, an Innova system and a Bruker Bioscope Resolve, however the only real difference in their setups were the resolution and speed at which measurements were able to be taken. The tips used for both systems were RTESPA-300 tips, which are silicon based with an aluminum reflective coating on the back for increasing laser reflection. These are rated to have a cantilever width and length of 40 ±2 microns and 115 ±10

microns respectively, and have a resonant frequency of 300 ±100 kHz. The tip radius itself is rated for 10 ± 2 nm (compare to the much larger stylus profilometry tip radius).

Unlike normal images, not just x and y data are stored in AFM images but z data as well. The Gwyddion software package was used to analyze all AFM images presented in this work. Data was leveled using mean plane subtraction, and polynomial backgrounds were removed. This helps correct for piezo nonlinear bowing, and will remove any height gradient due to the sample not being completely in a z-plane with respect to the tip. Any horizontal aberrations are removed and any rows shifted are aligned. Limits are then set on the minimum and maximum of the z-data to both remove possible erroneous data points and to help smooth out the data for analyzing more efficiently. Roughnesses are then extracted from the images. Finally, if grain size analysis is necessary, a minimum and maximum grain size are set, shape quality parameters are set, and a watershed algorithm is used to mark the grains within a certain threshold to determine their mean diameter. A watershed algorithm is one in which simulated droplets are dropped onto the surface and their paths are traced to determine where grains and valleys are located. Droplet size and the degree to which we would expect the grains to be segmented are varied to get the best thresholding possible.

2.10 Magnetometry

Magnetometry measurements were possibly the most important measurements that were needed to be taken in this work, as two of the main projects that will be presented have motivations completely based on desired magnetic properties of materials. Thus consistent and precise measurements needed to be taken to get accurate magnetizations of our materials. Two different magnetometry techniques were used to make two different types of measurements of

our samples. The first is known as Vibrating Sample Magnetometry (VSM), which we used for magnetization as a function of applied magnetic field measurements (M vs. H). The other technique is known as superconducting quantum interference device (SQUID) magnetometry, which we used for magnetization as a function of temperature measurements (M vs. T). VSM is ideal for taking M vs. H measurements because the field can be changed very quickly, and magnetic moment measurement is accurate enough to be useful in determining the shape of hysteresis over the short measurement collection time. Unfortunately, however, the vibratory nature of the technique makes it less ideal for longer measurements at a set field. This is mainly due to microstructural changes in the materials as well as sample shifting. When measuring powder, even tightly packed, visible distortions appeared due to physical shifts in the particles. Even with films however, any inhomogeneity is clearly visible in many samples due to shifting, even when textbook fixture techniques are used. To avoid this problem SQUID magnetometry used for these types of measurements instead. SQUIDs are well known for having extremely high accuracy magnetic moment measurements, with the capability of measuring the magnetic moment of single particles.

2.10.1 Vibrating Sample Magnetometry

VSM magnetometry is conducted by first applying a field to a magnetic material, usual using a variable electromagnetic. The material is then vibrated the between pickup coils (measurement coils), which by Faraday's law will cause an emf in the coils due to the changing flux. By using a sinusoidal signal we can express this induced emf as

$$V_{induced} = \omega C m A \sin(\omega t) \qquad 2.5$$

where ω the frequency of oscillation, m is the magnetic moment of the sample, C is a constant to account for the measurement geometry, and A is the amplitude of oscillation.

The VSM system used for this work was a module of Quantum Design's Physical Properties Measurement System (PPMS). A diagram showing the components of this specific system is displayed in Figure 2.10. Film samples are attached to a quartz sample mount, usually using vacuum grease as an adhesive, but sometimes by using Kapton tape for more delicate samples. Powder samples are instead sealed in a plastic capsule, and the capsule is fixed in a high purity bronze sample mount. A carbon fiber (which has a low thermal expansion coefficient) sample rod is used to hold the sample holder in the high vacuum system in the vicinity of the pickup coils. This sample rod itself is placed through a sample tube that acts as a low friction guide for the rod during the vibration, and in turn helps reduce the vibrations transmitted to the measurement coilset. The sample is vibrated at a frequency of 40 Hz with amplitude of 2 mm by attaching the top of the sample rod magnetically to a linear motor. The position of the motor is measured by using an optical linear encoder, and this measurement allows the samples position to be measured with accuracy down to 0.1 micron. The coilset in this system is a first order gradiometer with two coils spaced 7.1 mm apart. A single coil has an inner radius of 3.865 mm, an outer radius of 6.85 mm, and is 1.7 mm thick. The coilset is contained in what is called a sample puck, which contains other devices used in the measurements as well.

The sample chamber can be pumped down below 10^{-4} Torr under normal working operation, and much lower at lower temperatures. In the normal option the sample puck has heaters and a thermocouple to control temperature above room temperature, with max operating temperature reaching 400 K. However an oven option can be installed to go to temperatures as high as 1000 K; results presented in this thesis did not require such high temperatures so this will

not be discussed in detail. A helium cooling system can also allow for cryogenic measurements down to 1.9 K. The applied field is due to a variable electromagnet immersed in liquid helium that surrounds the sample chamber, but is separated by several vacuum tubes. The electromagnet in this system is rated to 9 T.

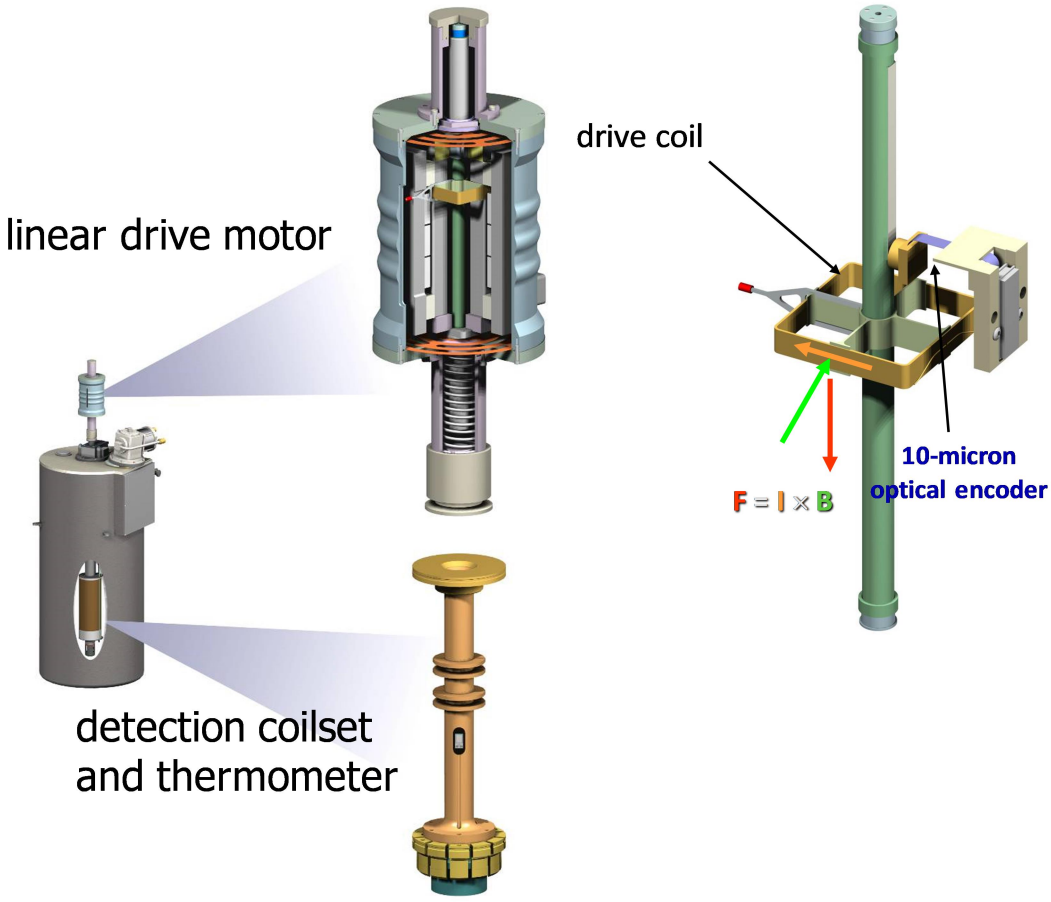

Figure 2.10. Schematic of VSM option in a Quantum Design PPMS. The outer components, which includes the electromagnet, is excluded to highlight the detection setup. (Courtesy: Quantum Design)

To make sure measurements have a strong signal, centering on a sample must be done. This requires correct sample mounting to be in the right range for the measurement, but otherwise simply requires a field to be applied and to find the area of maximum signal. However because our measurements require collection of data at different data points, the sample should

be remeasured each time the temperature is changed to minimize errors due to thermal expansion and contraction. Before any measurements are taken on a sample the electromagnet is put through a demagnetization process to reduce any remnant fields. This demagnetization process is treated more rigorously for powder samples, as they require higher fields. For our experiments the data points that are collected are averages of 40 measurements every second. Temperature is allowed to stabilize for up to 30 min before data collection, depending on the proximity to room temperature.

2.10.2 Superconducting Quantum Interference Device Based Magnetometry

SQUIDs are formed by connecting two superconductors separated by only two thin insulating layers, forming what's known as Josephson junctions, such that the junctions are parallel and the superconductor assembly forms a ring. The physics behind these junctions are very complex, but they can be described as junctions that allow Cooper pair tunneling. The current and voltage associated with this tunneling rate is predictable based on how many quantum pairs tunnel through. This quantum relationship between the tunneling and current/voltage had direct implications that flux changes must also be quantized in this relationship as

$$\Phi = \frac{2\pi\hbar}{2e} \qquad 2.6$$

SQUIDs function on this principle by applying a constant biasing current, so that the measured voltage will oscillates with any changes in phase at the two junctions. This in turn depends upon the change in the magnetic flux, so counting the oscillations allows one to evaluate the flux change which has occurred.

For our work we utilized a Quantum Design XL model Magnetic Properties Measurement System (MPMS-XL) SQUID magnetometer. Although it has an AC collection mode, all measurements were taken using DC mode. Samples are mounted in normal food grade Dixie straws, which have negligible magnetic moment compared to samples. Powders require the extra step of packing into cellulose capsules before being mounted in a straw. A sample rod, similar to the one in the PPMS, is used to place the sample into the correct position in the sample chamber. The straw is affixed to this with both a ferrule and Kapton tape. The sample must pass through a load lock chamber to prevent contamination of the sample chamber, and then the rod must be clamped in place with a Swagelok when the sample has reached the measurement area. Any further height adjustments can be made using the electric motor that controls the sample height. Similar to the PPMS VSM described above, samples have to be centered once they enter the chamber. This process is basically identical, with the difference lying in how the magnetic signal is collected. There is a heater in the chamber to allow for heating up to 400 K; two thermometers are used, one at the measurement site and the other at the bottom of the chamber. It's possible for temperatures to reach down to 1.9 K when cooling using the helium gas cooling system.

In the case of the MPMS, the samples are not directly passed through a SQUID like in many other setups. For this system a 2nd order balanced gradiometer is used for detection, using 2 sets of coils on axis 3 cm apart. Samples are not vibrated but instead moved at a much slower pace through the coils to induce a signal. The induced voltage will drive a current through an inductor to generate the flux to be measured by the SQUID. A superconducting RF interference isolation transformer is used to prevent erroneous flux jumps. Similar to the PPMS, the magnetic fields are produced using a variable electromagnet immersed in helium that is insulated from the

sample chamber. Although the field is much more stable than in the PPMS, it takes much longer to charge the magnet than in the PPMS, and changing fields can take over 10 times longer. The precision of the field is typically on the order of 0.1 mT.

2.11 Optical Wavelength Reflectometry

Reflectometry is a measurement technique which can be used to determine a large variety of physical properties. A simple definition is that reflectometry is the measurement of electromagnetic waves reflected from an interface in comparison to the initial waves incident on the interface. These measurements can be done in many different ways, depending on the way wavelength, polarization, and intensity are controlled for and measured. X-ray reflectometry is a technique that was already discussed above, which can determine quantities like roughness and thickness of films. Other common reflectometry techniques include radar/lidar techniques for determining positions, ultrasonic techniques used in medicine and geology, and neutron reflectometry which can be used to determine similar quantities as XRR but with magnetic resolution. The technique of interest in our work is actually a much simpler and older technique than all of these, optical wavelength reflectometry. In truth this encompasses more than the tradition optical range of wavelengths, ranging from 50 nm to 5 μm. This technique can allow for the determination of the composition, roughness, thickness, crystalline nature, doping concentration, electrical conductivity, refractive index, and permittivity of the material in question. Though there are both diffuse reflections and spectral reflections involved in these techniques, we will focus on the much simpler to measure and analyze spectral reflections. Reflections from bulk solids also require significant alterations to the calculations required to obtain useful information, and so we will also limit our discussion to the geometry of the samples of interest, thin films. We will also limit our discussion to single wavelengths and

polarizations, instead of trying to cover the full breadth of theory behind ellipsometry on top of the already lengthy calculations behind simple reflection and transmission. Thus our discussion and the work presented will be limited to spectral reflections from thin films, with single wavelengths and polarizations for each measurement.

The theory behind reflection and transmission at a single thin film interface is described in detail even in many undergraduate level textbooks, the result of which is known as the Fresnel equations. These equations take into account that a part of the ray will be reflected, the rest refracted at an interface, and accounts for phase changes and real refractive indices. There are different equations for s and p polarization. Here s-polarization refers to when the electric field vector is perpendicular to the plane of incidence, whereas p-polarization refers to when it's parallel to the plane of incidence. All of our samples were measured with s-polarization, so we will focus on these equations. The Fresnel equations for s-polarized light are given by

$$\mathrm{R} = \left(\frac{n_1 \cos\theta_1 - n_2 \cos\theta_2}{n_1 \cos\theta_1 + n_2 \cos\theta_2}\right)^2 \qquad 2.7$$

$$\mathrm{T} = \frac{4 n_1 n_2 \cos\theta_1 \cos\theta_2}{(n_1 \cos\theta_1 + n_2 \cos\theta_2)^2} \qquad 2.8$$

R and T are the decimal representations of the proportion of the wave that will be reflected or transmitted respectively. For these equations R + T = 1. n_1 and n_2 are the 1st and 2nd medium respectively, and θ_1 and θ_2 are the incident and refracted angles respectively. These equations can be modified by accounting for the complex nature of the refractive index by directly replacing them; however this will not account for the absorption effects of the medium properly. When accounting for thickness of the medium, multiple interfaces of different films, the roughness of the interface, and the absorption of films, the theory becomes far more complex

than the simple Fresnel equations. These cases will be discussed with greater detail in a later chapter.

We used an in house custom setup to take our reflectivity measurements. The sample chamber was the Montana Instruments Cryostation that was described in section 2.6 above, and measurements were taken in a manner consistent with what was described in that section, oftentimes in tandem with the electrical transport measurements. Three different wavelengths were used: 405 nm, 635 nm, and 980 nm. Thorlabs collimated CW laser diodes were used for 405 nm and 980 nm light sources. The 405 nm laser has a power output of 4.5 mW and has 1% frequency stability and 1% intensity stability. The 980 nm laser also has a power output of 4.5 mw and an intensity stability of 1%, however the frequency stability was 2% in this case. For the 635 nm diode, we used a 4.5 mW CW Premier laser diode module with intensity stability of 2% and frequency stability of 0.25%. The light became s-polarized through a linear polarizer with an extinction ratio of less than 1000/1 before hitting the sample. The angle of incidence was kept as close to 20° as was possible (within 0.2°) for all samples. Quarter waveplates were used to eliminate the effects of elliptical polarization for both reflected and transmitted waves, and an analyzer was used for both the reflection and transmission detectors. The detectors themselves were both Thorlabs PDA100A silicon diode array detectors, with detection ranges from 340-1100 nm and a peak response wavelength of 980 nm. Bandwidth of these detectors is 2.4 MHz. Gain was set at 0 for both detectors in all cases. To reduce background EM noise, an optical chopper is used to chop the beam into pulses at a frequency of 900 Hz. A lock-in amplifier is used to collect the signal from the detectors and filter out anything detected that's not received at this frequency. The sensitivity of the lock-in is varied depending on the strength of the signal. A custom LabVIEW program was used to control the signal collection, the temperature, and the

vacuum of the data collection. It was used in tandem with a custom Python program to convert the raw data into T, R, and A (absorption analog of R and T) coefficients by comparing the signal from both detectors to a reference signal that was collected at an earlier point.

Chapter 3. Magnetic Properties of Hybrid Vanadium Oxide/FM Composites

3.1 Motivation

In Chapter 1 we discussed some of the forms that magnetic hybrid structures take, as well as some methods of controlling their magnetic properties. Although these external influences have been shown to allow for a large range of control, attaining a higher degree of precision in the tuning of the various properties, as well as larger enhancements and suppressions of the properties, is still of great interest for many applications. We also discussed the specific magnetic hybrid system of a vanadium oxide/FM heterostructure, whose control mechanism is the application of strain to the FM layer by the VO_2 (or V_2O_3) layer during the VO_2 (or V_2O_3) SPT. This system has been investigated with increasing frequency due to the promising results obtained; however it is very surprising that there has been only one published study which has attempted to adapt this system for bulk solid use.[109] Bulk solids are far more appropriate for many potential applications, as they can be molded into different shapes for use in different types of equipment and are less prone to being oxidized. They can also be potentially used as precursors for large scale film fabrication if films are preferred.

This chapter will discuss our attempts to fabricate a magnetically coupled bulk vanadium oxide/FM system by using ball milling techniques and sintering. While we did not succeed in fabricating VO_2/FM, we were able to synthesize V_2O_3/FM bulk composites. We will first discuss an attempt made using just the ball milling technique to mix and alloy VO_2 and the strong ferromagnet $CoFe_2O_4$. The influence the milling has on the crystal structure and magnetics of the system will be presented, as well as the limited success obtained in trying to couple the two

compounds. Next we will present our attempt into trying to fabricate a VO_2/Ni composite system based on the technique used in Urban et al.[109], as well as the difficulties in trying to feasibly produce such a system. Finally, we will discuss our success fabricating V_2O_3/Ni composites followed by a detailed investigation into how various fabrication parameters end up affecting the V_2O_3/Ni system, and how an optimization of the magnetic coupling was obtained.

3.2 Milling of VO_2 and $CoFe_2O_4$

$CoFe_2O_4$ is a strong ferromagnetic compound but also an oxide, so it was supposed that it would be a good candidate to check if the ball milling technique could be used to structurally couple the $CoFe_2O_4$ particles to VO_2 particles. Mixtures of the compounds were attained by first taking commercially produced 99.5% pure $CoFe_2O_4$ powder, with particle sizes less than 80 nm, and commercially produced 99% pure VO_2 powder, with particle sizes less than 150 μm, and mixing them in a mortar and pestle for at least 15 min. When we refer to an unmilled or 0 hour milled sample, this is the point at which the processing of the mixture was stopped. Both 80% $CoFe_2O_4$-20% VO_2 and 60% $CoFe_2O_4$-40% VO_2 mixtures were mixed to try to see the effect that different ratios would have on resulting crystallography and magnetics of the product materials. There was little to no effect on the crystallography of samples with different ratios, and any correlation between these ratios and the magnetics, beyond the obvious difference that the mixture with more $CoFe_2O_4$ would have higher magnetic moment per weight, was not tangible. After the initial mixing, the mixed powders were milled according to the ball milling procedure described in section 2.2, using the non-magnetic zirconia milling jar and balls described. Milling times were varied from 2-12 hours. After mixing/milling, all samples were stored in a light vacuum of 100 Torr to prevent oxidation between fabrication and measurement. Jars were

cleaned with strong acids, distilled water, and solvents between samples to prevent contamination from previous samples.

We attempted to measure the electrical transport properties of the mixtures, first by forming the mixed powder into a pellet under a hydraulic press at 200 MPa, and then using the technique described in section 2.6. However a problem arose from the fact that the $CoFe_2O_4$ increased the conductivity to a point where it was extremely difficult to observe a signal difference between the insulating state of the VO_2 and the conducting state. Because of this we measured the MIT of the pure VO_2 powder before a milling process, and then milled it for 6 hours and compared the change in the MIT. This is shown in Figure 3.1, where we see that the milling process has a few distinct effects. The absolute resistance in the insulating state is lowered by two orders of magnitude, which is an effect of the particle size decrease after milling. Smaller particles means that there will be more surface area contact between particles, causing greater conductivity in the bulk solid as a whole. There is also a decrease in the change of magnitude of the resistance through the transition after milling. For the sample which was not milled there is almost a 3 order of magnitude change, whereas the milled sample only changed by one order of magnitude. This suggests that the transition is somewhat degraded by the milling process, although from the data it is not clear whether the MIT is solely being reduced, or if the SPT is as well. Finally the shape of the hysteresis is changed, although it's not clear what this may imply.

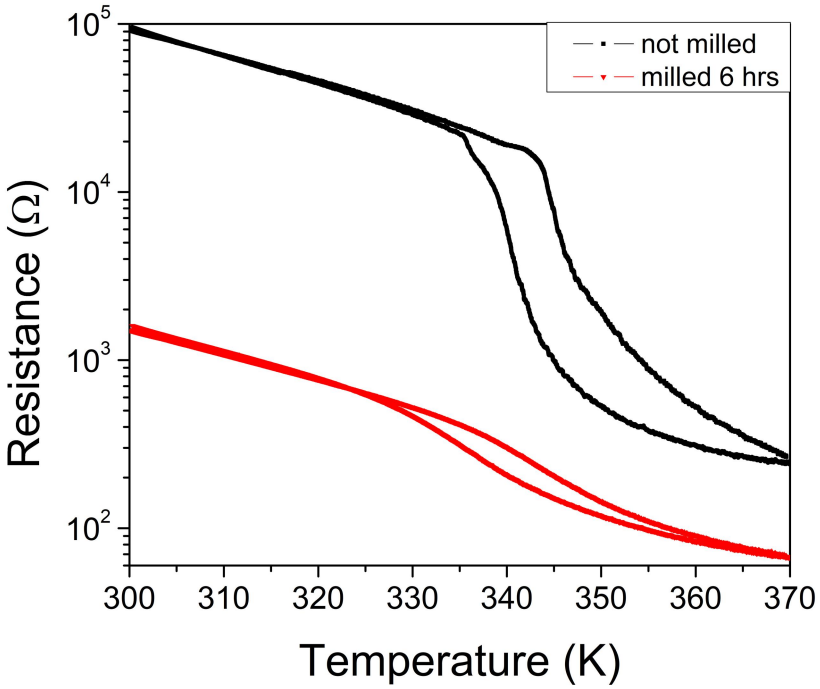

Figure 3.1. Resistance as a function of temperature through the VO_2 transition for a 6 hour milled sample and an unmilled sample of VO_2. Broadening and reduction is seen for the milled sample.

To determine how the crystalline structures of the compounds were affected by the milling process, x-ray diffraction was performed on all samples. A comparison between an 80-20 ratio, 0 hour milled sample and a 12 hour milled sample is shown in Figure 3.2. The characteristic VO_2 and $CoFe_2O_4$ patterns are observed in both of these samples clearly. However the milled sample also shows formation of the iron oxide compound hematite, suggesting the milling process caused the cobalt ferrite compound to be split to some degree. This was observed for all milled samples. The milled sample's pattern shown in Figure 3.2 actually retains quite a bit of crystallinity, and yet if closely inspected we see that the signal is degraded and much noisier than the unmilled sample. Most of the milled samples' patterns did not even have this level of crystalline quality; although the peaks may be somewhat visible under close inspection, the only clear peak that remains for most milled samples is the VO_2 20-2/ $CoFe_2O_4$ 211

overlapping peak. It is well known that crystalline quality is decreased during the milling process, and it is clear that this is the case for our samples as well. This may be an explanation for why the MIT has been degraded as well, since crystalline quality is key for the structure change that happens during the transition.

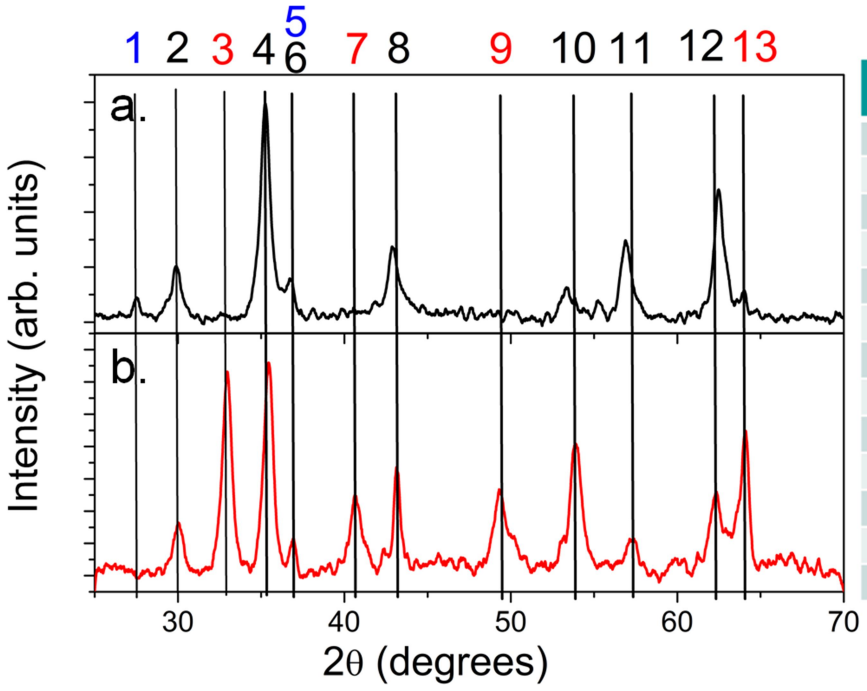

Peak No.	Crystal Plane	Compound
1	0,1,1	VO_2
2	2,2,0	$CoFe_2O_4$
3	1,0,4	Fe_2O_3
4	2,1,1	$CoFe_2O_4$
5	2,0,-2	VO_2
6	2,2,2	$CoFe_2O_4$
7	1,1,3	Fe_2O_3
8	4,0,0	$CoFe_2O_4$
9	0,2,4	Fe_2O_3
10	4,2,2	$CoFe_2O_4$
11	3,3,3/5,1,1	$CoFe_2O_4$
12	4,4,0	$CoFe_2O_4$
13	2,0,0	Fe_2O_3

Figure 3.2. XRD patterns for two different $CoFe_2O_4$-VO_2 mixtures. a. not milled sample b. 12 hour milled sample. Both mixtures were 80% $CoFe_2O_4$ and 20% VO_2. Associated peaks are labeled and identified in graph to the right of figure, where we see that there is a formation of hematite during the milling process.

After confirming that the VO_2 transition was still occurring, albeit degraded, and that our samples were still mixtures of the two desired compounds, albeit with some formation of other compounds, we explored whether there was any magnetic coupling between the compounds as was desired. As $CoFe_2O_4$ is a very hard magnet, up to 17,000 Oe fields needed to be applied to reach full saturation. Hysteresis loops were collected from -17,000 Oe to 17,000 at different temperatures across the VO_2 transition to see if there were any changes through the VO_2 SPT. A 60/40 12 hour milled sample's hysteresis loops at different temperatures through the VO_2

transition are shown in Figure 3.3. The inset shows what the hysteresis looks like for a normal single phase ferromagnet, in this case just one of our unmilled 60/40 ratio samples. Comparing this to the main figure, we see some very clear features that have occurred due to the milling process. Most clearly is the shape of the loops. Instead of a linear change in field as the magnetization flips, it is instead pinched in the center. This is indicative of the fact that there are two different ferromagnetic phases which are uncoupled. It is possible this is due to a secondary ferromagnetic compound formation, and since we know hematite is formed it seems likely this is the culprit as it is weakly ferromagnetic. However it is also possible inhomogeneity in the particle sizes could be responsible. It is important to note that this pinched effect was seen for all samples.

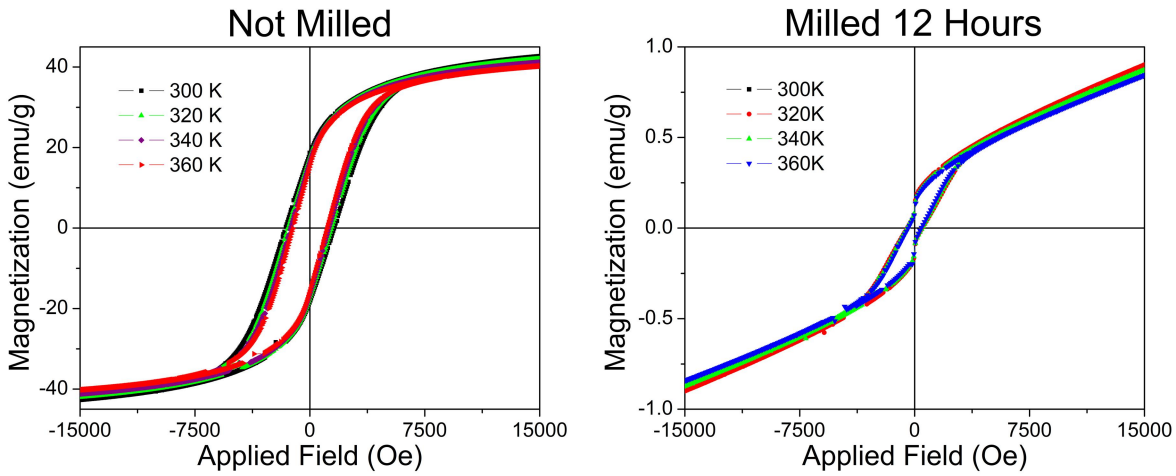

Figure 3.3. Hysteresis loops of 60% $CoFe_2O_4$-40% VO_2 12 hour milled sample at different temperature. Inset shows an unmilled sample. There is no clear difference as we travel across the VO_2 transition. Pinched hysteresis suggests that there is a formation of two different ferromagnetic phases in the sample, while the upward slope of the sample suggests the formation of a strongly paramagnetic component.

The next notable feature which has changed in the hysteresis of the sample in Figure 3.3 after milling is the net slope. In a normal single phase ferromagnet we expect the slope to be close to zero, however we see that the slope is positive for the sample shown in Figure 3.3. A

positive slope like this indicates that the substance is paramagnetic, meaning that a paramagnetic phase must have been formed as well. It is possible that another oxide of cobalt or iron is responsible for this. Only 2 samples had this effect, and they were both 60/40 samples, so it most likely has something to do with the interaction of the two compounds during the milling process, although exactly what is not clear. A less obvious to see change in the figure is the net magnetization. We see that the magnetization has been reduced considerably after the milling process. This could either suggest there is some large change in either the strain matrix of the mixture, or the anisotropy. We also found that the VSM was not reliable at obtaining accurate magnitudes of the powder samples' magnetizations (possibly due to the vibrations moving the particulates around even if they are packed densely), therefore this aspect of the data is not to be trusted as rigorously.

Once the hysteresis loops are collected, the coercivities are extracted to see if there is any trend as the sample passes through the VO_2 transition. As we discussed in Chapter 1, film samples have seen both large increases and decreases in coercivity across the transition temperature, and so any enhancement or suppression of the coercivity would be indicative of coupling between the VO_2 and $CoFe_2O_4$. Unfortunately we did not see any of these effects in the coercivity data. Both Figure 3.4 and Figure 3.5 show coercivity as a function of temperature through the VO_2 transition for different composite samples. Figure 3.4a shows what an unmilled samples coercivity looks like, and it follows the decreasing trend that is expected. Figure 3.5 is a good example of how most of the samples behaved, with no clear deviation from the negative slope trend of the unmilled sample. The only sample which had a response is shown in Figure 3.4b, the 6 hour milled 80/20 ratio sample. At the transition temperature there is a small 6% enhancement, suggesting some small coupling between the two compounds. Unfortunately this

could not be reproduced under other sample conditions. The lack of coupling could possibly be due to the degradation of the transition that was described above, and so it is likely a recrystallization procedure would have to be performed to achieve better results. Unfortunately this would involve heating the composite, and cobalt ferrite is not a very stable compound under heat treatment. How this technique is improved upon is thoroughly discussed in the next section.

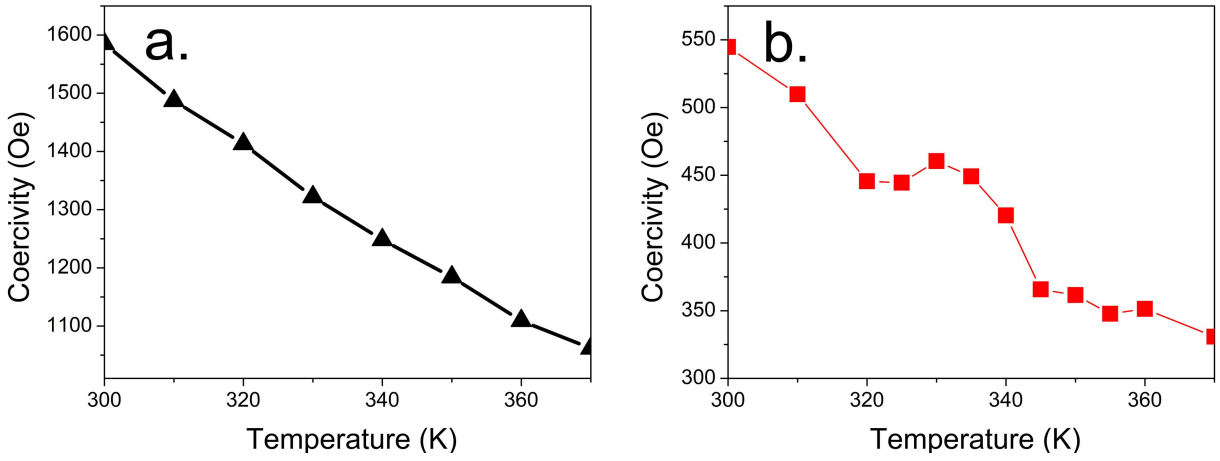

Figure 3.4. a. 0 hour milled sample. b. 6 hour milled sample. Both samples are from the 80/20 ratio sample set. As the samples go through the VO_2 transition we simply see the expected negative slope for the unmilled sample, while the milled sample shows possible coercivity enhancement in the transition region.

Before moving to the next section, there are still a few points to be made about the coercivity of these particular composites. It should be clear from Figure 3.4 and Figure 3.5 that the absolute coercivity is quite different depending on the sample. Unfortunately there was no clear trend from sample to sample to suggest why the coercivities changed so wildly depending on the fabrication parameters. Thus the only conclusion that can be made here is that they are highly dependent on other uncontrolled for parameters. Figure 3.5 also shows the coercivity for both heating and cooling through the transition twice, for 4 total cycles. After each cycle there is an irreversible change in the net coercivity in the form of a decrease. Lauzier et al.[108] had

previously seen this type of irreversibility in an analogous thin film system. In that study, AFM images proved that the irreversibility was due to cracks which form in the VO_2 layer as it passes through the transition. Based on this result it seems likely that in our case the VO2 particles are both breaking into smaller particles and shifting, causing a change in stress experienced by the ferromagnetic components in the system.

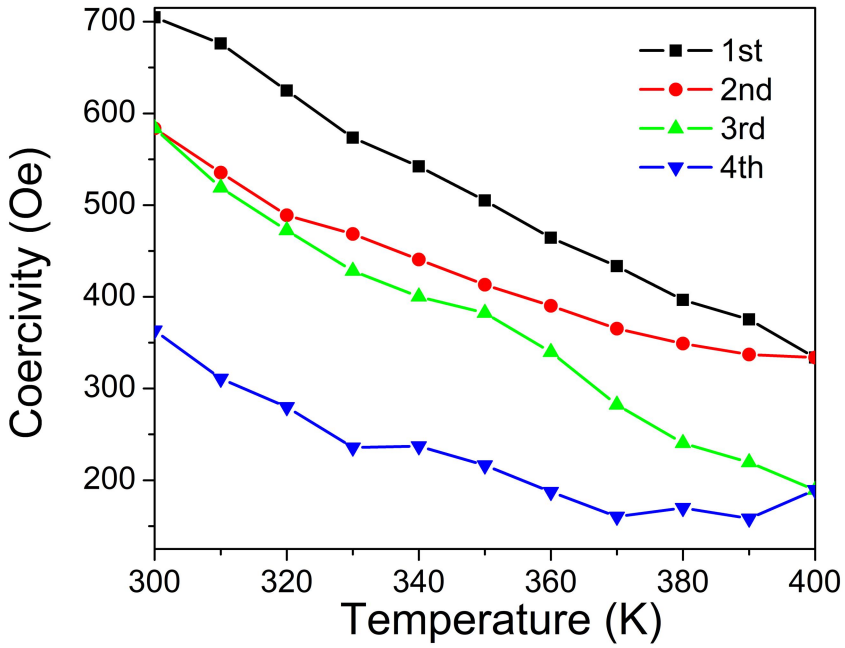

Figure 3.5. Coercivity across VO_2 transition over 4 heating cycles for 80/20 ratio 12 hour milled sample. Although the expected negative slope is seen each time, there is a net decrease in the coercivity each time the transition is passed through.

3.3 Sintering of Vanadium Oxide Composites as a Fabrication Technique for VO_2/Ni

After seeing limited results with the $VO_2/CoFe_2O_4$ composites using purely ball milling, it was decided that some crystallization process needed to be used to attain better results. As the $CoFe_2O_4$ had been problematic in the previously described process, we decided to opt for the simpler ferromagnet Ni for future processes. Urban et al.[109] had shown that by combining this

technique with a sintering process, V_2O_3/Ni composites, with the Ni magnetism coupled to the VO_2 transition, could be fabricated. In this process, there is an initial powder of VO_2 and NiO which is mixed and ball milled in the same way as described above. After the milling process, the powder is pressed into pellets under 200 MPa and sintered in a hydrogen environment at room pressure. The hydrogen gas will reduce the compounds in the powder in the following way:

$$NiO + H_2 \rightarrow Ni + H_2O$$

$$2VO_2 + H_2 \rightarrow V_2O_3 + H_2O$$

The reduction process quickly and effectively crystallizes both Ni and V_2O_3, and their compacted state allows for their grain boundaries to overlap. We did a detailed study on how the fabrication parameters can be optimized for this process to result in products which have high coupling between the two compounds, as well as the details of the crystallography and morphology which results from this process. The results and details of this study are given in the next section.

We tried to adapt this process for a final product which was a mixture of VO_2 (instead of V_2O_3) and Ni. First we started out using the same precursors of NiO and VO_2, following the same procedure outlined above. The mixture was 85% VO_2 and 15% NiO, and unless otherwise stated the vanadium oxide ratio to the nickel compound ratio was also kept as 85/15. VO_2 was the same commercial powder used in the previous section, and the 99% pure NiO (less than 100 nm particle size) used was also a commercial product. Sintering for the former process was typically over 2 hours long and above 600 °C, therefore we attempted a shorter reduction process at lower temperatures to try to reduce the NiO without reducing the VO_2. Unfortunately, lower temperatures(200-500 °C) either did not reduce the NiO, or reduced both compounds slowly but with the VO_2 reducing at a faster or similar rate, so that the resulting compound was a mixture of

Ni, NiO, VO_2, and V_2O_3. Using higher temperatures and lower times did not help, as it turns out that sintering above 600 °C under hydrogen reduces the compounds within 20 minutes, not allowing for enough control when considering the heating and cooling procedures already overtake this amount of time.

As it did not seem feasible to create the desired result using a precursor powder of NiO and VO_2, new attempts were made using different precursors. An attempt was made by replacing VO_2 with V_2O_5 powder instead, and following the same procedure otherwise. Anecdotally, if the same sintering times and temperatures are used that showed results for coupling V_2O_3 and Ni, the results are an almost identical product with similar coupling. However, trying to use shorter times to isolate VO_2 in the final powder, although allowing for the NiO to fully convert to Ni in this case, still resulted in mixtures of vanadium oxides, with all three main oxides (V_2O_5, VO_2 and V_2O_3) being identified along with several intermediary phases. From this we concluded that the reduction process under hydrogen did not allow for enough control to isolate oxides, and opted to try different heat treatment processes.

Instead of trying to reduce the materials for crystallization, heating in a vacuum of about 50 mTorr was used to attempt to crystalize the composites. Because we were no longer relying on chemical transformation, we used Ni powder in our starting mixture instead. The Ni used was either made by reducing the commercial NiO powder or using high purity (99.99%) commercial Ni (less than 40 nm particle size) powder. No difference was seen from using the two different precursors. The same milling and pressing procedures were followed for a VO_2/Ni mixture, and different sintering techniques were investigated. Temperatures from 800-1100 °C were used, as these were the ones that gave results for coupling in previous studies (and as will be seen in the next section there is a lower limit on the temperature for effective coupling) for the V_2O_3/Ni

composites. Sintering times from 2-24 hours were investigated. For shorter times the compounds regained their crystallinity and retained their chemical compositions, however no magnetic coupling was seen in these instances. Times over 6 hours started to reduce the VO_2 into intermediary phases, and above 18 hours they were also partially converted into V_2O_3. The mixed phase composites were tested for coupling, and still displayed no positive result. We began to realize the reduction itself may be more important in the coupling process between the two compounds, and so a starting powder of V_2O_5 and Ni was prepared. After vacuum sintering for 18 hours, the composite formed the crystalline structure displayed in Figure 3.6. We see that there is a mix of all three main oxidation states of vanadium oxide as well as both Ni and NiO. From this it can be concluded that, because Ni has a higher electronegativity than V, the Ni will become oxidized in the heat treatment as the vanadium compounds are being reduced. In other words, unless the vanadium oxide component is at its most stable lower oxidation state (V_2O_3), the vanadium oxide compound itself will end up oxidizing the Ni. Thus a controlled reduction process to VO_2 while retaining Ni is, at least using the heat treatment, impossible.

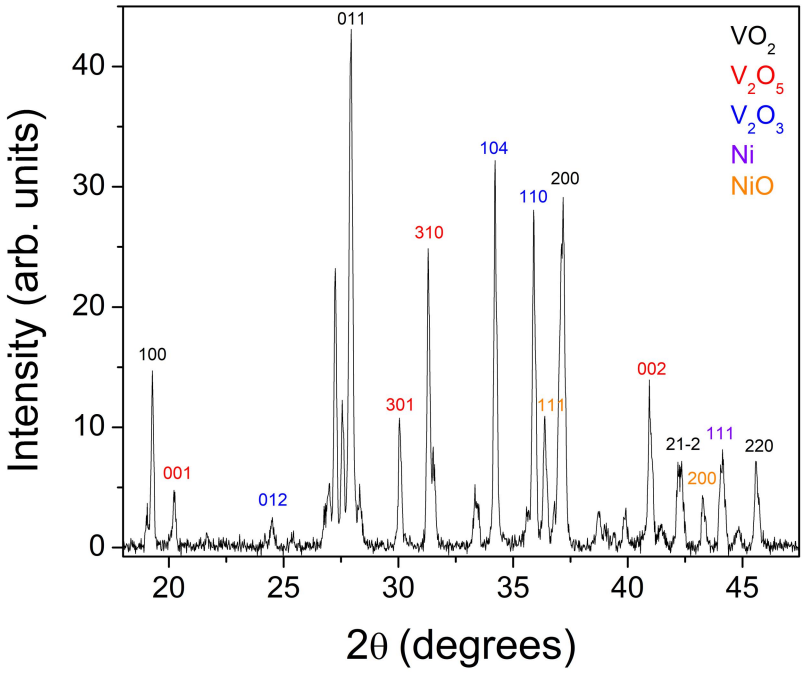

Figure 3.6. X-ray diffraction of an 18 hour sintered V_2O_5/Ni pellet. Sintered in vacuum. Crystal planes are labeled and phases color coded to right hand key. All three main oxidation phases of vanadium oxide are formed, and Ni is partially converted to NiO.

One more attempt was made, this time avoiding the heat treatment by instead reducing during the milling. Pure C was mixed in proportion to 50% V2O5 and 50% NiO powder. This reduction would work according to the following formulas:

$$2V_2O_5 + C \rightarrow 4VO_2 + CO_2$$

$$2NiO + C \rightarrow 2Ni + CO_2$$

Since we are able to measure out the precise amount of C for this reduction, it allows for a more controlled method. After milling the mixture, it was clear that it had reacted and reduced the compounds. However, once again the V_2O_5 reduced to a lower oxidation state than VO_2, forming V_2O_3 and only some Ni.

3.4 Fabrication of V_2O_3/Ni Composites and Optimization of Magnetic Coupling[1]

After the unsuccessful attempts fabricating coupled VO_2/Ni composites, we decided to focus efforts into the fabrication of V_2O_3/Ni composites, which had already shown promising results in previous studies. To determine optimal coupling and to see if previous studies' results could be reproduced, several different ranges of parameters were investigated in the fabrication of V_2O_3/Ni composites, and their properties measured. There were four main parameters that were varied: the ratio of VO_2 to NiO, the milling time, the sintering temperature, and the sintering time. Three different ratios were fabricated, 70% VO_2 and 30% NiO, 85% VO_2 and 15% NiO, and 94% VO_2 and 6% NiO. Milling times were varied from 2-24 hours. Sintering temperatures were varied from 600-1100 °C and sintering times varied from 5-18 hours. In truth, sintering temperatures and times beyond these were tested; however these cases were already discussed in depth in the previous section.

X-ray diffraction data was collected for each sample fabricated. Four characteristic samples' and the starting powder's x-ray patterns are plotted against each other in Figure 3.7, with peaks matched to their respective crystal planes. We see that the starting powder starts with only VO_2 and NiO peaks, as expected. We also see that all of the milled and sintered samples, regardless of fabrication conditions, show only V_2O_3 and Ni. It was true in general that all samples, regardless of the fabrication parameters stated above, showed a full conversion of both VO_2 to V_2O_3 and NiO to Ni. The main differences seen between the patterns were the broadness of the peaks. The samples with higher sintering temperatures generally had sharper peaks, which corresponds to larger crystallite sizes, thus indicating more crystal growth for these samples.

[1] Results from this section published in the work "Magnetic Properties of Hybrid V_2O_3/Ni Composites"[156].

After subtracting instrumental broadening, the peaks were fit with Gaussians to determine the position and broadening, and then the Scherrer equation discussed in Chapter 2 was used to estimate the crystallite sizes. The results of this analysis are shown in Table 3.1. Crystallite sizes of V_2O_3 show an increase for higher sintering temperatures as expected. For Ni, there was no clear correlation between the sintering temperature and crystallite size.

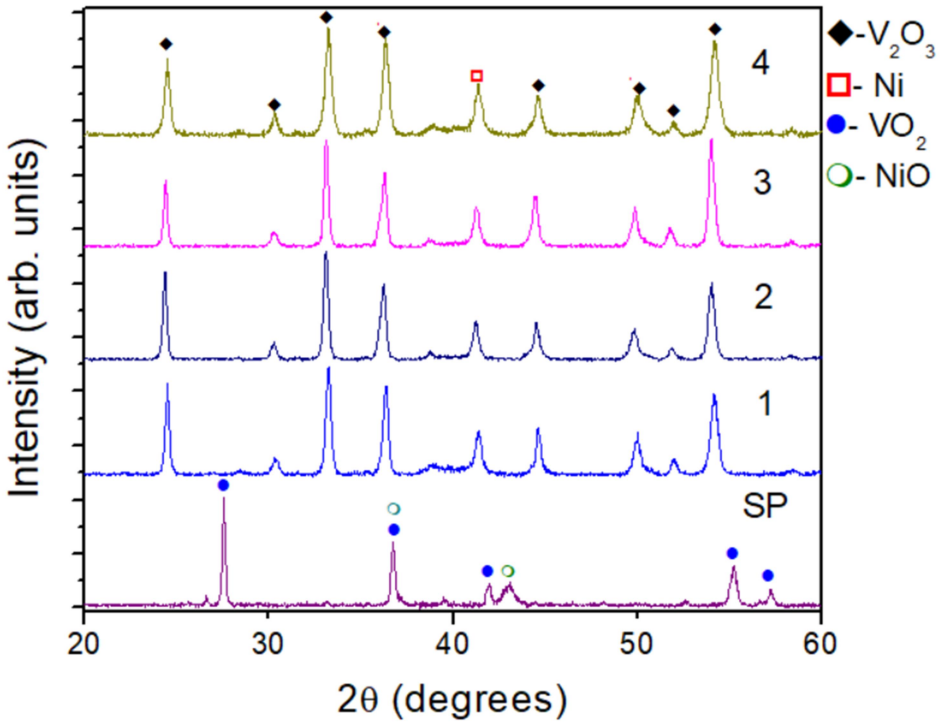

Figure 3.7. XRD pattern for 85%/15% starting powder (SP) as well as 4 different 85%/15% sintered powders. (1) 5 hours sintered at 800 °C, (2) 10 hours sintered at 800 °C, (3) 10 hours sintered at 900 °C, (4) 18 hours sintered at 600 °C. Compounds labeled based on right hand key.

Figure 3.8 shows the SEM data collected on three of the characteristic samples described shown above. All three samples have an apparent porous matrix of V_2O_3, with distinct structures formed. Particle size analysis was attempted, however from the lack of uniformity across scans of the same samples it was determined that TEM analysis would have to be done if this was

desired. We did not investigate this route further for the reasons described in Chapter 2. EDS data was also collected to determine the distribution of elements across the matrix of particulates. Data for the characteristic 900 °C sintered sample is shown in Figure 3.9, with the EDS mapping for V and Ni displayed side by side. All 3 samples that were investigated using EDS showed similar results for these mappings. We see that the V and Ni are disbursed equally across the sample region, suggesting little inhomogeneity in our samples.

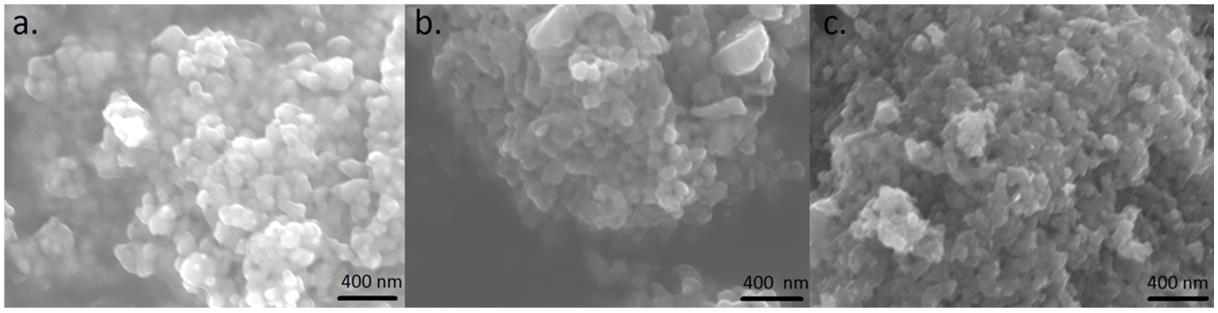

Figure 3.8. SEM micrographs of three different V_2O_3/Ni composites, all with ratios of 85/15. a. Sintered 10 hours at 900 °C. b. Sintered 5 hours at 800 °C. c. Sintered 18 hours at 600 °C

The previous studies[109] had shown formation of Ni rich clusters in a V_2O_3 matrix, which differs significantly from our results. This is most likely due to the fact that in that study milling times were much shorter (>2 hours), and therefore the compounds less uniformly distributed in the final product. The EDS data also showed several contaminants. The largest was due to Na uniformly dispersed across not just the sample region but the tape as well, as it is a common contaminant to be introduced in the SEM preparation process. The next most prevalent contaminants were large clusters of Zr mixed with the sample, showing that the milling media indeed became mixed with the sample material to some small degree. The lowest concentrated contaminants were also due to the milling media, Mg and Hf, which are the minor elements in the Zr ceramic.

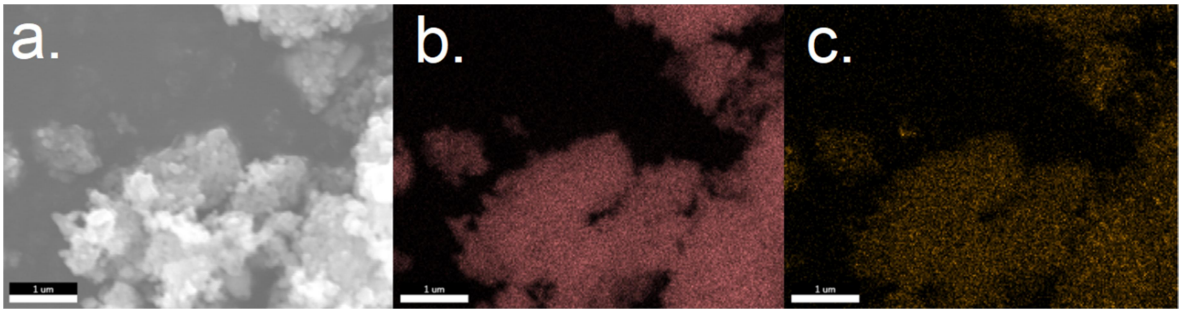

Figure 3.9. EDS mapping images showing two main components of a 12 hour milled 10 hour sinter at 900 °C 85/15 ratio composite. a. SEM image of the EDS scan region. b. EDS mapping of Vanadium. c. EDS mapping of Nickel

Magnetics data, both magnetization and hysteresis loops across the V_2O_3 transition, were collected for all samples that had full reduction. Large changes in coercivity and moderate changes in magnetization were seen in samples within certain fabrication parameter ranges, thus reproducing previous results in solids and films. Generally the samples with a composition ratio of 85/15 showed greatest changes, and so all data shown have this composition. In Figure 3.10 is displayed the magnetization vs. applied field graph for the 12 hour milled, 10 hour sintered at 900 °C sample. Saturation is reached by 2000 Oe, and there is no distortion in the shape of the hysteresis as seen with the $CoFe_2O_4$-based composites.

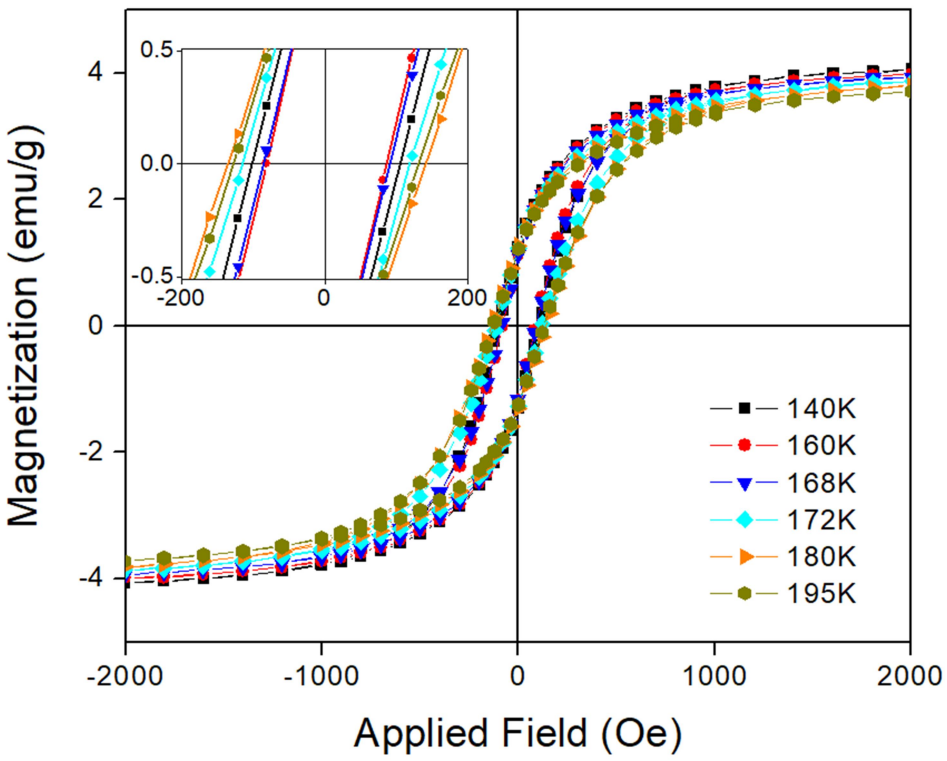

Figure 3.10. Hysteresis loops at selected temperatures for V_2O_3/Ni pellets (85%/15%) with 12-hour milling time. Sintered at 900 °C for 10 hours. Inset: Same plot from -200 Oe to 200 Oe.

The coercivity as a function of temperature for this sample is plotted in Figure 3.11a, where we see that the overall trend is decreasing, as expected, but that there is a sharp 53.8% increase at the V_2O_3 transition temperature. After this the general trend continues downward. This demonstrates the successful reproduction of previous results, although with a much greater magnitude change than was previously seen in composites. Figure 3.11b is a graph of the magnetization as a function of temperature, similarly showing a general downward trend, but in this case a sharp decrease of 4.8% is seen at the transition, after which the net downward trend is returned to. This sample showed some of the greatest changes out of the whole sample set. Comparing this to the 800 °C sintered for 10 hours sample, whose magnetics data is shown in

Figure 3.11c and Figure 3.11d, we see the somewhat smaller changes in coercivity and magnetization through the V_2O_3 transition, namely 30.2% and 2.6% respectively.

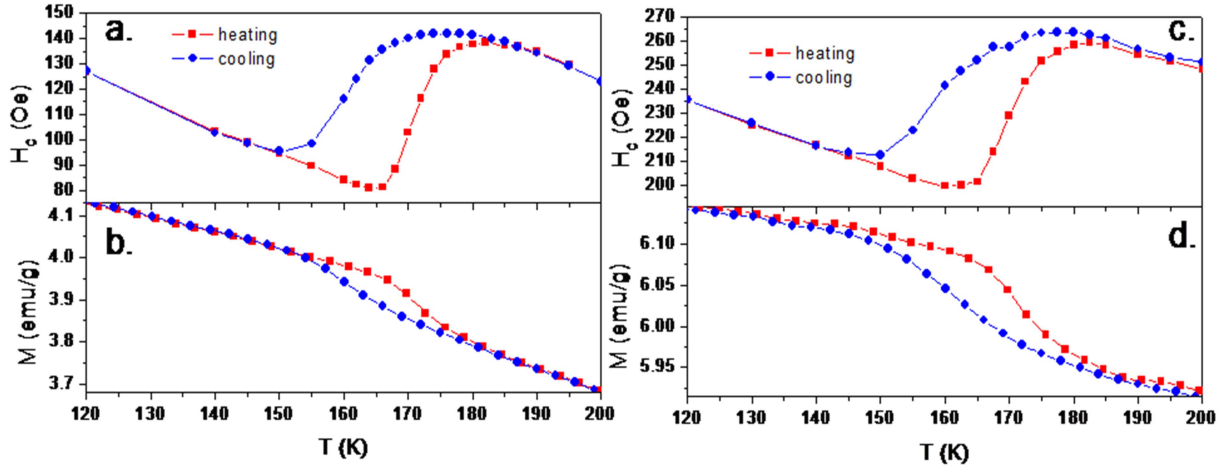

Figure 3.11. Magnetics data for two samples with large to moderate changes a. Coercivity vs. temperature of a sample milled 12 hours and sintered for 10 hours at 900 °C. b. Magnetization vs. temperature of same 900 °C sample at 1000 Oe. c. Coercivity vs. temperature of a sample milled 12 hours and sintered for 10 hours at 800 °C. d. Magnetization vs. temperature of same 800 °C sample at 1000 Oe.

Figure 3.12 shows a similar pair of samples which produced very different results in their magnetics data. In Figure 3.12a and Figure 3.12b we see the magnetics data for a 12 hour milled sample that was sintered for 5 hours at 800 °C. There is only an 11.3% change in coercivity for this sample, significantly smaller than the previous samples we've discussed. We also see that there is effectively no magnetization change at the transition for this sample, although there is a slight hysteresis indicating the SPT having some influence. In fact, all samples which had shorter sintering times had correspondingly smaller transitions. This suggests the time the sample spends being sintered has some direct correlation with the coupling, most likely either due to some minimum crystallite size required, or due to the time required for the particles to diffuse to the point required for effective coupling. Sintering temperatures had an even more drastic effect on the amount of coupling. Figure 3.12c and Figure 3.12d display the magnetics data for a sample

sintered at only 600 °C, and yet for a longer time of 18 hours. Unlike the other samples we've shown, this sample shows no deviations from the general trend whatsoever, suggesting no coupling between the V_2O_3 and Ni. All samples which were sintered at 600 °C showed no deviations from the general decreasing trend for both magnetization and coercivity data near the SPT. The change in coercivity for our main sample set is shown alongside fabrication parameters and calculated crystallite sizes in Table 3.1.

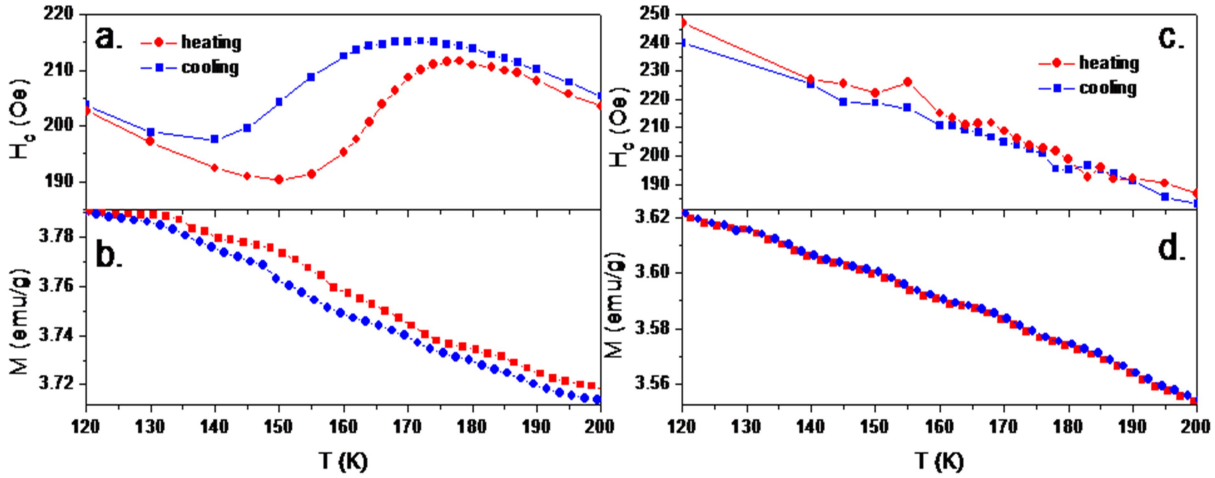

Figure 3.12. a. Coercivity vs. temperature of a sample milled 12 hours and sintered for 5 hours at 800 °C. b. Magnetization vs. temperature of same 800 °C sample at 1000 Oe. c. Coercivity vs. temperature of a sample milled 12 hours and sintered for 10 hours at 600 °C. d. Magnetization vs. temperature of same 600 °C sample at 1000 Oe.

Figure 3.13 shows a graph of the percent change in coercivity at the V_2O_3 transition as a function of the sintering temperature for all samples with the 85/15 composition ratio. The symbols represent the different milling/sintering time combinations in hours, as described by the left hand key. If we look at the trend in this graph, and study the data in the table carefully, there is no clear trend between the enhancement and the milling time, although comparing our results to the previous studies results might suggest that lower milling times than were investigated produce lower enhancement. Thus some minimum milling time below what we investigated is

most likely required for complete mixing. It is not clear from the graph what the effect of sintering time is, however it does seem that lower annealing times do have lower coercivity enhancements in general.

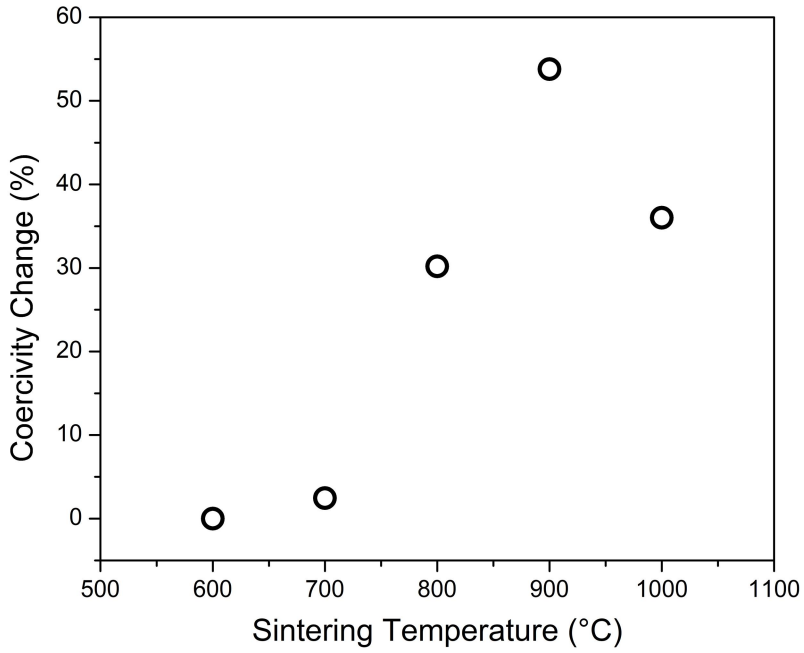

Figure 3.13. Percent coercivity change over the V_2O_3 transition shown as a function of temperature for samples fabricated with several changing parameters.

What is very clear from Figure 3.13 is that the sintering temperature is the main parameter which effects the magnitude of the coercivity enhancement. The region of 800-900 °C seems to show the largest coercivity enhancement for each sample set regardless of the other fabrication parameters. Remember that there is a direct correlation between V_2O_3 crystallite sizes and the sintering temperature, which arouses suspicions that maybe there is an ideal crystallite size for coercivity enhancement. However if the table is studied closely, we see that this is not necessarily the case, as similar crystallite sizes do not necessarily produce similar coercivity enhancements. Thus we can only conclude that the crystallite size is only part of the story.

Obviously there is some range of crystallite sizes that produce high coercivity enhancements, most likely due to some ideal area of interface between the grains, however the interplay between sintering time and temperature suggests that the diffusion of the compounds must also be an important factor to consider.

Table 3.1 A comparison of fabrication conditions and their resultant properties, including both crystallite sizes and magnitude of the magnetic transition.

NiO %	VO_2 %	Milling Time (h)	Sintering Time (h)	Sintering Temp. (°C)	V_2O_3 Crystallite Size (nm)	Ni Crystallite Size (nm)	Coercivity Transition
6	94	12	10	900	-	-	48.70%
6	94	12	10	800	105	23	13.80%
15	85	12	10	1000	244	95	36.02%
15	85	12	10	900	108	47	53.80%
15	85	12	10	800	85	44	30.20%
15	85	12	10	700	56	50	2.47%
15	85	12	10	600	52	31	-
15	85	12	5	900	78	63	28.80%
15	85	12	5	800	66	68	11.30%
15	85	12	5	600	43	41	-
15	85	12	18	900	136	62	40.90%
15	85	12	18	800	76	64	45%
15	85	12	18	600	42	36	-
15	85	6	10	900	199	40	22.80%
15	85	6	10	800	90	44	47.10%
15	85	6	10	600	55	23	-
15	85	3	10	900	143	80	24%
15	85	3	10	800	88	35	51.13%
15	85	24	10	900	230	48	56.30%
15	85	24	10	800	86	50	24.52%
30	70	12	10	900	106	94	47%
30	70	12	10	800	63	72	42.50%
30	70	12	10	600	34	44	-

Changes in the coercivity and magnetization can be explained as an effect of changing stress against Ni grains due to the V_2O_3 SPT. The changing crystal structure will cause a deformation of the shape and size of the V_2O_3 grains, which in turn will either release stress or

apply more stress depending on how the grain boundaries between the V_2O_3 and Ni are formed. Thus by the inverse magnetostrictive effect, which was discussed in Chapter 1, there will be a change in the magnetic properties as a result of this change in stress against the Ni. Considering the 3D nature of the composite, the changing stress is most likely compressive; since we see a decrease in the magnetization through the transition, our Ni must be experience a decrease in compressive stress. This makes sense, as there is a decrease in volume when the V_2O_3 goes from its low temperature to high temperature state. We can then assume that the coercivity enhancements are due to stress anisotropy, and the change in stress can be estimated by assuming that the change in coercivity is a stress anisotropy field.

Using equation 1.6, with the magnetostrictive coefficient of bulk nickel (-34×10^{-6}) as well as the saturation magnetization of bulk nickel (470 emu/cm^3) as our constants, we can then estimate the stress. Using the sample shown in Figure 3.12a, we see that the coercivity at 182 K is 138 Oe. Extrapolating the linear behavior before the transition, we would actually expect a coercivity of 61 Oe. Thus we can assume this 77 Oe difference between our extrapolated value and our measured value at 182 K is solely due to stress, and then use this value as our stress anisotropy field. Plugging all of these values into equation 1.6 results in a change of stress on the Ni particles of 35.5 MPa. Studies done on thin film V_2O_3/Ni bilayers have resulted in stresses as high as 55.3 MPa,[107] slightly larger than that calculated here.

Other groups have used a model known as the Klemens model[139] to estimate the stress that should be experienced in expanding and contracting composite systems. The details of this model are quite complicated, far beyond the scope of this thesis, and so only the basics will be discussed. The model assumes that stress at the boundaries of a two phase composite is purely

due to linear expansion. The change in the fractional linear dimension of an inclusion (γ) with temperature can thus be derived to be

$$\frac{\partial \gamma}{\partial T} = \frac{\alpha_2 - \alpha_1}{3} \qquad 3.1$$

where the α's are the linear expansion coefficients of the two materials. Bulk Ni's expansion coefficient is well known (1.3 x 10^{-5} K^{-1}), and we can determine the effective expansion coefficient of V_2O_3 across the transition by using the linear dimension change (0.5%) and the width of the transition (40K). This results in an expansion coefficient of 10^{-4} K^{-1}. Plugging these values in gives us the change of the linear dimension with temperature across the transition of 1.45 x 10^{-3} for an inclusion made of Ni or V_2O_3. The Klemens model also derives a relationship between this change, the stress, and the Young's modulus of the inclusion, approximating it to be the Young's modulus of the inclusion multiplied with the change in fractional linear dimension. This results in the formula

$$\sigma = Y_M \frac{\partial \gamma}{\partial T} \Delta T \qquad 3.2$$

We can use the value for change in fractional linear dimension for a Ni inclusion derived above, along with the width of the transition stated, and the Young's modulus of Ni to get a theoretical result for the stress Ni should experience in our system. The result is 290 MPa, and would result in a coercivity enhancement of 600 Oe, much larger than what we saw in our actual results. The resulting stress for the sample discussed in the previous paragraph is only experiencing 14.1% of this theoretical stress. This implies that there is some stress relaxation mechanism, likely at the grain boundaries, and so only some of the strain is transferred to the Ni.

3.5 Conclusions

We studied the effect of introducing a ferromagnetic material to a bulk system which undergoes a structural phase transition. Pure milling techniques showed very limited results in coupling the $CoFe_2O_4/VO_2$ system. The milling process reduced the crystallinity of the compounds and formed hematite. Hysteresis loops of the $CoFe_2O_4/VO_2$ composites were pinched, suggesting the hematite had an influence on the magnetics measurements and was not magnetically coupled to the $CoFe_2O_4$. Occasionally a strong paramagnetic phase was formed, although the composition of this phase remains unidentified. There were irreversible changes seen in the coercivity as a function of temperature after going through the VO_2 transition, with the net coercivity decreasing after each heating cycle, most likely due to the shifting of the particles in the composite. No compounds showed any appreciable coercivity enhancement or suppression, with the 6 hour milled 80/20 ratio sample having the most promising results and yet still within the range of error.

VO_2/Ni composites with coupled properties were not successfully fabricated. It was discovered that simply a recrystallization process did not cause coupling, possibly because more diffusion is required and chemical changes take place over the required time scales. All techniques that involved reduction led to either a fully reduced mixture of V_2O_3 and Ni, or a partially reduced mixture of vanadium oxides with a large amount of NiO still remaining.

The sintering process for V_2O_3/Ni composites fully reduces the VO_2 and NiO precursors if the sintering temperature is above 600 °C. Our process creates a homogenous mixture of V_2O_3 and Ni, at odds with the previous study's results. Coercivity enhancements up to 56% are seen, a large improvement from the previous study. The magnitude of the enhancement of the coercivity and the suppression of the magnetization is highly dependent on the fabrication parameters.

Sintering time needs to be at least 10 hours for better coupling, and the temperature region of 800-900 °C showed the largest enhancements, suggesting both grain size and diffusion are the important factors in this process. Any samples sintered at 600 °C showed no enhancement or suppression. Calculated stress from our results is only a fraction of the theoretical values, suggesting a stress relaxation mechanism is at play within the grain structure across the transition.

Chapter 4. Effects of W Doping in VO_2 on the Magnetic Properties of Sol-gel Synthesized VO_2/Ni Heterostructures[2]

4.1 Introduction to Fabrication Techniques and Goals

After having witnessed the results referenced in Chapter 1 and shown in Chapter 3, it should now be very clear why there is so much interest in V_2O_3/Ni and VO_2/Ni systems. Unfortunately, even though films have received a large amount of study, previous work has focused purely on sputtering techniques for fabricating bilayers, which are both expensive and more difficult to scale for industrial purposes than chemical techniques. Sol-gel techniques for the synthesis of VO_2 films have been one of the cornerstones in the development for cheaper VO_2 films that maintain a reasonable amount of crystalline quality. However, no other groups have tried to investigate how films fabricated with this technique compare to sputtered films in the fabrication of magnet hybrid heterostructures. Because the heterostructures are so sensitive to the interface between the two films (and thus the surface quality of the vanadium oxide layers), it is important to determine if films fabricated with this technique are still viable for the fabrication of heterostructures.

Another advantage of sol-gel techniques is the ability to introduce dopants in a controlled manner. In chapter 1 we discussed how doping VO_2 is a way to modify the transition temperatures with high precision, specifically with W. Doping with W using the sol-gel technique is not only well-studied, but there are many different routes of accomplishing it that are well-studied. By mixing the W and V metal complexes together into a well-mixed solution,

[2] Results from this chapter previously published in the work "Effects of W Doping in VO2 on the Magnetic Properties of VO2/Ni Heterostructures"[157].

the final product has very uniformly dispersed W atoms in the VO_2 structure. It is also possible to dope with W using sputtering techniques, and there are several different techniques to do this. Commonly there are three main ways to accomplish this: Small pieces of W can be placed on top of the V sputtering target, a target with the desired doping percent can be used, or W and V can be cosputtered during the fabrication of the film. A flaw in the first method is that the materials deplete very quickly, and so the sputtering chamber will have to be opened regularly to replace or modify the placement of the pieces (for different doping percentages), which leads to oxidation and lower quality films. Using a doped target is ideal for obtaining doped samples of a specific doping concentration, however if variable doping concentrations are desired this is not a suitable solution. Thus the most controlled method is to use co-sputtering. There are advantages and disadvantages to each method when considering the introduction of dopants, and so this needs to be investigated further before determining which technique is more suitable for different purposes.

There has also been no investigation into whether the VO_2/Ni heterostructures can be influenced by doping VO_2. The benefits of an effectively doped VO_2/Ni are obvious, for if W doping could also cause the magnetic effects, namely the large changes in coercivity and magnetization, to be shifted to lower temperatures, than the efficiency and versatility of devices that are able to be created can be drastically improved. The ability to lower the coercivity changes closer to room temperature would allow for magnetic recording devices to use less energy when they need to go through the transition for writing, and the lowering of the magnetization changes could make refrigeration applications actually feasible since they need to be close to room temperature. Determining the effect that different doping concentrations has on

the VO_2/Ni would also allow for the possibility of fabricating devices which have variable doping concentrations, and thus a large range of operating temperatures.

In the next section, we review our use refinement of the sol-gel synthesis techniques we used for the fabrication of VO_2 films, and ultimately their application in VO_2/Ni heterostructures. After this we will go over the results of using both sputtering and sol-gel synthesis as methods of fabricating W doped VO_2 films, and explain why the sol-gel technique was ultimately chosen for the fabrication of doped bilayers. We will then present the resulting magnetic measurements of successfully W doped VO_2/Ni heterostructures, and discuss the implications of these results.

4.2 Sol-gel Synthesis of VO_2 films and Use in Fabrication of VO_2/Ni Bilayers

The sol-gel technique that was ultimately used for our doping technique and the fabrication of W doped VO_2/Ni bilayers required much refinement to get both a good SPT and consistent results from film to film. This refinement required not only analyzing and adjusting several of the clear cut fabrication parameters, but also modifications of the procedure itself to increase efficiency and reproducibility. The initial fabrication procedure used three precursor compounds.[140] The first is the source of the vanadium atoms, vanadium oxytriisopropoxide ($OV(OCH(CH_3)_2)_3$), which is an organometallic compound used to form the sol. The second is ethanol, which forms the base of the solution. Last is acetic acid, which is the catalyst for driving the gel formation. There are two main processes which occur simultaneously, hydrolysis and polycondensation, which are represented by the following chemical reactions respectively:

$$OV(OCH(CH_3)_2)_3 + 3H_2O \rightarrow OV(OH)_3 + 3C_3H_8OH$$

$$2OV(OH)_3 \rightarrow V_2O_5 + 3H_2O$$

We see that an equivalent amount of water is formed as was needed, which allows this process to be completed without a correct molar ratio of water to be present. The hydrolysis part of this reaction forms a vanadium oxide alcohol complex, as well as isopropanol as a byproduct. The polycondensation is where the gel matrix of V_2O_5 is formed from the alcohol complex. Depending on the pH, several different things are possible at the polycondensation step, but our addition of acetic acid drives the reaction towards non-porous monolithic structure formation instead of high porosity particulate formation. We used commercial 98% liquid vanadium oxytriisopropoxide, commercial 99.9% pure ethanol, and commercial 98% pure acetic acid. The vanadium oxytriisopropoxide was kept at a fixed ratio to the solvent of approximately 15/70. Acetic acid was only approximately measured using a dropper, but also varied to determine the best amount of catalyst, starting out with 5 drops (~100 μL).

All gels were formed by mixing the precursor compounds using a magnetic stirring rod for a variable amount of time, from 6-48 hours. Once the stirring process was complete, the substrates were cut into 5 mm x 5 mm pieces and these pieces were cleaned by ultrasonication for 15 min in acetone and then 15 min in methanol. Substrates were affixed to the spin coater, and the gel was dropped onto substrates until covered. Spin coating speeds varied from 1000 rpm to 8000 rpm depending on the sample, and all samples used a coating time of 40 s. Once coated they were placed on a hot plate in air at 250 °C for 3 minutes, which allows for the film to densify and the alcohols to evaporate. This process is then repeated 2-3 more times to increase thickness of film. Profilometry measurements determined final film thicknesses of ~400 nm for samples with 4 coats, which corresponds to approximately 100 nm per coat. Once the coating process is completed, the films are placed on the hot plate at 410 °C in air, this time for 30 min to crystallize the films. Due to humidity and air temperature affecting this step of the process, an

insulating container was built to cover the samples on the hot plate during this step. The films are then placed in a tube furnace and annealed in vacuum (~1 Torr) from 450-530 °C, depending on the sample, for 2 hours with a ramp rate of 15 K/min for both heating and cooling. The purpose of this step is to reduce and further crystalize the film. The reduction process is as follows,

$$2V_2O_5 \rightarrow 4VO_2 + O_2$$

All samples are then stored in a light vacuum before measurements take place.

The technique above was able to produce VO_2 samples with very high quality MITs, like that of the sample shown in Figure 4.1a. Samples like this were accomplished by using a lower acidity, about 2-4 drops of acetic acid for the sol. Using more acetic acid tended to make darker films that had no transition in the VO_2 region, possibly because V_2O_3 was produced. This would not be surprising, as V_2O_3 formation is actually a competing polymerization process using this technique. However across the other variable fabrication parameters we explored using this technique, the main problem we encountered was reproducibility.

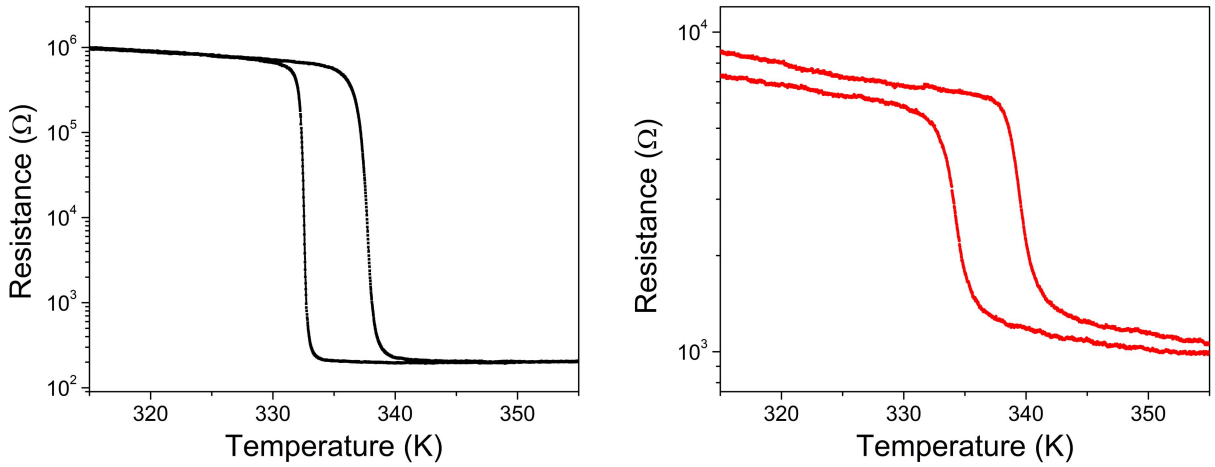

Figure 4.1. a. Sol-gel sample with good resulting film b. Sol-gel sample with bad resulting film. Both samples with same exact fabrication conditions, using the ethanol based technique with low acidity. Deposited on r-cut sapphire substrates, spun at 3000 rpm, and annealed at 530 °C.

Figure 4.1 demonstrates this clearly, showing two samples fabricated using the exact same parameters but at different times. In Figure 4.1a we see there is a sharp transition almost 3.5 orders in magnitude, whereas in Figure 4.1b we see a broader transition with less than a single order of magnitude change. It was also usually very clear visually that there was a difference in the final samples. When there was a good transition, the samples generally took on a darker brownish or orangish color, whereas films with bad transitions had a lighter yellow. One of these less than ideal films was analyzed using x-ray diffraction, the results of which are plotted in Figure 4.2. The presence of V_2O_5 suggests that the annealing process must not have fully converted the film to VO_2, so it is not surprising that the films have such a low quality transition. For comparison, the top plot in Figure 4.9 shows a higher quality film, and while the still contains some evidence of other vanadium oxide phases (however not V_2O_5) , the signal of these phases in comparison to the VO_2 phase is very low. Why this conversion did not take place for some films while it did for others is not clear. It is possible that the humidity in the air caused

the formation of undesirable phases of V_2O_5 which will not reduce given only the vacuum annealing technique. Although it was very possible to make high quality films, this lack of consistency did not suit our need to be able to compare samples with slight alteration in parameters. Therefore this specific technique ultimately needed to be changed or replaced. Although we believe that synthesizing the films in an environment with controlled humidity and temperature could resolve the issues described, lack of access to tools to allow for such control forced us to seek a different solution.

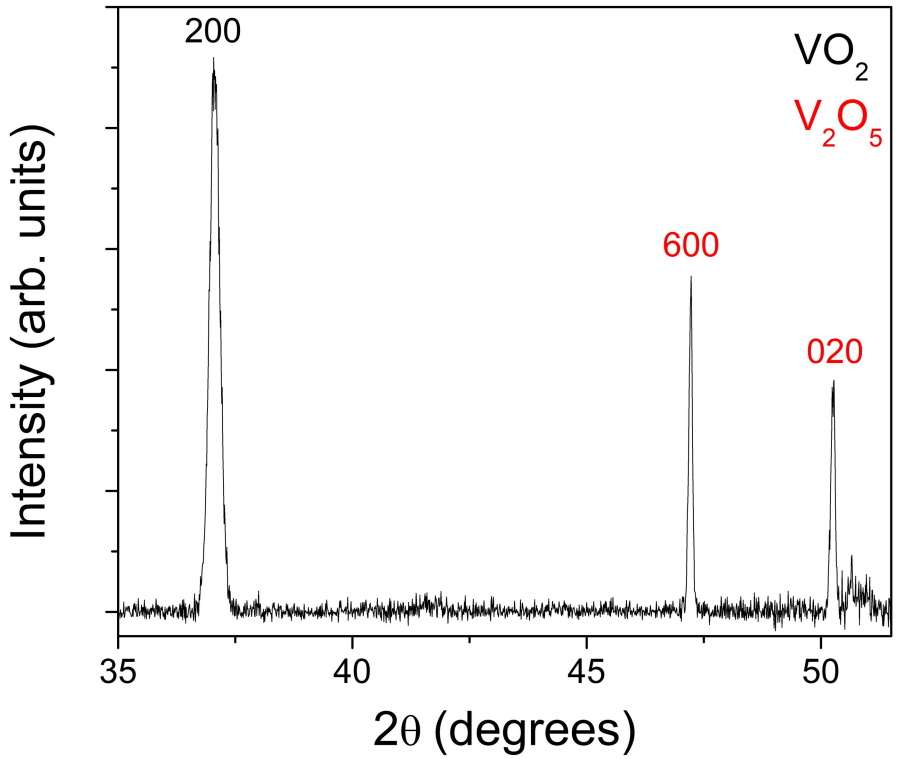

Figure 4.2. XRD of sol-gel sample with bad quality MIT. Both VO_2 and V_2O_5 are seen in the pattern.

A new technique was tried that was only slightly different. In this process the ethanol is replaced with isopropanol, and the amount of vanadium oxytriisopropoxide per solvent

significantly reduced. As it seemed like humidity was affecting the fabrication process, changing from ethanol to isopropanol had an added benefit, as ethanol is far more prone to absorbing water than isopropanol, especially high purity ethanol. This means that appreciable amounts of water could be introduced during both the gel formation and the drying processes, possibly altering how the hydrolysis process proceeds, changing the pH of the solution, or even catalyzing the formation of other compounds. For this process the acetic acid concentration was not varied, and was kept around 5 drops per 10 mL of isopropanol. This is consistent with the addition of acid in the previous solutions, so the vanadium compounds will be present in a similar pH environment, regardless of the reduced amount of vanadium oxytriisopropoxide. 0.283 mL of vanadium oxytriisopropoxide was added per each 10 mL of isopropoxide.

Using the new technique several parameter ranges were determined to be ideal. Letting the gel formation occur over a period of 18-30 hours produced the most ideal results. It was visually clear this was the case, even before testing resulting films. When first mixing the precursors, the solution takes a darker yellow color which can morph into a light blue color over the first 10-20 hours. However when the solution reaches the ideal stage for coating, it is almost completely transparent, a good indicator that the hydrolysis and polycondensation processes have formed the vanadium oxide gel matrix. However leaving the solution to stir for longer gradually increases the opacity, former a darker solution that has visually apparent black powder dispersed. This most likely indicates that vanadium oxide(s) between the 3 and 4 oxidation states have formed into nanoparticles. Once the stirring time was fixed at 24 hours the consistency between samples improved dramatically. However there was still some inconsistency between samples, approximately once every 3 or 4 samples a much lower quality film was produced. A slight modification of the procedure itself is what ultimately reduced the production of lower quality

films to a negligible quantity. This modification is simply removing the in air crystallization step of the process. Several other groups included this process with the reasoning that heating in air would better crystallize the V_2O_5 before it would be reduced to VO_2, which would ultimately lead to higher quality VO_2. However we found that when it was removed the films retained the crystalline quality which was previously seen, and lower quality films were never produced if the whole process was carried out carefully. This indicates that it is highly likely that the atmospheric conditions during the 30 min, 410 °C heating step was influencing the quality of the film. It is possible that if the atmospheric conditions could be more precisely controlled this pre-annealing heating step would improve the quality, however this was not investigated. One more parameter, which was not initially discussed, needed to be taken into account to reduce the production of low quality films. This is the shelf life of the precursor compounds. The isopropanol and acetic acid both have high stability, so their stability was not the issue. However the vanadium oxytriisopropoxide degrades very quickly, which we discovered once no good quality films were able to be produced using the same bottle. This was also apparent visually after time, as there was a large sedimentation of black powder that would not dissolve, once again suggesting there was a degradation to one of the vanadium oxides in the 3-4 oxidation state range. It was visually clear that this degradation started to take place within 45 days of the precursor compounds introduction to air, with the precursor becoming completely unusable after 60 days. The degradation could most likely be prevented if the bottle was stored in a controlled atmosphere, however this was not available to us.

Several other parameters were varied to determine the effect they had on the resulting films. Annealing temperature was varied between 450 °C and 530 °C. Figure 4.3 shows a resistance as a function of temperature plot through the VO_2 MIT for two different annealing

temperatures. We see that the higher annealing temperature has a slightly broader transition with a smaller hysteresis. This was generally true with higher temperatures, and so to optimize the sharpness we chose to use 450 °C as our annealing temperature for the other samples. Different spin coating speeds were also tested to see how they had an effect on the morphology of the films. This can be very important in the fabrication of bilayers, as previous studies[108] have shown that larger grain sizes tend to produce larger transitions. It is also well known that magnetic thin films with surface and interface roughnesses of a higher magnitude will in turn have higher coercivities. Figure 4.4 shows the different morphologies for films spin coated at 1500, 3000, and 8000 rpm. The main trend seen here is the decrease in roughness of the films with increased rpm. However the grain sizes are comparable between the 3 films, with the 8000 rpm sample showing only slightly larger grains. We also see that the 8000 rpm film has a more elongated and elliptical grain shape compared to the other samples. There is also directionality to this elongation, suggesting the grains may grow elongated perpendicular to the rotational axis due to the gel being spun at such high speeds. 3000 rpm was used for the rest of the samples, although this selection was somewhat arbitrary considering the lack of variation in grain size.

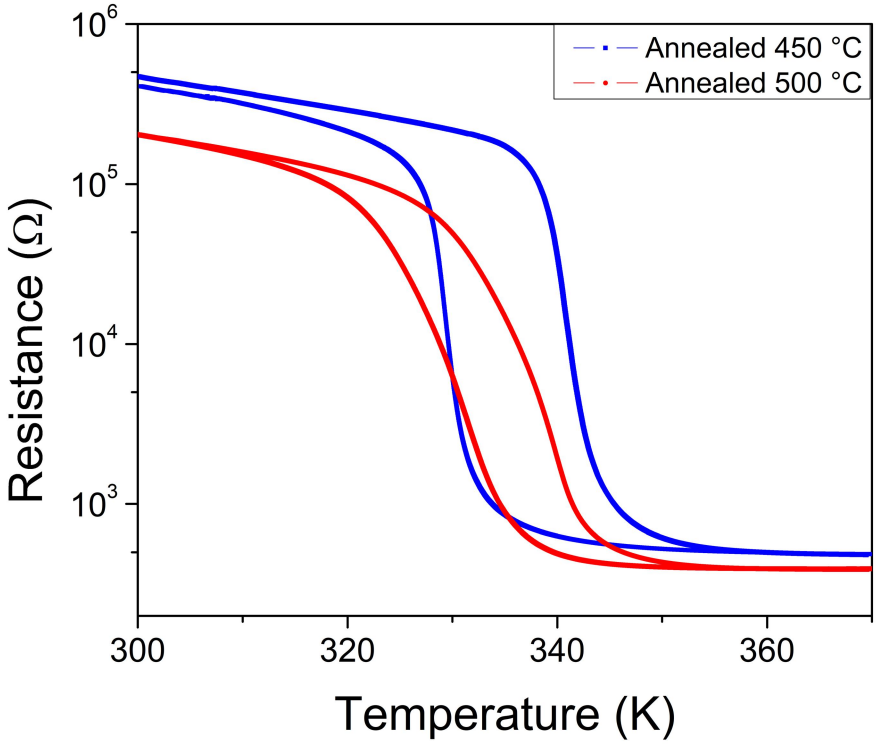

Figure 4.3. R vs. T for two different annealing temperatures. Red graph was annealed at 500 °C while blue was 450 °C.

The effects of different substrates were investigated as well. This has already been well studied, and was done to see if we could reproduce the results using our fabrication technique, to allow for more versatility when fabricating later samples. R-cut (-1012) sapphire (Al_2O_3) was the main substrate used for most samples, but c-cut (0001), m-cut (10-10), and a-cut (11-20) sapphire substrates were also used for comparison. There was not a noticeable difference in the quality of films between the three different cuts of sapphire, and there were only slight changes in the sharpness of the transition. Z-cut (0001) quartz (SiO_2) was also investigated as a substrate, mainly due to the fact that it is easier to etch than sapphire. Unfortunately the lattice mismatch is not ideal, so it is well known that it produces lower quality films than ideal substrates like sapphire or TiO_2. Figure 4.5 shows a comparison between the electrical transport properties of

sol-gel samples fabricated simultaneously on r-cut and quartz substrates. We see that while the r-cut sample has a 2.5 order transition, the quartz only has a 1 order transition. The quartz sample is also slightly broader and has a larger hysteresis.

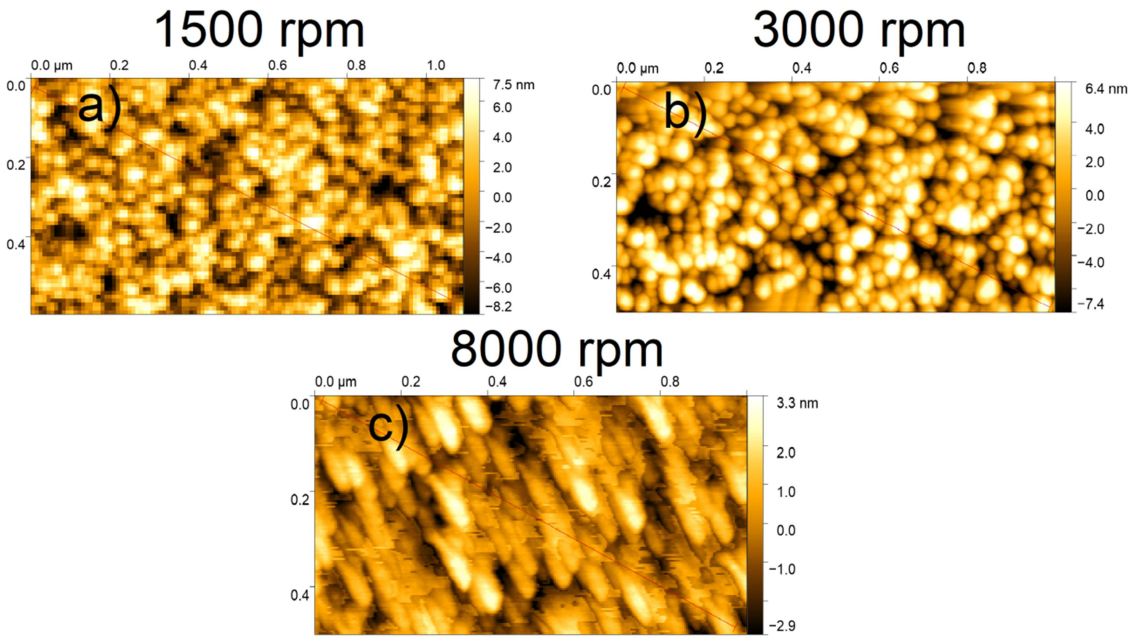

Figure 4.4. a. Sol-gel VO_2 film spin coated at 1500 rpm. b. Sol-gel VO_2 film spin coated at 3000 rpm. c. Sol-gel VO_2 film spin coated at 8000 rpm. The 8000 rpm sample had an rms roughness of 1.68 nm, the 3000 rpm had roughness of 3.15 nm, and the 1500 rpm sample a roughness of 3.63 rpm. All other sample fabrication parameters are identical.

From this point in the chapter, all of the data for sol-gel samples that will be presented were fabricated using the isopropanol based technique, mixed for 24 hours, spun at 3000 rpm onto r-cut substrates, and annealed at 450 °C. X-ray diffraction data for a bare unaltered film fabricated in this manner is shown in the top graph of Figure 4.9. The main peaks in this graph are from the r-cut substrate and monoclinic VO_2, however there are smaller peaks which remain unidentified in the graph. This is due to the fact that they can correspond to intermediary oxide phases of vanadium that overlap with one another, making it impossible to distinguish which specific intermediary phase or phases they correspond to. Thus this technique does still produce

some impurities, however the quality of the transition is still suitable for the fabrication of heterostructures.

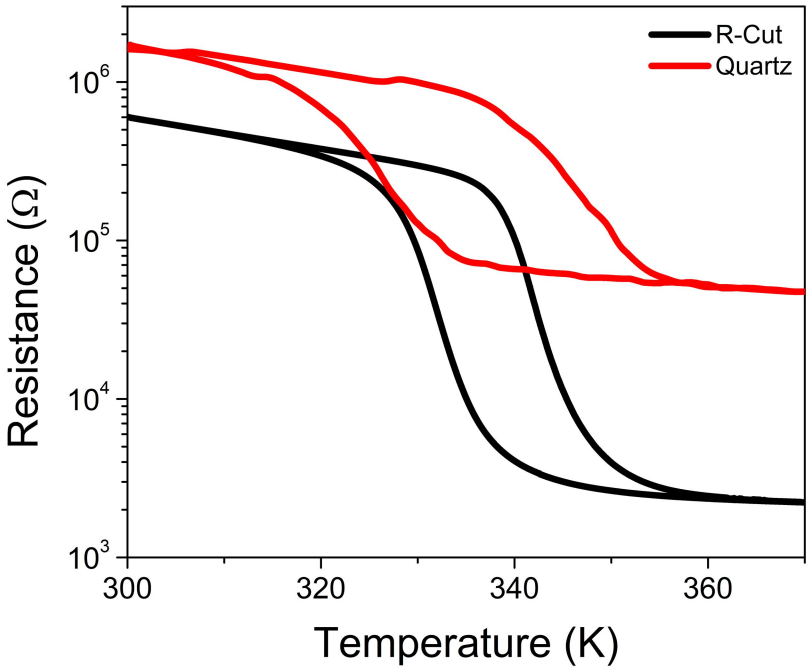

Figure 4.5. Electrical transport properties through the VO_2 transition for sol-gel samples deposited on r-cut and quartz substrates, compared. Both samples fabricated simultaneously.

The deposition of Ni on top of VO_2 fabricated using the sol-gel synthesis does not differ very much from the pure sputtering techniques which have been used previously.[108] The main difference is the inability to deposit Ni on top of VO_2 in situ. All VO_2 films must be taken into air and transferred to the sputtering system. The details behind our sputtering procedure in general are described in the next section. Most films were raised to 200 °C, well above the VO_2 transition temperature, before being deposited on. This corresponds to the Ni being deposited onto rutile VO_2. The Ni was sputtered from a 99.95% pure Ni target, using a DC power supply at 50 W. 15 nm of Ni was deposited on top of the VO_2 films for each sample. One exception is was made for the sputtering temperature, where a film was cut in half and one piece had Ni deposited

onto the rutile state, whereas the other was left at room temperature to have Ni sputtered onto the monoclinic VO_2. All samples were also coated with a 5 nm capping layer of W, using the DC gun at 50 W at room temperature, so as to prevent oxidation of the Ni surface. As Ni is the only ferromagnet in this system, the magnetics measurements primarily reflect this layer. Samples are all fully saturated at an applied field of 1000 Oe. Hysteresis loops were collected for these samples at different temperatures through the MIT, and the coercivity extracted, just as was done for the composite samples in Chapter 3. Results are shown in Figure 4.6, where we see the signal very similar to that of sputtered films. Rutile deposited films show consistent sharp decreases of up to 65% through the MIT, approaching that seen in films.[108]

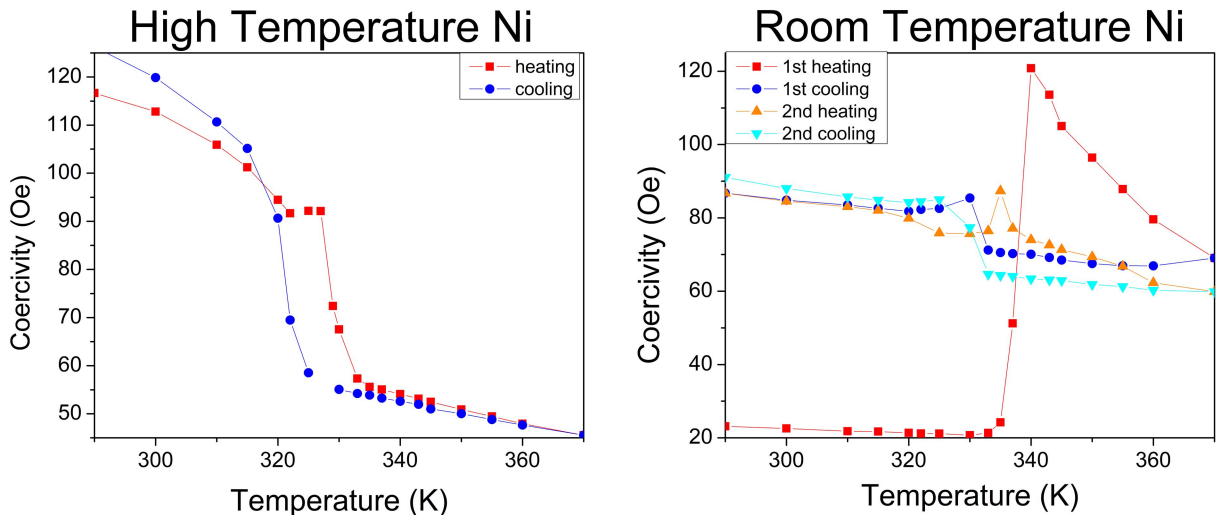

Figure 4.6. Coercivity changes across the VO_2 transition for VO_2/Ni bilayers with Ni deposited at two different temperatures. VO_2 layers were from same film, which was cut in half before Ni deposition. Room temperature deposited Ni plot shows two heating/cooling cycles to demonstrate the large irreversible change that is seen. High temperature deposited Ni was deposited at 200 °C.

For the monoclinic deposited film, we see that during the first heating cycle there is a large 142% increase, however after this the cooling and heating cycles show almost no change. This is actually also a reproduction of results previously seen in sputtered films, and is studied extensively in Lauzier et al.[106] The basic explanation is that this irreversibility is caused by

cracks and fissures forming in the Ni layer during the first transition. Rutile deposited films already have to go through this transition before they can be measured, which is why we do not see an analogous effect for these films. It is also clear that the reproducible coercivity changes at the transition after the films have already been cracked are much larger for rutile deposited films, so we will focus on these for the rest of the chapter. These changes are due to the inverse magnetostrictive effect and stress anisotropy, which we have discussed extensively in both Chapters 1 and 3. Just like for the V_2O_3/Ni composite in Chapter 3, we can estimate the stress by assuming the coercivity changes are due to the anisotropy field. The volume change across the VO_2 SPT is probably not the main cause of the stress transfer change between the layers, and instead it is a change in the tensile stress between the layers. Extrapolating the trend from 340 K to 320 K, we see that the coercivity would be 65 Oe, but our measurement shows that it is actually 105 Oe. The difference is thus 40 Oe, and we can plug this into equation 1.6, using the same constants we had used for the composite to determine the stress to be 18 MPa. Sputtered films with higher quality have been calculated to have stress transfers from 22-59 MPa;[105,108] so although our sol-gel synthesized bilayers, expectedly, do not have as high of structural coupling between layers, they do approach this level of coupling.

4.3 W Doping Using Both Sol-gel and Sputtering Techniques

As we discussed in section 4.1, there are several different methods of doping films using a sputtering technique. We wished to analyze films with different doping concentrations, so this ruled out the possibility of using a doped target. Although placing the dopant on the target is a good option for being able to adjust the doping concentration, unfortunately fabricating VO_2 films in a sputtering system requires a large amount of control over oxygen concentrations. Using this doping technique would require opening the main chamber of the sputtering system

each time a new doping concentration is desired, and the amount of time it takes to gain control of the oxygen concentration inside the chamber after it has been opened makes this technique infeasible for comparing samples. Thus the only viable option for our requirements is co-sputtering of W during the sputtering procedure.

Before we could make doped films we first had to tune the sputtering process to create high quality pure VO_2 films. R-cut 5 mm x 5 mm substrates were used for all samples. Before they were placed in the sputtering system they were cleaned using ultrasonication in an acetone bath for 15 minutes, and then a methanol bath for 15 min. The base pressure of the system was below 2.3 x 10^{-7} Torr for all sputtered films. Once in the chamber, the films are brought to the sputtering temperature in steps of 25 °C per minute to make sure the substrate does not crack or warp. The sputtering temperature itself can have a range of about 475-675 °C for good quality films, but the oxygen concentration needs to be tuned for different temperatures. We started out with a sputtering temperature of 575 °C at the beginning of our tuning process, but ultimately dropped to 525 °C. Once the substrates are at the sputtering temperature a presputtering process is required to help form a stable plasma and to clean the target. First argon is added to the system at a rate of 31 sccm, and then the pressure is brought up to 30 mTorr. The RF power supply, which is hooked up to the V gun, is brought to a power of 50 W to spark the plasma formation. This starts the sputtering process on the V target, but because there is a mechanical shutter on the gun it only sputters internally and not in the rest of the chamber. A pure 99.95% V target is used in this gun. The presputtering is allowed to continue for 10 min to make sure the plasma is stable, and also serves to clean off any oxides that may have formed on the surface of the target. Next, the power of the RF gun is brought up to the sputtering power of 200 W. The rate at which oxygen is introduced to the system is one of the most important parameters in determining the

quality of the film, so it is the main parameter which is varied, with films of slightly different amounts of oxygen tested and compared. The range of oxygen which was tested was from 2.73-3.05 sccm, but 2.77 sccm ultimately resulted in the best films. Once the oxygen is introduced, the target is allowed to presputter for another 5 minutes so that it's clear the plasma is stable. The shutter is then opened and the deposition of the film begins. All films are deposited to approximately 100 nm, corresponding to about 40 minutes at this pressure and power. Once films are of the desired thickness the sputtering is stopped, the temperature brought back to room temperature at the same rate, and the gas flow and pressure brought to base values. The main technique we used to determine the film quality was by testing the electrical transport properties of the MIT. Higher quality films will have a change in resistance at the transition of at least 4 orders of magnitude. An example of one of the well-tuned films is shown in Figure 4.7.

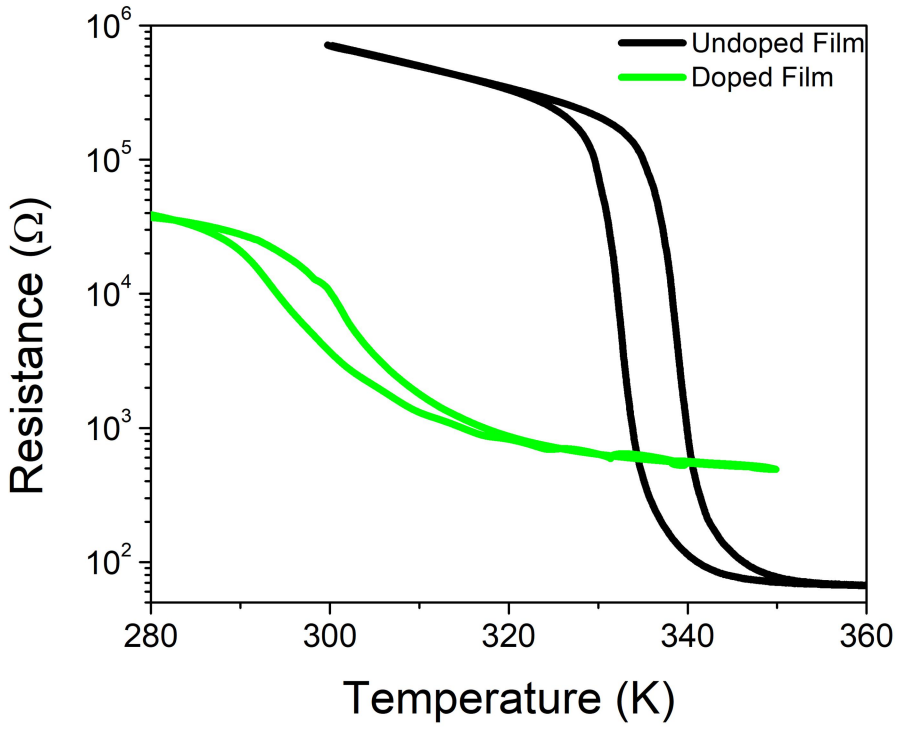

Figure 4.7. Resistance as a function temperature for an optimized sputtered film and a W doped sputtered film. Doping concentration is approximately 2.3%.

Introducing dopants into the film requires this same process, except with the W gun now supplied DC power to presputter and sputter the W target alongside the V target during the relevant steps. The W target used was also a 99.95% pure target. For presputtering, the W gun was held at 50 W, but before the deposition started the power had to be brought much lower, so as to reach the dopant range desired (0.1-2%). Unfortunately we ran into several difficulties at this point. The plasma is only very stable to about 25 W for W, and when this power was attempted it was immediately clear when films were removed too much tungsten had been added, as the film was completely metallic even at low temperatures. We estimate that the tungsten target at 25W was doping the system as high as 10%. Lowering the power further caused a different problem to arise. Below 15 W the plasma starts to become extremely unstable,

and will flicker or go out very easily. However 15 W produced films that were still far too doped, with transitions that didn't start until 270 K and were extremely small. This seems to correspond to about a 3% dopant concentration in the film. Below 11 W the plasma goes out completely immediately, setting a hard limit on the minimum amount of dopants we can introduce. 11 W was attempted, but unfortunately the plasma disappears very soon during the deposition, not allowing for a film with the desired thickness to be fabricated. The lowest power that was able to produce 100 nm films was 12 W, and even this was difficult due to the plasma often disappearing. A resistance versus temperature measurement of one of these films is shown in comparison to the undoped film in Figure 4.7, demonstrating the shift in temperature of the MIT, as well as the corresponding reduction in magnitude. The shift corresponds to approximately 2.3 % doping in the sample. Unfortunately, with over 2% doping as our lower limit, the sputtering technique simply did not allow enough control over the addition of dopants.

The sol-gel technique was also investigated to see if it was a better candidate for producing doped films. The same procedure using isopropanol that was described in the previous section was used with one simple modification, the addition of a tungsten based organometallic compound during the initial mixing. We used a commercially bought compound called tungsten (VI) isopropoxide, which was dispersed in isopropanol. This is in a sense the W analog of vanadium oxytriisopropoxide, and undergoes a similar set of reactions:

$$W(O_2CH(CH_3)_5)_3 + 3H_2O \rightarrow W(OH)_3 + 6C_3H_8OH + 3H^+$$

$$2W(OH)_3 \rightarrow WO_3 + 3H_2O$$

We see that the hydrolysis reaction produces a W alcohol complex and isopropanol, as before, but also lowers the pH of the solution. The polycondensation process forms the same amount of

water as the hydrolysis required, just as with the vanadium counterparts. The final tungsten product is tungsten (VI) oxide, which will end up embedding in the V_2O_5 matrix. As the reduction process for WO_3 tends to lead to WO_2, the main two oxide phases in the final film, VO_2 and WO_2, will have the same ratio to oxygen, which should more effectively dope the VO_2 films while minimizing extra unwanted distortions to the crystal lattice. The tungsten isopropoxide is able to be mixed at a very precise ratio to the vanadium oxytriisopropoxide, allowing for far more control over the doping concentration than we had for the sputtering process.

We fabricated doped sol-gel films ranging from 0.1-3% doping concentrations. The electrical transport properties across the VO_2 MIT for three characteristic films are shown in Figure 4.8. These are 0%, 1%, and 2% doped films, and used to demonstrate the differences between normal films and a progression of doping. We see that the results seen in many previous studies are reproduced, with both a shift in temperature and reduction in the magnitude of the MIT for doped samples. The temperature is shifted from 335 K for the undoped to 302 K for the 2% doped sample, and the transition decreased from 2.5 orders of magnitude for the undoped sample to 0.7 orders for the 2% doped sample. There is no clear trend to be seen in the hysteresis with increased doping concentration, however there is a broadening of the transition from 22.7 K for undoped to 26.7 K for 2% doped. These trends are reproducible and consistent across the full range of doping tested.

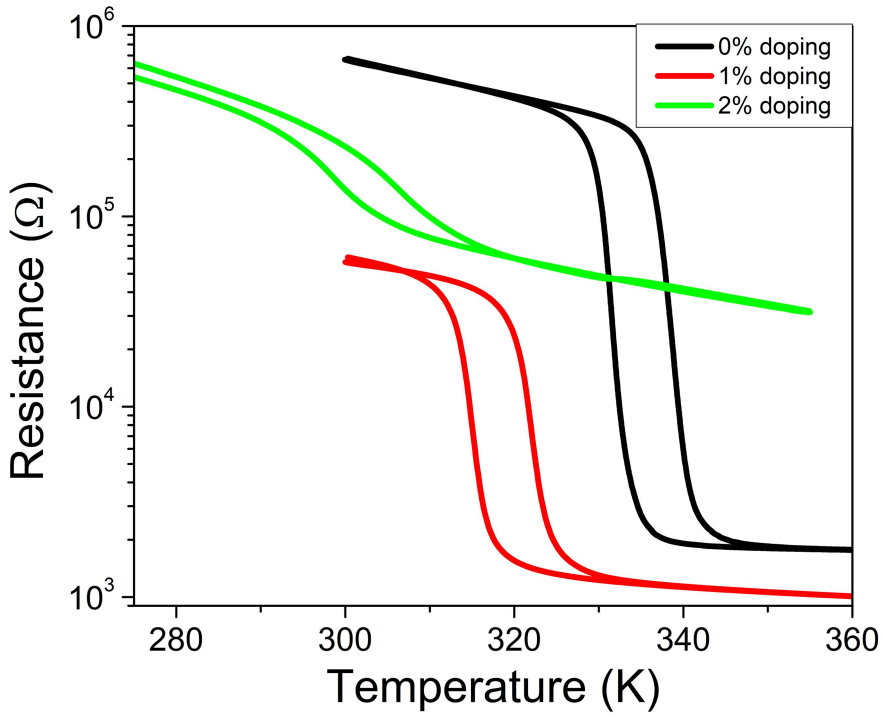

Figure 4.8. Resistance as a function of temperature through the VO_2 transition for several W doped sol-gel VO_2 films. Doping concentration ranges from 0-2%.

For samples with doping concentration lower than 1.5%, the insulating state resistance shows a trend of higher resistances with lower doping concentrations. This is not surprising, as the addition of W increases the number of carriers in the system. What is surprising, however, is that for higher doping concentrations, larger than 1.5%, there was no reproducibility or clear trend for the insulating state resistance, even for samples with identical doping concentration. This suggests that there must be some more complex mechanism for higher doping concentrations. As an example demonstrating this break in trend, we compared two 2% doped films fabricated, one which had an insulating state resistance on the order of 5.4 (the one in Figure 4.8), while the other was on the order of 4.2. However the transition temperature of these

films were both 302 K, and they had barely distinguishable widths and magnitudes. 1.5%, 1.75%, and 3% doped samples behaved in the same manner.

XRD patterns were collected for the three doping concentrations we just discussed, and are displayed in Figure 4.9. All data were collected at room temperature. As was discussed, the undoped sol-gel sample only clearly shows monoclinic VO_2, with some phase impurity that remains unidentified for the reasons previously explained. Doped samples show evidence of both monoclinic and rutile phase VO_2, along with the compound V_2WO_6. The doped samples also showed other unidentified phases which couldn't be specifically identified due to overlapping peaks.

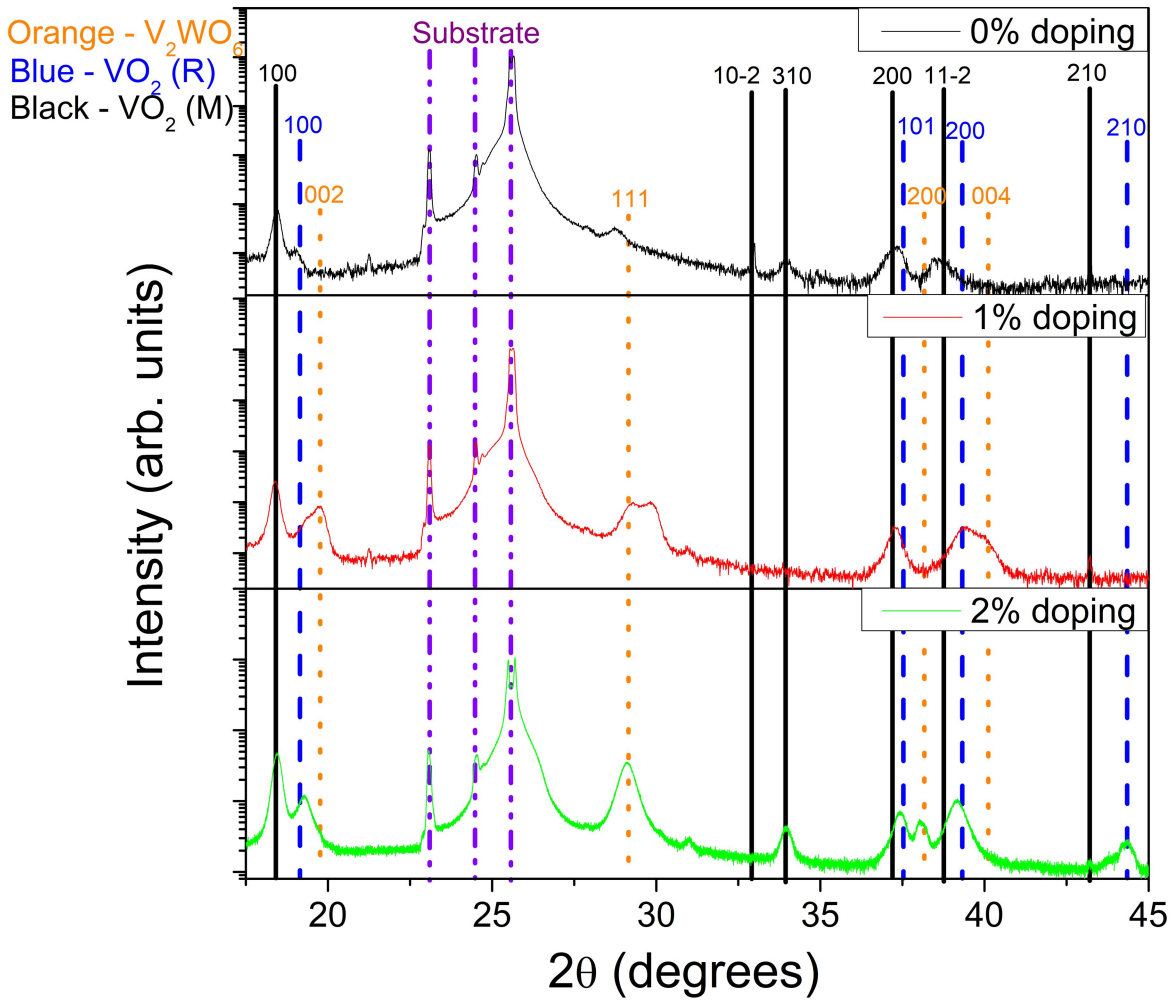

Figure 4.9. X-ray diffraction patterns for VO_2 films with 3 different doping concentrations. Both monoclinic and rutile peaks are identified, along with the compound V_2WO_6. Other phase impurities remain unlabeled due to the inability to isolate.

To further confirm that it was the rutile phase which was stabilizing in the doped films, we performed a more in depth XRD analysis of the VO2 peak near 2θ = 37°. The peak in this region of the pattern can corresponds to both the monoclinic phase 200 plane and the rutile phase 011 plane, with the angular distance separating them only about 0.2°. Other studies[105,141] have used these peaks to demonstrate the shift from the monoclinic phase to the rutile phase by

showing how the central maximum of the peak shifts to higher degrees when increasing the temperature through the SPT. Instead, for our analysis, we fit a Gaussian to the peak in this area for the three different doping concentrations shown in Figure 4.9. Figure 4.10 shows the results of our Gaussian fits, demonstrating a shift to higher angles with increased doping. This confirms the assumption that the increased doping stabilizes the high temperature rutile phase at room temperature.

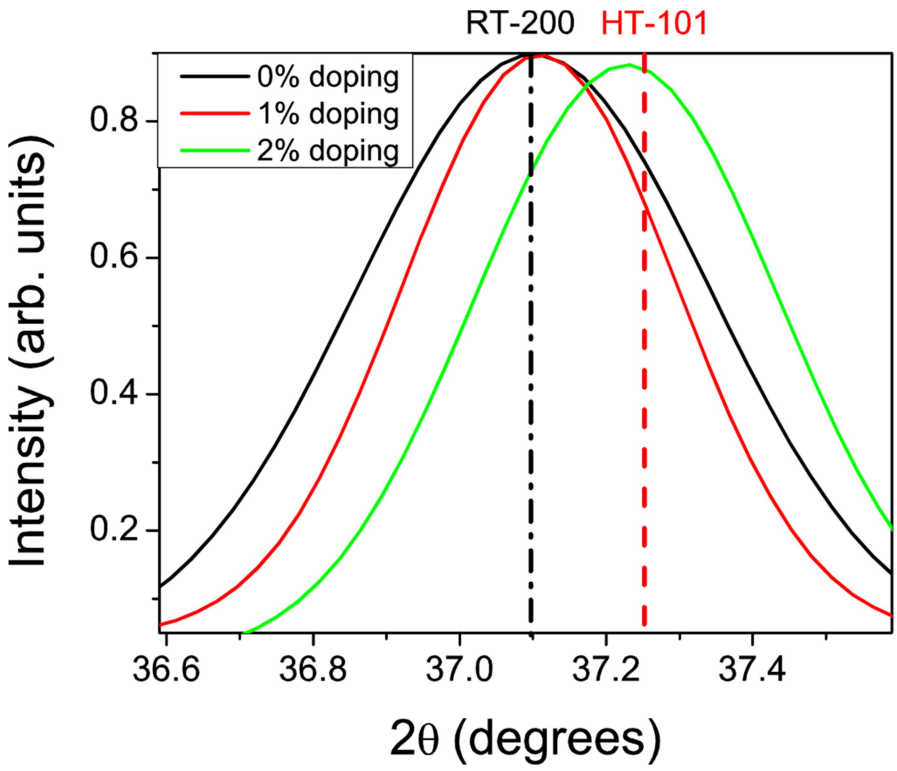

Figure 4.10. Gaussian fits of XRD peak near 37 degrees. As dopant concentration increases the peak shifts from the monoclinic 200 peak to the rutile 101 peak.

As we discussed in the previous section, the morphology of underlying VO_2 films has a large effect on VO_2/Ni bilayers. Because of this, we collected AFM images for films doped at the three characteristic doping concentrations, which are shown in Figure 4.11. The main trend that is seen is a slight decrease in the roughness with increased doping concentrations. A watershed algorithm was used to determine particle sizes of each sample as well. Grain size seems to only

vary by 25% deviation between samples, showing no clear correlation with doping concentration. In the previous study by Lauzier et al.[108], the difference in grain size between samples with small magnetic changes and large magnetic changes is at least 75%, three times as much as the deviation seen between our samples.

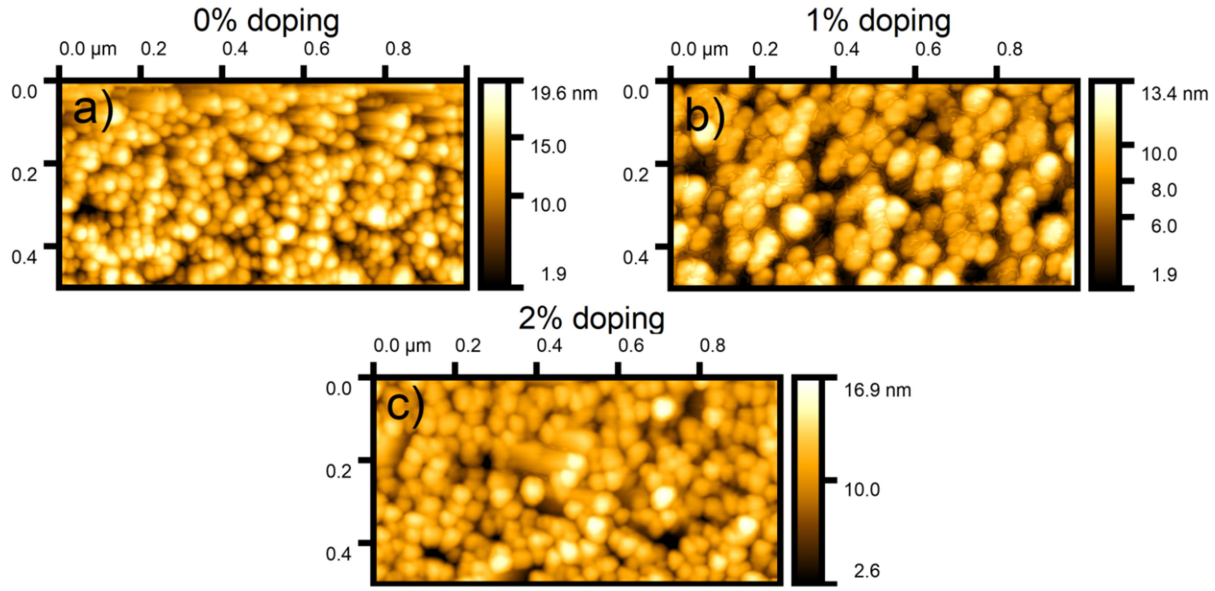

Figure 4.11. AFM scans of doped sol-gel samples at different concentrations. a. A 0% doped sample, with 3.15 nm rms roughness. b. A 1% doped sample, with 2.53 nm rms roughness. c. A 2% doped sample, with 2.28 nm rms roughness. All samples were spun at 3000 rpm.

4.4 Magnetic Measurements of W Doped VO_2/Ni Heterostructures

Due to the promising results seen with both doping and the VO_2/Ni bilayers, the sol-gel technique was chosen to investigate the effects of doping VO_2/Ni bilayers. Sol-gel synthesized doped VO_2 was coated with Ni using the technique described in section 4.2, for both 1% and 2% doped films. Magnetization as a function of applied field measurements were taken of these samples using the VSM, and the coercivities extracted as previously described. The coercivity as a function of temperature for 0%, 1%, and 2% doping concentrations are plotted in Figure 4.12. Both the 1% and the 2% doped films also show a sharp decrease in the coercivity, as was seen in

the undoped films and previous sputtered films. However this sharp change occurs at a much lower temperature, corresponding to the increasing dopant concentration. With 1% doping the sharp decrease was shifted from 340 K to 318 K, and at 2% they were shifted to 297 K. Just as the electrical transport properties were decreased in magnitude, there is a decrease in the magnitude of the sharp change in the coercivity for increased doping, as well as significant broadening. While the 0% doped sample in Figure 4.12 has a 57.3% change, the 1% doped sample has a 47.5% change, and the 2% sample has a significant decrease to a 24.1% change. An absolute decrease in the coercivity is also seen for VO_2's insulating state, from 155 Oe for 0% to 93 Oe for 2%.

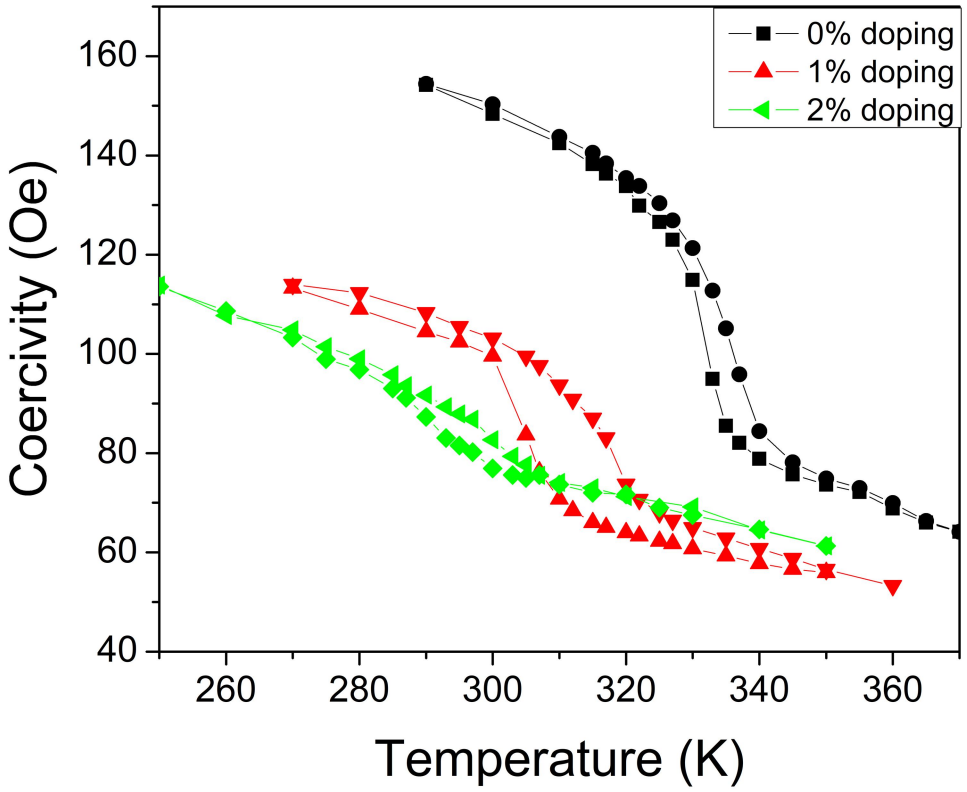

Figure 4.12. Coercivity change as the VO_2/Ni bilayer passes through the VO_2 transition. Samples with 0% dopant concentration, 1% dopant concentration, and 2% dopant concentration are shown.

Magnetic moment as a function of temperature measurements were also taken for these three samples using SQUID magnetometry, with the results shown in Figure 4.13. For the 0% doped sample we once again see a reproduction of previous results in sputtered bilayers, with a sharp increase in the moment coincident with the VO_2 SPT. As was seen with the coercivity change, in the 1% doped sample there is both a decrease in the temperature at which the change occurs as well as a reduction in the magnitude of the change. In this case the temperature was shifted from 335 K to 317 K, and the magnitude decreased from a 3.21% change to a 0.42% change. Unlike with the coercivity change, however, there is no sign of any sharp changes in the magnetic moment of the 2% doped sample. The consistency between the shift in temperatures

for the electrical transport properties and the magnetic properties confirm that the W capping layer did not diffuse through the Ni layer to the VO_2 film. This is not a surprising result, as the W layer was deposited at room temperature and the thickness deposited was only 1/3 of the Ni layer, which only allows for a short diffusion time.

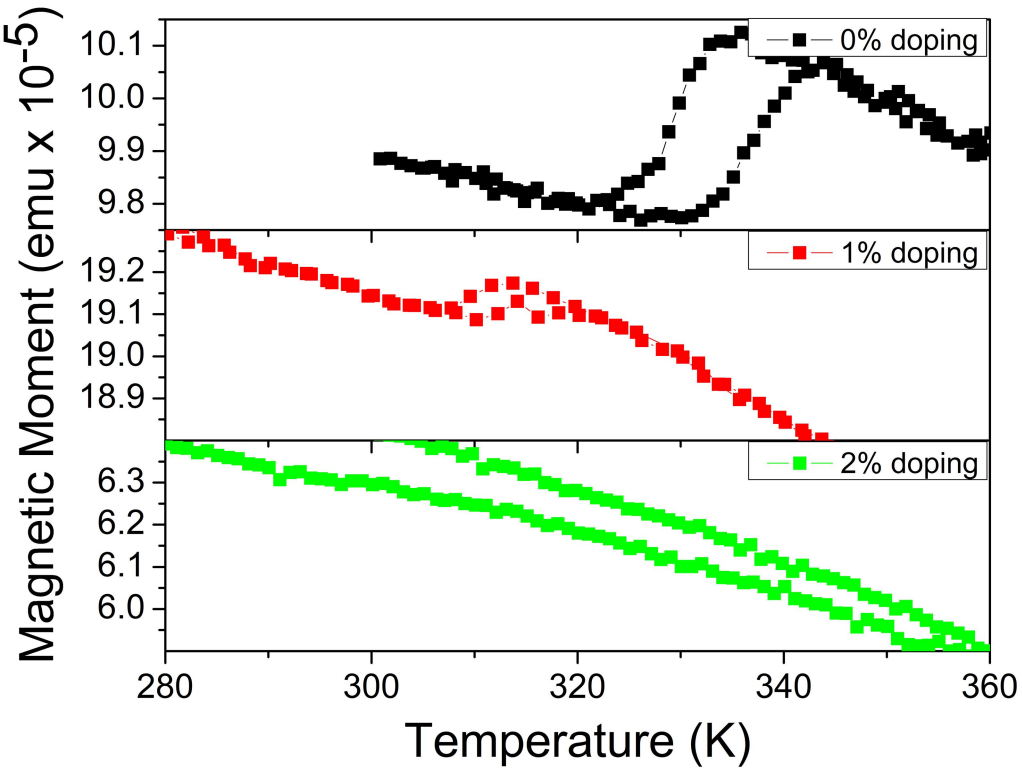

Figure 4.13. Magnetization across the VO_2 transition for bilayer films with three different doping concentrations. No visible change is seen for the 2% doped sample.

Although it has been well established that doping degrades the quality of the MIT in VO_2, there has been some ambiguity as to whether this is simply due to the introduction of carriers to the system or if there is an actual degradation to the SPT which has a larger effect on this MIT reduction. However, as we have already discussed extensively, the type of magnetic changes that are seen in Figure 4.12 and Figure 4.13 are due to the inverse magnetostrictive effect, and is ultimately due to the change in stress the VO_2 layer transfers to the Ni layer during the SPT. The

stress transfer is a wholly structural effect, so the fact that the magnetic changes are decreased must be only due to structural reasons. This degradation of the SPT is most likely due to the stabilization of the rutile phase in the doped films that was demonstrated in Figure 4.9 and Figure 4.10. The results suggest that the SPT is already in a partially transitioned state even below the transition temperature, and thus there will be less remaining monoclinic phase transitioning to rutile. Because of the reduced change in crystalline properties there will be less change in the tensile stress transfer at the interface, in turn causing the reduction in the magnetic properties. The reduction in the SPT could also be due to the creation of the other phases we saw in Figure 4.9, which could be causing distortions in the crystalline lattice of the VO_2 films. Unfortunately, it is ambiguous as to what degree the rutile stabilization or the impurities contribute to this degradation; yet, what we can conclude, is that the MIT degradation must be due to one or both of these, and not just added carrier concentration.

When the magnetization increases as the films go through the VO_2 SPT, the tensile stress between the layers must be decreasing through the transition. Thus the rutile state is the relaxed state, which is not surprising as this is the state in which the Ni is deposited. We can also calculate the stress between the layers for the doped bilayer sample set the same way we did in section 4.2 and section 3.4. For the undoped sample in Figure 4.12 we calculate the stress to be 19 MPa, for the 1% doped sample it is 9 MPa, and for the 2% doped sample it is 7 MPa.

4.5 Conclusions

We refined a sol-gel synthesis technique for the development of VO_2/Ni bilayers. The main problem in the development of this process was the reproducibility for fabricating high quality films. This reproducibility issue was most likely due to water contamination, and resulted

in a film that was not fully converted from V_2O_5 to VO_2. By fabricating the films using a lower acidity process, replacing ethanol with isopropanol, and getting rid of the in-air crystallization step, we reduced this reproducibility problem to a manageable level. Annealing at 450 °C was shown to have a sharper transition than other annealing temperatures, while different spin coating speeds were shown have very little effect on the particle size. Different cuts of sapphire showed minimal differences in their electrical transport, but quartz substrates were shown to have a decreased quality, although still remaining a feasible option if etching is required. The films primarily consisted of monoclinic VO_2, but other unidentified phases were also present. Sol-gel synthesized VO_2/Ni bilayers showed large decreases in coercivity at the VO_2 SPT for HT deposited Ni, and large irreversible changes in RT deposited Ni. Both results reproduce previous results seen in sputtered films, but with smaller magnitude changes.

Both sputtering and sol-gel synthesis techniques were investigated to check their feasibility as techniques for producing W doped VO_2 films, and the effect of doping on the films properties was investigated. The cosputtering technique used to fabricate W doped films resulted in too high of doping concentrations, not allowing for doping concentrations below about 2.3%. Sol-gel synthesis was used to successfully fabricate doped VO_2 films from 0.1-3%, reproducing the shifted electrical transport properties seen in previous studies. Introducing W into the system was shown to stabilize the rutile phase of VO_2 and form impurities, one of which was identified as V_2WO_6. The doping had very little effect on the morphology of the films, however. VO_2/Ni bilayers with a W doped VO_2 layer showed the same magnetic changes as the undoped bilayers, but with a shift to lower temperatures and a decrease in magnitude. The decrease in magnitude of the magnetic change suggests the decrease in the MIT is partially due to a degradation of the

SPT, and this degradation can be explained by either the stabilization of the rutile phase and/or the formation of other phases.

Chapter 5. Optical Properties of VO_2

5.1 Motivation

Thermochromic materials have incited large amounts of interest for their ability to be used in smart devices, optical switches, thermometers, and many other applications. As discussed in Chapter 1, vanadium oxides are often used for their thermochromic properties, with VO_2 attracting particular interest in this field due its ability to be easily used for room temperature applications. Previous studies on the optical changes during the VO_2 transition have mostly focused on ellipsometry measurements in the infrared (IR) range, and have primarily been studies of bulk materials and thick sputtered films.[74,142,143] Few studies have done detailed analyses in lower wavelength ranges with thinner films. Furthermore, most studies have focused on the wavelength dependence of the VO_2 transition and determining optical constants from this. There are very few studies focused on how transmission and reflection change through the transition, let alone any analysis of the details of the transition as a function of temperature. For example, it's well known that in the IR range VO_2 presents a change from a highly transparent and low loss material to a more reflective lossy material through the transition temperature.[144] However the situation is more complicated for other ranges of wavelengths, and this aspect of the transition is not well studied. The situation becomes even more complicated when you consider that the transition's magnitude, broadness, and hysteresis are all influenced by film properties such as the film quality, roughness and grain size, impurities, and substrate.[107,108,145,146]

We first present the ways the optical properties of VO_2 changes through the MIT for different wavelengths in the visible and near IR range. Data for films deposited on different

substrates and with different thicknesses is shown, and possible correlations will be discussed. Morphological considerations are taken into account as well. Next we will discuss how to account for thickness, multiple layers, roughnesses, and absorption when modeling transmission (T) and reflection (R) coefficients. After this we discuss our specific model for the optical properties of VO_2 films and its MATLAB implementation. Finally the results of trying to fit our model to the data collected will be displayed, and fitting parameters discussed.

5.2 Transmission and Reflection From VO_2 Films

Reflectivity data was collected across the temperature range of the VO_2 transition using the setup and procedure described in Chapter 2. All samples were pure VO_2 films, with the substrate and the thickness of the films being the main two controlled parameters varied. Only films with MITs that were optimized for magnitude and sharpness were used, which means that different fabrication conditions had to be used for each substrate deposited on. Each substrate required different fabrication conditions to achieve optimal transitions, and thus may have different crystalline quality. Different thickness films were fabricated for each substrate chosen, from 50 nm, 100 nm, and 200 nm. Films were deposited onto r-cut, c-cut, and a-cut sapphire substrates. All films were fabricated using sputter deposition with the technique described in Chapter 4. R-cut and a-cut samples were fabricated with 2.7 sccm oxygen flow rate, while c-cut samples were fabricated with 2.65 sccm. Deposition temperature was also varied to optimize the transition properties of the films. R-cut and c-cut samples were fabricated at 575 °C, while the a-cut sample was fabricated at 525 °C.

The main method of characterizing the films while optimizing for the transition was by using electrical transport measurements, using the technique described in Chapter 2. Figure 5.1

shows resistance as a function of temperature plots for films deposited on each of the different substrates after the transition properties were optimized. Films show only small differences in their change of magnitude at the transition, with each sample having over 4 orders of magnitude changes in their resistance. There were also only negligible differences in their widths. Both r-cut and c-cut also had only slight differences in hysteresis and transition temperature, with transition temperatures of 340 K and 339 K and hysteresis of 6 K and 4 K respectively. However the a-cut sample had significant differences from the other samples for these two properties, with a higher transition temperature of 349 K and a larger hysteresis of 9 K. The change in the transition temperature for different substrates is well-known, and is an effect of the epitaxial strain that is caused by the substrate to the a and c in plane axes stabilization of the monoclinic phase. Other substrates are known to cause the reverse effect, and can lower the transition temperature almost 10 K.

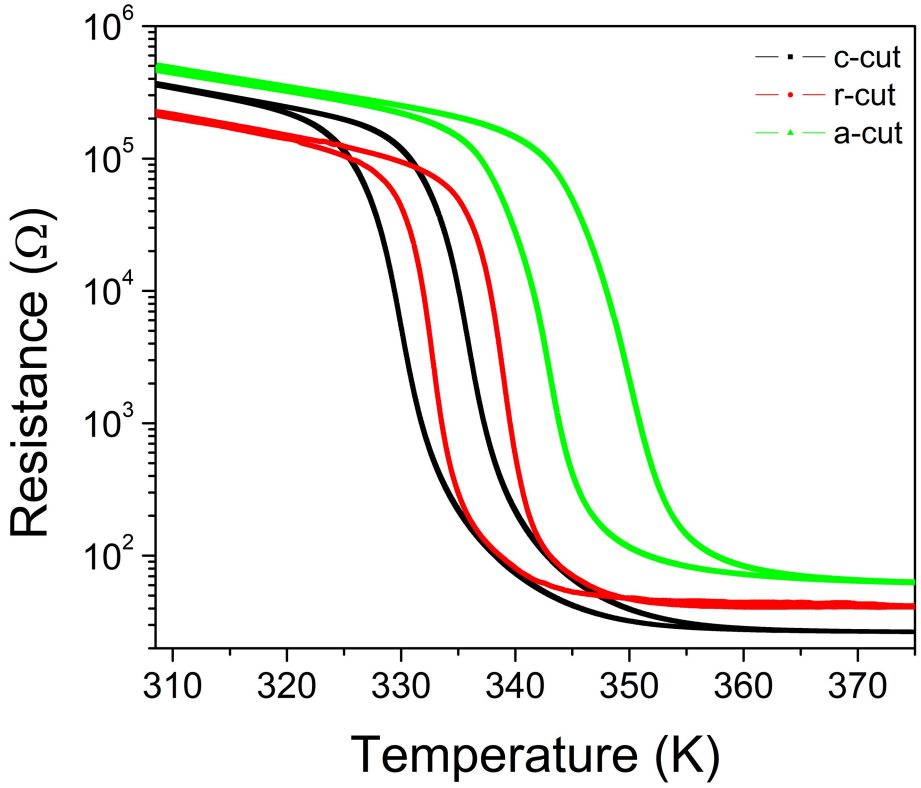

Figure 5.1. Electrical transport measurements for 100 nm VO_2 film samples on different substrates after the quality of the transition was maximized. Magnitude of transition and broadness is similar for all samples, with main difference seen in hysteresis and transition temperature.

Crystallographic, structural, and morphological data were collected to both confirm the quality of the films and to determine other properties of the films that may be relevant to their optical properties. Figure 5.2 shows the XRD plot for an optimized VO_2 film deposited onto c-cut. Besides substrate peaks the only visible x-ray peaks seen are from monoclinic VO_2, suggesting little impurity. Although the signal to noise ratio for the VO2 peaks is low, this is typical of most of the sputtered films measured using the particular instrument and not indicative of a low crystalline quality. We also see in Figure 5.3 the XRR data for an r-cut sample, which indicates that the thickness of the film was approximately 105 nm. Film deposition times for all

samples discussed after this point were appropriately adjusted to reflect the desired thicknesses stated.

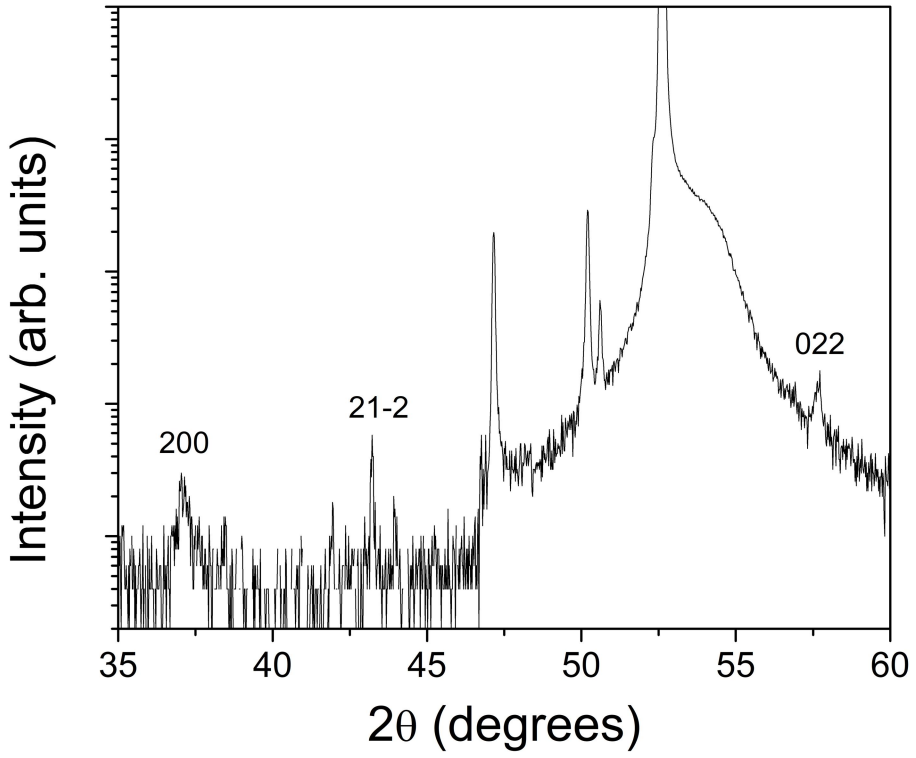

Figure 5.2. XRD pattern for a sputtered VO_2 film on c-cut sapphire. VO_2 peaks are identified, while all unidentified peaks correspond to the substrate.

As roughness is known to have an effect on the reflectivity of surfaces, particularly affecting the amount of diffuse versus spectral reflections that occur, for each sample that had optical data collected, AFM data was also collected. Several examples are shown in Figure 5.4 and Figure 5.5 for AFM images of different sample sets. In Figure 5.4 we see a comparison of 50 nm films sputtered onto the different substrates. While the a-cut and the r-cut have similar roughnesses, 0.39 and 0.4 nm respectively, the c-cut sample has a higher roughness of 1.3 nm. Films deposited onto c-cut were always somewhat rougher than the same thickness films

deposited onto a-cut and r-cut. Grain size analysis was also done on all AFM images, yielding grain sizes of 26.71 nm, 36.11 nm, and 44.22 nm for the r-cut, c-cut, and a-cut respectively shown in Figure 5.4. R-cut samples did tend to have larger particle sizes, however no other clear trends were seen.

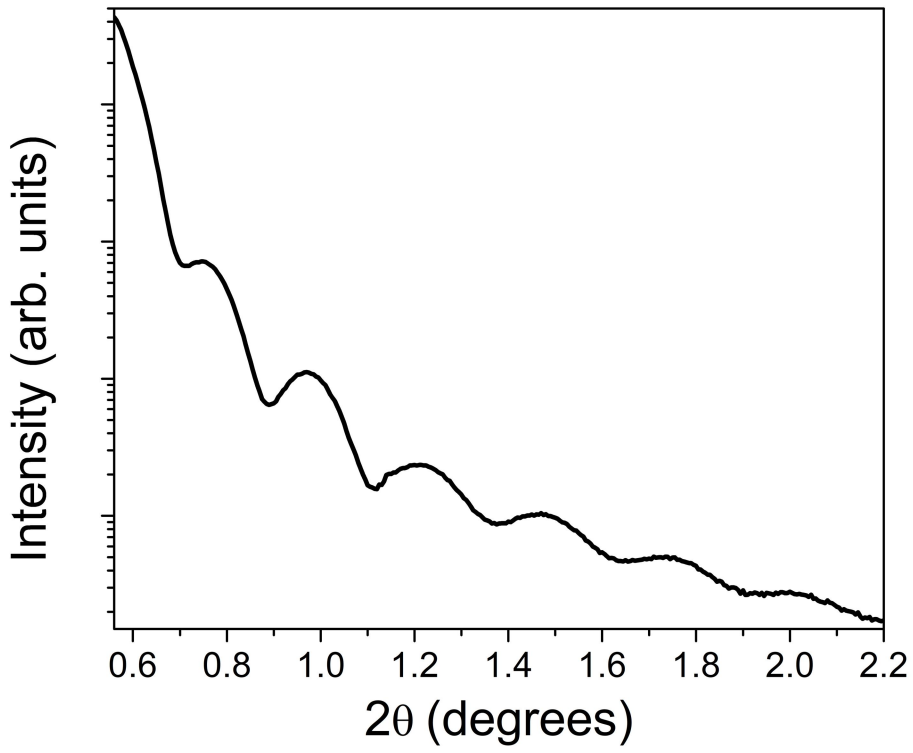

Figure 5.3. XRR scan of an r-cut VO_2 film. Distance between oscillations was 0.21°, which corresponds to a thickness of ~105 nm.

Figure 5.5 shows a comparison of different thicknesses (200 nm, 100 nm, 50 nm) of VO_2 film deposited on r-cut sapphire. We see that, generally, the films are rougher the thicker they are, which was true for all samples except for the 200 nm c-cut film. Thus, it appears that longer deposition times seem to affect the roughness; however, there is also enough variability in the

trend to suggest that other uncontrolled factors are also playing a role. Table 5.1 shows both the rms roughness and the average particle size for each film analyzed.

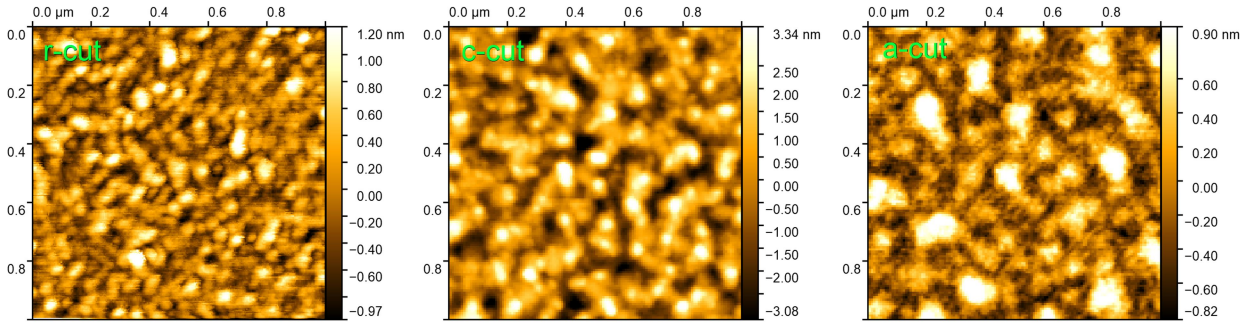

Figure 5.4. AFM images of 50 nm sputtered VO_2 films on 3 different substrates. Images are 1 nm by 1 µm cross-sections. The r-cut sample has an rms roughness of 0.4 nm, the c-cut sample 1.3 nm, and the a-cut sample 0.39 nm.

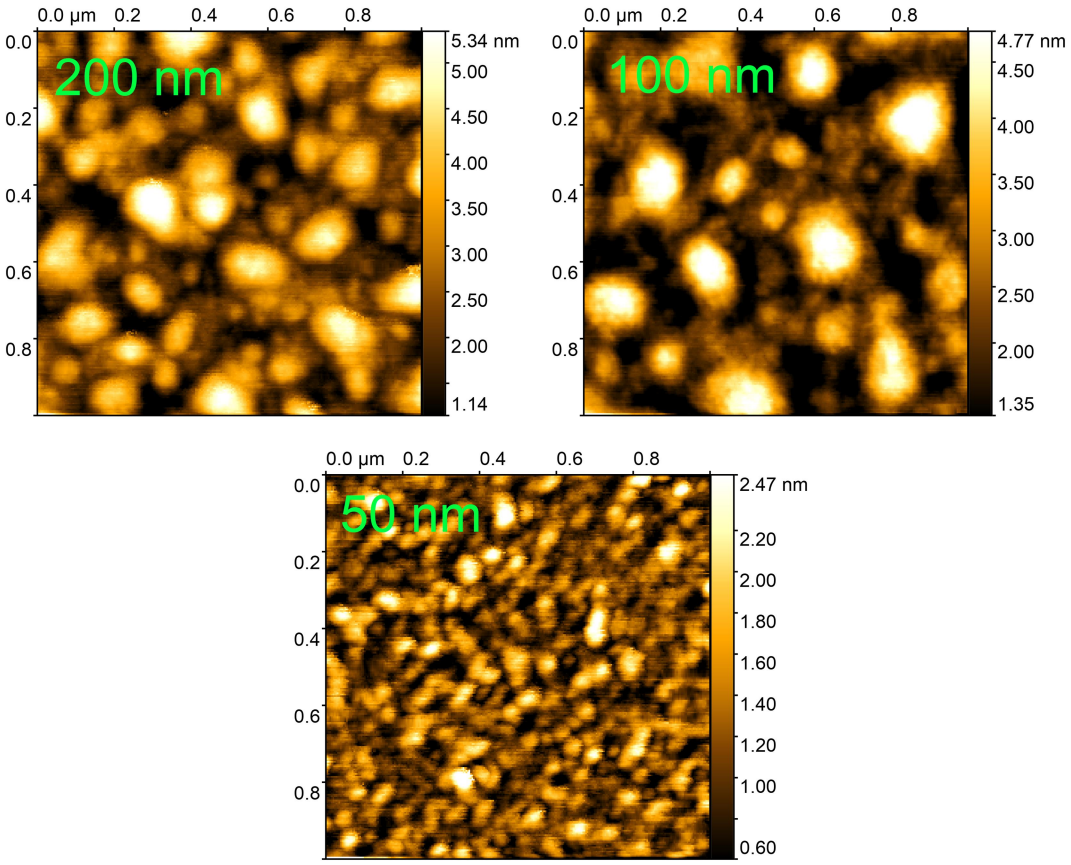

Figure 5.5. AFM images of sputtered VO_2 films with different thicknesses on r-cut sapphire. Images are 1 x 1 μm^2 cross-sections. The 200 nm sample had an rms roughness of 1.02 nm, the 100 nm a roughness of 0.97 nm, and the 50 nm a roughness of 0.4 nm.

All reflectivity measurements were taken using the technique described in Chapter 2. Unlike what was expected, which was that the reflectivity would be low and the transmissivity high in the insulating state, with the reverse in the metallic state, we instead observed a much more complex behavior. The response of the reflectivity and transmissivity for different films showed a complex behavior both quantitatively and qualitatively. One of the more striking results is shown in Figure 5.6, which is that there is a large downward bump in the reflectivity that appears at the higher temperature end of the transition. This was surprising, both because there was no discussion in the literature about these effects being observed in the reflectivity, as

well as the fact that it was so commonly observed in our films. The cause of this is not clear, and may be due to either scattering, anomalous absorption, or interference effects.

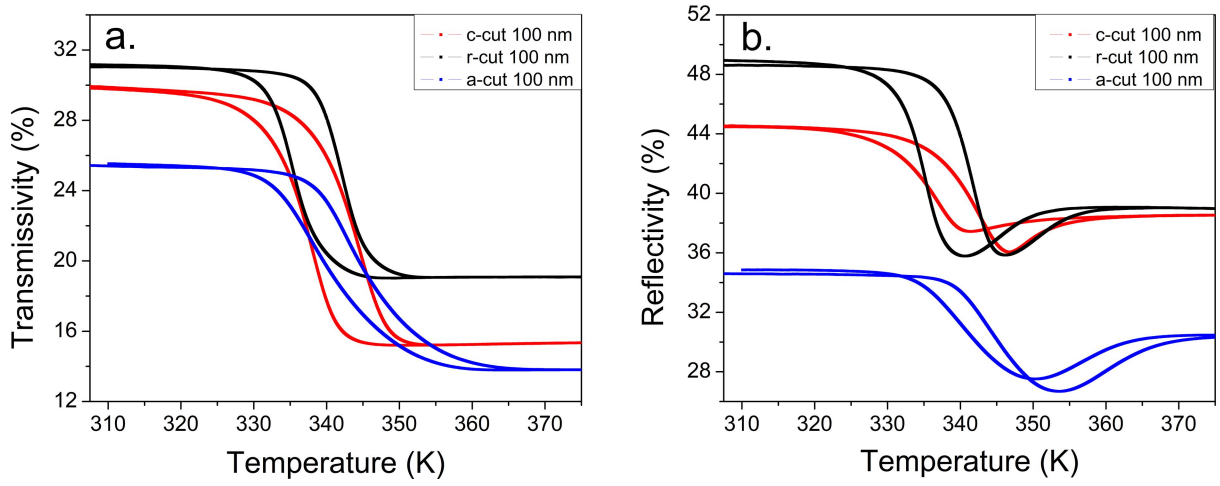

Figure 5.6. a. Transmissivity as a function of temperature across the VO_2 transition for 100 nm VO_2 films deposited on different substrates. b. Reflectivity curves for the same films. All data was collected with 980 nm light. Each curve chosen showed a downward bump at the end of the transition in the reflectivity.

We see from Figure 5.6 that this bump is present across the films on different substrates and thicknesses for reflectivity at 980 nm, although it is not clear from this data what influences the magnitude of these downward bumps. The largest downward bump observed was an almost 10% deviation from the final metallic state intensity, while the smallest was less than 0.5%. Although the downward bump was primarily seen in the reflectivity at 980 nm, it was also seen in the transmissivity for a 100 nm r-cut film at 980 nm and a 200 nm r-cut film at 635 nm. Another similar anomalous effect is an upward bump seen in the 405 nm transmission of the 100 nm r-cut sample. Upward bumps were also seen in some of the less optimized films measured, either 100 nm r-cut samples or 100 nm c-cut samples, possibly suggesting that both the thickness and a property determined by crystalline quality play a role in this.

The most common behavior at the transition across all wavelengths was for both the reflectivity and transmissivity to decrease across the transition, suggesting that the metallic state was more absorbing for the metallic state of most samples. An example of a 200 nm c-cut film which has this more typical behavior for all wavelengths is shown in Figure 5.7. The second most commonly seen behavior seen was the reflectivity decreasing but the transmissivity increasing. An example of this is shown in Figure 5.8a and Figure 5.8b, for a 50 nm r-cut film at 405 nm and 635 nm. This behavior was seen only in lower thickness films at 635 nm and 405 nm, and we can see from Figure 5.8c that the behavior is the typical downward transition seen previously, including the slight downward bump. We can also see from Figure 5.8a how the 405 nm data tends to have smaller changes in the transition, and very little transmission in general.

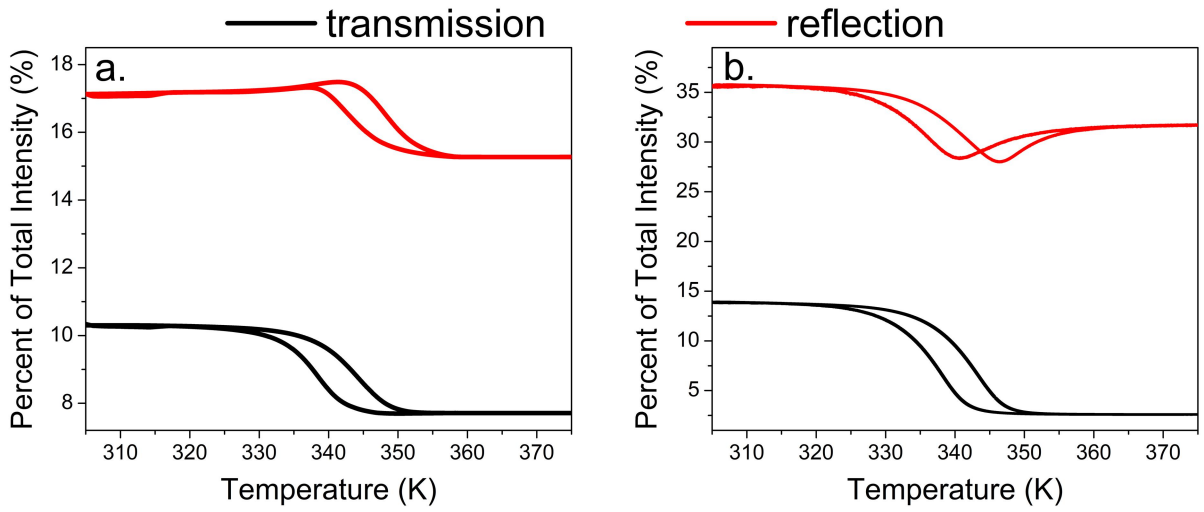

Figure 5.7. Transmissivity and reflectivity for two wavelengths as a function of temperature across the VO_2 transition for a 200 nm VO_2 film on c-cut with different transition properties. a. Collected at 635 nm. b. Collected at 980 nm. Both reflectivity and transmissivity decrease through the transition for both wavelengths.

There was only one sample that diverged from either of the two cases described above for how the reflection and transmission change at the transition, and that was the 200 nm film deposited on r-cut sapphire. The data for this sample at 980 nm is shown in Figure 5.9, where we

see that the reflectivity for this sample increased, while the transmissivity decreased. This data also shows a downward bump and a kink in the transition of the reflectivity, suggesting this film possesses some unique quality that the other films do not.

Table 5.1 shows a summary of the primary data set of optimized films, displaying both the roughnesses and particle sizes for each film as was previously stated, but also describing how the transmissivity and reflectivity either decreases or increases at the transition (or shows no change), and if there are any upward or downward bumps in the data. There was no clear correlation between the magnitude of the transition and either the particle size or roughness of a film. The particle size shouldn't have a large effect (or possibly any effect) on the transmission or reflection so this is not unexpected; however the roughness definitely should affect both of them.

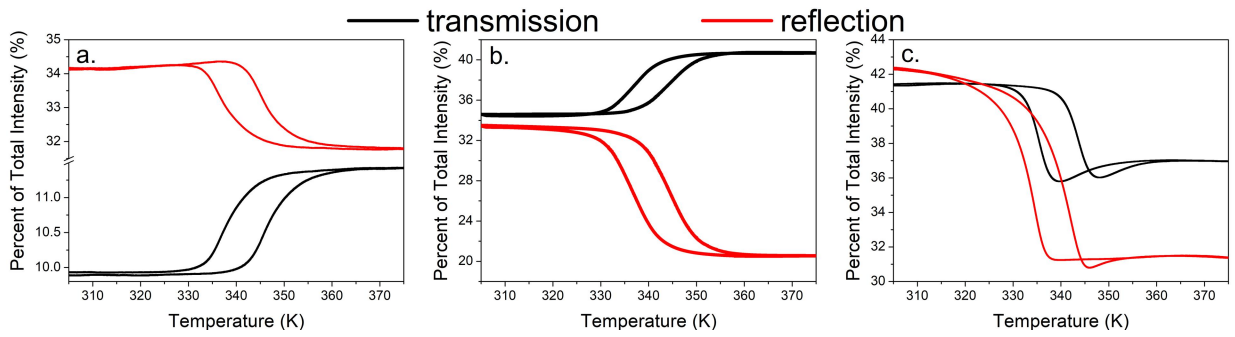

Figure 5.8. Transmissivity and reflectivity as a function of temperature across the VO_2 transition for a 50 nm VO_2 film on r-cut for 3 different wavelengths. a. Collected at 405 nm. b. Collected at 635 nm. c. Collected at 980 nm. For the 405 nm and 635 nm, the reflectivity shows a decreases while the transmissivity an increase, whereas the 980 nm data shows a decrease in both the reflection and transmission at the transition.

Thus the correlation between the roughness and the observed changes in these properties at the transition are most likely complicated and indirect. Although, as we have discussed, we did observe some clear trends in what types of samples are likely to have the different qualitative differences in their transmissivity and reflectivity through the transition, there is no clear trend

that helps explain what determines quantitative aspects of the transition, such as the percent change or the absolute insulating/metallic state transmission/reflection. Thus further analysis of the data is needed to help explain results.

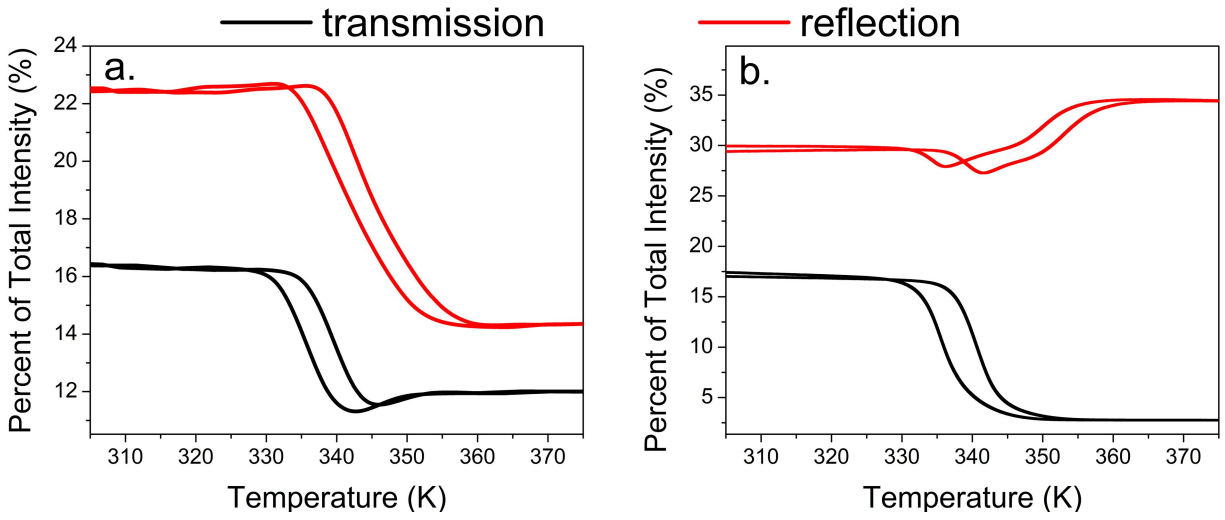

Figure 5.9. Transmissivity and reflectivity as a function of temperature across the VO_2 transition for two different wavelengths for a 200 nm VO_2 film on r-cut. a. Collected at 635 nm. b. Collected at 980 nm. Both transmissivity and reflectivity show a decrease in magnitude at the transition for 635 nm, and a small downward bump is present in the transmissivity. The reflectivity increases while transmissivity decreases at the transition for the 980 nm data, and double switching behavior and a downward bump are also present in the reflectivity.

Table 5.1. Comparison of fabrication conditions with morphology and optical results. Substrate type, thickness, roughnesses and particle sizes for each film are described in the first two columns. Percent change in the transmissivity (T) and reflectivity (R) for different wavelengths is shown in the next columns. It is also specified if T and R either decreases or increases at the transition (or shows no change).

Substrate	Thickness Rms roughness Grain size (nm)	Wavelength					
		405 nm		635 nm		980 nm	
		ΔT	ΔR	ΔT	ΔR	ΔT	ΔR
c-cut	200 0.93 33.54	22.22% Decrease	10.1% Decrease	28.57% Decrease	15.39% Decrease	142.85% Decrease	13.33% Decrease
	100 1.85 41.73	0% -	6.67% Decrease	12.5% Decrease	0% -	66.67% Decrease	14.63% Decrease
	50 1.3 36.11	6.32% Decrease	4.65% Decrease	11.11% Increase	41.38% Decrease	11.77% Decrease	41.27% Decrease
r-cut	200 1.02 44.15	16.22% Decrease	0% -	28.57% Decrease	40% Decrease	150% Decrease	15.87% Increase
	100 0.97 70.42	37.04% Decrease	7.14% Decrease	18.02% Decrease	15.39% Decrease	48% Decrease	22.73% Decrease
	50 0.4 26.71	20% Increase	9.23% Decrease	13.33% Increase	49.06% Decrease	8.16% Decrease	27.03% Decrease
a-cut	100 0.49 20.96	28.57% Decrease	3.18% Decrease	20.41% Decrease	12.9% Decrease	59.74% Decrease	12.5% Decrease
	50 0.39 44.22	3.97% Decrease	5.56% Decrease	8.7% Increase	20.64% Decrease	60.47% Decrease	27.69% Decrease

5.3 Modeling VO_2 Optical Transition For R and T

In section 2.11, we discussed the basic theory behind reflection and transmission at a thin film interface, but did not discuss how to account for multiple surfaces, absorption, or rough interfaces. Although we are investigating only a single layer VO_2 film, it is important to develop a model for multiple surfaces, as we end up modeling our roughness as an extra effective layer in our film system. There are several different ways that all of these additional properties of a film system can be accounted for, but we will focus solely on the theory we used in our MATLAB implementation. Although we will cover the theory with a necessary amount of detail, a greater detail derivation for how we account for absorption and multiple is given by Pascoe.[147] We will also limit our discussion to that corresponding to s-polarization, as the p-polarization theory requires separate treatment. This theory accounts for both multiple layers and absorption at each layer simultaneously, unlike other common theories that account for at most 2 layers of absorbing materials or account for an arbitrary number of layers that are instead lossless. Similarly, further details behind the theory we used to account for roughness are described in Carniglia et al.[148]

In basic theory, the transmissivity and reflectivity add to unity, as we assume that the light cannot interact in any other manner. Although some theories behind absorption can account for its effects while maintaining this relationship, we chose a theory behind the absorption which instead used the following relationship,

$$T + R + A = 1 \qquad 5.1$$

Here A is the absorptivity of the film, the percent of the incoming light which was absorbed rather than reflected or transmitted. The absorption of each layer is accounted for by three related

physical properties: the complex refractive index, y; the propagation constant, γ; and the admittance, Y. Because the admittance is a function of the propagation constant, and the propagation constant is a function of the refractive index, the refractive index is ultimately the important property. They are related to each other by the following two equations:

$$\mathrm{Y} = \gamma \mathrm{y} \lambda c \epsilon_0 \mathrm{j} \qquad 5.2$$

$$\gamma = \frac{2\pi \mathrm{y} \mathrm{j}}{\lambda} \qquad 5.3$$

where c is the speed of light in vacuum, ϵ_0 is the permittivity of free space, and λ is the wavelength of the incident light. Remember that y is complex, so both the admittance and the propagation constant can have complex and real components, each of which are representative of different physical effects. The method chosen to account for the multiple absorbing layers is by associating each layer with a characteristic matrix, analogous to the transfer matrix method commonly used to calculate the effects of sending a ray through a series of optical components. To form these matrices, the relevant properties are the complex refractive index of a layer, the incident angle on the first surface, the thickness of the layer, and the polarization.

We define the correction to the admittance for s polarization that takes into account the angle which the ray travels through the film to be

$$\eta = \mathrm{Y} \cos\theta \qquad 5.4$$

To help clean up our matrix we also define the variable δ to be

$$\delta = \gamma \, \mathrm{d} \, \cos\theta \, \mathrm{j}, \qquad 5.5$$

which is representative of the path length which the EM wave has to take. In this equation, d is the thickness of the layer. We can now form the characteristic matrix of a layer, which is a

representation of the propagation of both the electric field and the magnetic field through the layer, as follows:

$$\mathrm{M} = \begin{bmatrix} \cos\delta & \frac{\sin\delta}{\eta} j \\ \eta \sin\delta & \cos\delta \end{bmatrix} \tag{5.6}$$

Then, to calculate the effects of the whole film system, we have to multiply the matrices for each layer, including the initial propagation material (vacuum in our case). This can be represented mathematically as

$$M_{total} = \prod_{i=1}^{n_{layers}+2} M_i \tag{5.7}$$

where M_i is the characteristic matrix a layer, n_{layers} is the number of layers, and M_{total} is the resultant matrix representing the whole system. The first matrix, M_1, which represents the initial propagation media, needs to be treated separately and is instead described by a matrix for a traditional lossless material. A diagram that demonstrates how each layer has a different matrix and material properties is shown in Figure 5.10.

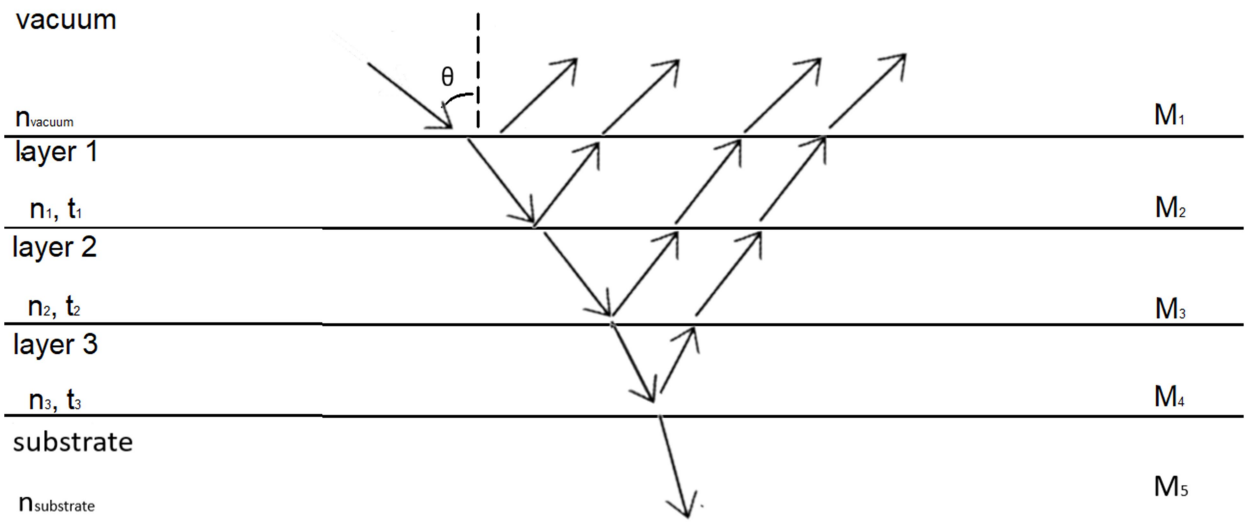

Figure 5.10. Ray incident upon a 3 layered film. All three layers are labeled with their respective indices and thickness, as well as the associated representative matrix. We see that the first and last matrix actually correspond to the media the film is in and the substrate the film is on respectively. What is not shown is that there can also be back reflections from the reflected rays, which illustrates the complex nature of transmission and reflection in multilayers.

The system of equations the final matrix represents is then able to be used to solve for the reflection and transmission coefficients. The matrix which represents the whole system can be expressed by its components as follows,

$$M_{total} = \begin{bmatrix} m_{11} & m_{12} \\ m_{21} & m_{22} \end{bmatrix} \tag{5.8}$$

which allows us to express the reflection coefficient as

$$\rho = \frac{\eta_{vacuum}(m_{11} + m_{12}\eta_{substrate}) - (m_{21} + m_{22}\eta_{substrate})}{\eta_{vacuum}(m_{11} + m_{12}\eta_{substrate}) + (m_{21} + m_{22}\eta_{substrate})} \tag{5.9}$$

Although we didn't show the derivation of the traditional reflectivity and its relationship to the reflection coefficient in Chapter 2 (as was stated there, this is due to the fact that it is so well known), the relationship between the reflection coefficient in this theory is no different from the traditional theory:

$$R = \rho\rho^* \tag{5.10}$$

Similarly the transmission coefficient can be calculated to be

$$\tau = \frac{2\eta_{vacuum}}{\eta_{vacuum}(m_{11} + m_{12}\eta_{substrate}) + (m_{21} + m_{22}\eta_{substrate})}, \tag{5.11}$$

with the transmissivity being related to it in our theory with only a slight modification:

$$T = \mathrm{Re}(\frac{\eta_{substrate}}{\eta_{vacuum}})\tau\tau^* \tag{5.12}$$

Lastly, the absorptivity can now be calculated by using equation 5.1. We must use an intermediate variable,

$$\varphi = \eta_{vacuum}(m_{11} + m_{12}\eta_{substrate}) + (m_{21} + m_{22}\eta_{substrate}), \tag{5.13}$$

to clearly express the full expression as

$$A = \frac{4\eta_{vacuum}[(m_{11} + m_{12}\eta_{substrate})(m_{21} + m_{22}\eta_{substrate})^* - \eta_{substrate}]}{\varphi\varphi^*} \tag{5.14}$$

This sums up the main results of the theory we used for dealing with absorption and multiple layers. The three equations derived for R, T, and A are implemented in our MATLAB program directly to determine these quantities. The required input parameters for this implementation are the refractive indices of each layer as well as the initial propagation media and the substrate, the thickness of each layer including the substrate, the incident angle, and the wavelength of the EM wave.

There are many different theories which can account for the roughness, some of them requiring significant modifications which would have been difficult to combine with the absorption/multilayer model chosen. We must also take into account what roughness range we

are dealing with, as smaller roughnesses will have mainly specular reflections while larger roughnesses will have diffuse reflections. As we saw in the previous section, the highest roughness for our sample set was 1.85 nm. The range for spectral reflection is generally below 10 nm of roughness, and above 15 nm of roughness is when diffuse reflections start to have a large effect on the system. Thus our films are well within the range dominated by spectral reflection, so a theory which deals with this range is required for accurate modeling. To satisfy both of the considerations above, a much simpler theory that both only considers spectral reflections and is compatible with our absorption theory was used, and is based on modeling the roughness as an effective (single) layer in and of itself that mixes the properties of the two layers of the rough interface. A diagram illustrating this is shown in Figure 5.11. Although the concept behind the idea is sat face value, the actual mathematics behind it are very complicated. Because of this many steps will be omitted to keep our derivations at a reasonable length.

Although we will not discuss the details behind the theory that justifies why we can simply treat the surface like another absorbing layer in a multilayer system, we show how to get the effective material properties that are needed properly model the layer; namely, the real part of the refractive index, the imaginary part of the refractive index, and the thickness. The real part of the refractive index is easily determined by assuming the layer is an equal mixture of the media it's coming from and the media that it's going into, as we can then use the Drude effective medium approximation[149] result

$$n_{eff}^2 = \frac{n_1^2 + n_2^2}{2}, \qquad 5.15$$

where n_1 is the refractive index of the first material, n_2 is the refractive index of the second material, and n_{eff} is the effective real index of refraction of the roughness layer. As our first material is just the vacuum, this simplifies to

$$n_{eff} = \sqrt{\frac{1 + n_2^2}{2}} \qquad 5.16$$

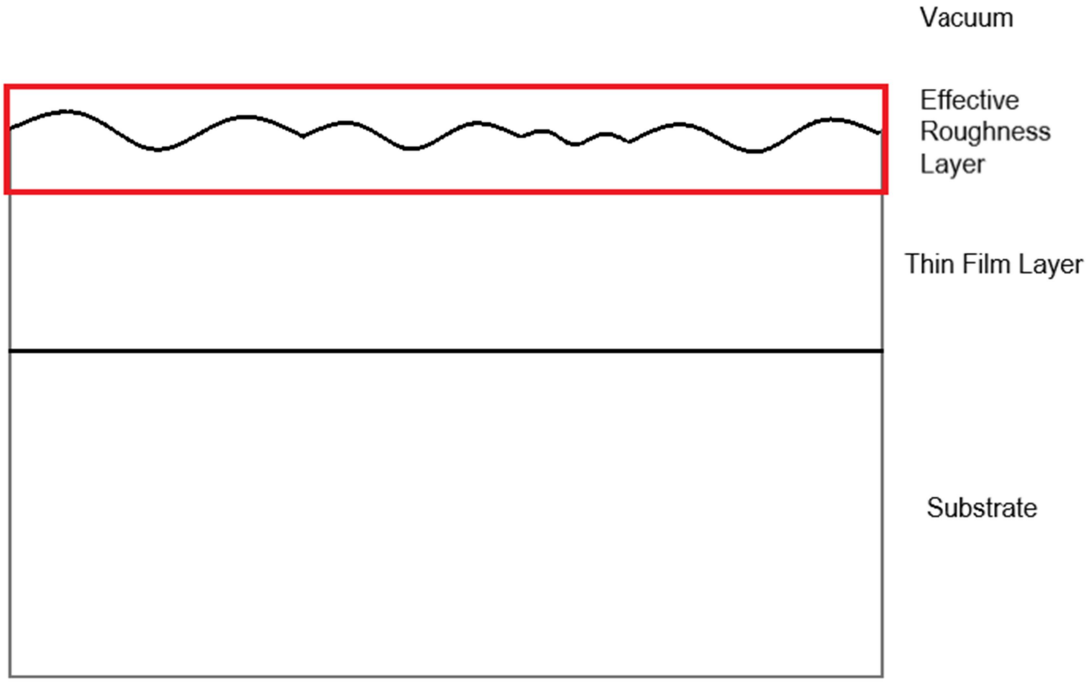

Figure 5.11. Illustration of how the region of roughness at the interface can be considered its own effective thin film layer with intermediate properties between the vacuum and the film.

To get the other two properties required for our model, we have to first discuss what we expect to see for a smooth layer at an interface, and then represent the roughness as a random function with a Gaussian distribution across the surface. If the autocorrelation length is large in comparison to the wavelength we are using, then we can use a scalar scattering theory to model

the difference in the transmission and reflection when adding the roughness distribution. The results of using such a model are given by[150] the following two equations:

$$\Delta R = -R_0 \left(\frac{4\pi n_1 \sigma}{\lambda}\right)^2 \quad 5.17$$

$$\Delta T = -T_0 \left(\frac{4\pi (n_1 - n_2)\sigma}{\lambda}\right)^2 \quad 5.18$$

where R_0 and T_0 are the reflectivity and transmissivity for a smooth interface, and σ is the roughness. Next, we must consider the properties of a thin absorbing layer at the interface of two media that has a thickness d, real refractive index n (given by equation 5.15), and imaginary refractive index k. The reflectivity for such a system can be expressed as

$$R = \frac{r_1^2 + 2Re\left(r_1^* r_2 e^{-i\delta_r}\right)e^{\delta_i} + r_2^2 e^{2\delta_i}}{1 + 2Re(r_1 r_2 e^{-i\delta_r})e^{\delta_i} + r_1^2 r_2^2 e^{2\delta_i}} \quad 5.19$$

where δ_r and δ_i are the real and complex δ's for the thin absorbing layer, r_1 is given by

$$r_1 = \frac{n_1 - n + ik}{n_1 + n - ik}, \quad 5.20$$

and r_2 is given by

$$r_2 = \frac{n - ik - n_2}{n - ik + n_2} \quad 5.21$$

Similarly the transmission can be expressed as

$$T = \frac{\frac{n_2}{n_1} t_1^2 t_2^2 e^{\delta_i}}{1 + 2Re(r_1 r_2 e^{-i\delta_r})e^{\delta_i} + r_1^2 r_2^2 e^{2\delta_i}} \quad 5.22$$

where t_1 is given by

$$t_1 = \frac{2n_1}{n_1 + n - ik}, \tag{5.23}$$

and t_2 is given by

$$t_2 = \frac{2(n - ik)}{n - ik + n_2} \tag{5.24}$$

We can assume that the thickness of the effective layer must be very small, especially for lower roughnesses. Thus both δ's must be very small, and because of this we can expand T and R into powers of the two δ's and collect only terms up to the 2nd order. Plugging in equation 5.15 in a way that helps simplify the expression as well as appropriate factoring reduces the expression for the reflectivity to

$$R = R_0\left(1 + \frac{n_1}{n}\delta_i - \frac{n_1(n_1^2 + 3n_2^2)}{n^2(n_1^2 - n_2^2)}k\delta_r - \frac{n_1 n_2}{4n^2}\delta_r^2\right) \tag{5.25}$$

where R_0 is the reflectivity for the system without the added absorbing layer. Similarly the transmission can be expanded and simplified to

$$T = T_0\left(1 + \frac{n_1 + n_2}{2n}\delta_i - \frac{(n_1 - n_2)^2}{n^2(n_1 + n_2)}k\delta_r + \frac{(n_1 - n_2)^2}{16n^2}\delta_r^2\right) \tag{5.26}$$

where T_0 is the transmissivity for the system without the added absorbing layer. By taking the difference between R_0 and R, and T_0 and T, we can determine ΔR to be

$$\Delta R = \frac{4\pi n_1 d}{\lambda}\left(\frac{4kn}{(n_1^2 - n_2^2)} + \frac{\pi n_2 d}{\lambda}\right) \tag{5.27}$$

and ΔT to be

$$\Delta T = \frac{\pi d}{\lambda}\left(\frac{8kn}{(n_1 + n_2)} + \frac{\pi(n_1 - n_2)^2 d}{\lambda}\right) \tag{5.28}$$

Equating these with their equivalent terms from scalar scattering theory allows us to solve for the two properties we desired. We see that the thickness ends up being simply twice the roughness,

$$d = 2\sigma, \tag{5.29}$$

and the complex refractive index is given by

$$k = \frac{\pi(n_1 - n_2)^2(n_1 + n_2)}{4n}\frac{d}{\lambda}, \tag{5.30}$$

Again plugging in 1 for our refractive index of the vacuum layer, our expression reduces to

$$k = \frac{\pi(1 - n_2)^2(1 + n_2)}{4n}\frac{d}{\lambda} \tag{5.31}$$

The final model combines the two models we've discussed, using the representative matrix model with absorption to model the system as 2 layers in a vacuum, the roughness layer defined above with the VO_2 layer below it, on a sapphire substrate. The main unknown parameter for each film at a set temperature is the refractive index, as the other properties are known from the data collected. To model the effect of the VO_2 transition, we assume that there are different refractive indices for the insulating and metallic state, and that the grains of VO_2 will switch according to a Gaussian distribution across the transition. Although this is not as accurate as other models, such as percolation models, of the VO_2 transition, it is far more computationally efficient. Thus, the refractive index can be modeled as a modified error function as temperature increases across the VO_2 transition, with the switching dependent on the insulating and metallic states refractive indices. The transition temperature and the hysteresis of the transition can be determined easily from collected data, so the transition parameter to be determined by the model is limited to the width. The final unknown parameter is the attenuation due to other scattering sources in the system. A Levenberg-Marquardt (LM) non-linear least

squares algorithm, modified to allow for trust regions, was used to refine the parameters for insulating real refractive index, insulating imaginary refractive index, metallic real refractive index, metallic imaginary refractive index, the width of the transition, and the attenuation with respect to the associated transmission/reflection data sets. For many data sets there was only a limited range of possibilities for several of these parameters, so the degree of freedom was often far less than what would be assumed from the 6 free parameters described above.

5.4 Comparison of Data and Model

The model described in the previous section was implemented using a MATLAB program. The jreftran package[151], which is a MATLAB implementation of the RTA matrix calculations discussed above, was used as template for the development of our program. Although an attempt was made to model all of the data of all of the samples in Table 5.1 using the model, it was only possible to obtain a reasonable fit for 14 of the 24 data sets collected. This was most often due to the fact that the magnitude change of either the transmissivity or reflectivity was extremely small, which allowed for too many possible parameter solutions with equal amounts of feasibility. Thus, determining what parameters uniquely fit this data set was unfortunately impossible for these cases. For the rest of the cases, no parameters in the feasible range for VO_2 could reproduce both the correct magnitudes of the metallic and insulating state transmission/reflection, and the correct shape of the curve of the transition (bump/no bump). There are several feasible reasons for why the model failed in these instances. Slight deviations in the angle or polarization during data collection that weren't accounted for is one of the more likely reasons, as the model can be extremely sensitive to slight changes in angle for certain systems. Another very likely reason is that it's a failing of the model itself, which may not account for some of the more complex interactions in certain films. Despite these failings, the

model was indeed able to reproduce most of the main features of the reflectivity/transmissivity data sets discussed in section 5.2. A summary of the results from the fits is given in Table 5.2. An example of a fit of a typical data set is shown in Figure 5.12, a fit of a data set with a downward bump is shown in Figure 5.13, and a fit of the anomalous data set that we discussed in section 5.2 is shown in Figure 5.14.

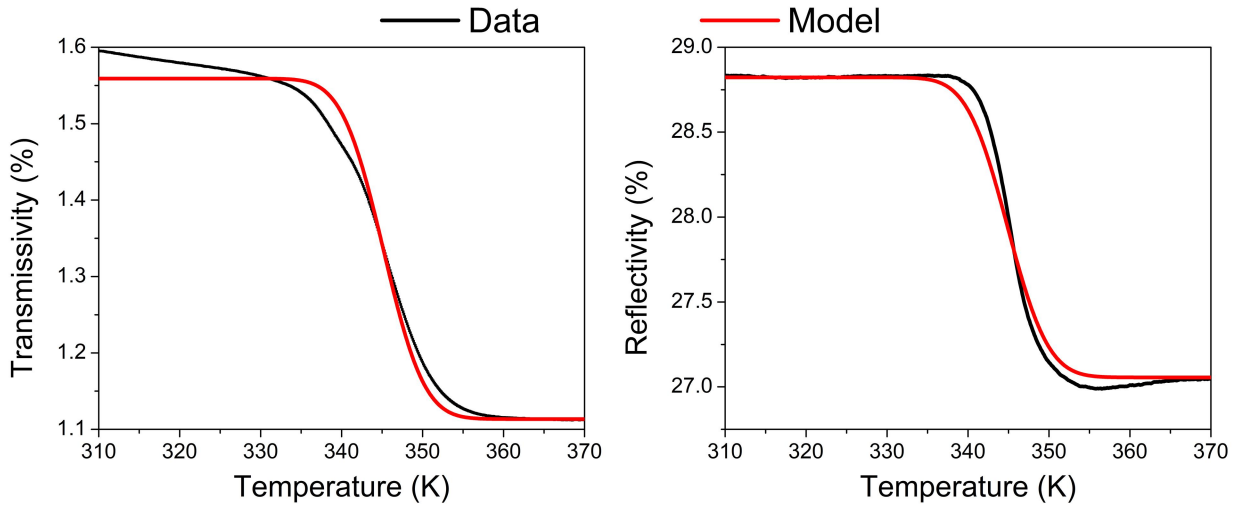

Figure 5.12. Example of a fit of the model to a transmission/reflection data set for VO_2 film with the typical behavior across the transition. For a 100 nm film on r-cut with 405 nm incident light. Refractive indices fit to be 2+0.38j for metallic state and 1.93 + 0.37j for the insulating state. This is comparable to values, albeit on the lower end of the range for n, determined from previous studies at this wavelength, which typically have n's from 1.8-3 and k's from 0-1 at the lower wavelengths. Studies have also shown that the insulating and metallic state values for n are usually very close at this wavelength.[89,152,153]

The comparison of the model to the data that is shown in Figure 5.12 is a demonstration of how well the model is able to fit to the most commonly observed qualitative behavior seen in our data. This particular data set was for a 100 nm VO_2 film on r-cut collected at 405 nm. As this is an LM fit of the data, there is no goodness of fit variable analogous to an R^2 to help us understand quantitatively how good of a fit this is, however we can visually analyze how well the model agrees with the data. We see that the model is good at replicating the broadness and transition temperature seen in the data, as well as the shape in the middle of the transition.

However there is a failure to replicate the curvature at the edges of the transition, suggesting the model does not exactly replicate the switching behavior between monoclinic and rutile phases. Other more complex models, such as modeling the switch using a percolative model, succeed in replicating the end behaviors better for electrical transport, so it is likely that they would also be more successful at replicating the end behaviors for the optical transition as well. However these models also struggle to replicate the end behaviors more than the middle of the transition, testifying to the complexity of the system in these regions.

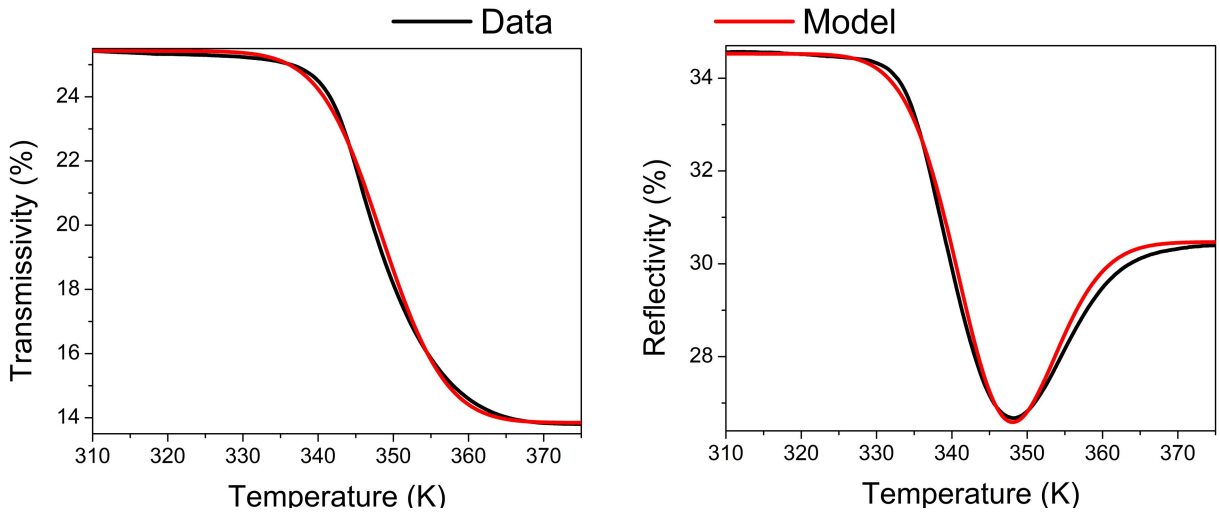

Figure 5.13. Example of a fit of the model to a transmission/reflection data set for a VO_2 film showing a large downward bump at the end of the transition. For the 100 nm film on a-cut with 980 nm light incident. Refractive indices fit to be 1.94 + 0.64j for metallic state and 1.4 + 0.32j for the insulating state. Previous studies have shown a wide spread for both metallic and insulating state n's in the near IR region, from about 1.4-4, so our values are to this range. k is also typically below 1 for both states, consistent with our data.[89,152]

Examining the comparison of the model to data shown in Figure 5.13 for the 100 nm r-cut film with 980 nm light, we see that the model is highly successful in reproducing the bump seen in many of our data sets. For this particular fit, the success of the model in reproducing the features of the data is higher than that seen in many of the more typical data sets. Although it is still possible that some other rarer effects, such as scattering or some anomalous absorption,

could be responsible for the bumps we observed, the fact that our simple model, which didn't take any of these more complicated effects into account, was able to reproduce these features so precisely suggests that the simpler considerations of the model are more likely responsible for these features. A precise explanation for why specific films show the bumps instead of others is actually quite complicated, as it has to do with the intricate algebra and geometric considerations at each layer that we discussed in the previous section. A simplified way to visualize the process is to think of it like a multiple oscillator system, where the phases of the different oscillators can cause constructive or destructive interfere at different times. In our case it is not time but temperature which evolves the state of the system. Why the transmissivity does not show a similar evolution through the transition is also complicated, but has to do with how the phase factors of the two states interact in Equations 5.9 and 5.11.

One of the main differences in fits that include bumps versus fits that do not is that there are large differences from the insulating to metallic state in both real and complex refractive indices. For all samples that do not have bumps, the difference is always less than 0.15 for both real and complex indices, however the difference is usually much greater than this for samples which do have these interference bumps. However the absolute refractive index actually changes very little in comparison to the real and imaginary components individually. Thus the interference in the reflectivity/transmissivity at a certain wavelength is likely to occur in samples which have larger differences in n and k between their two states at that wavelength. From our data this is clearly more likely at 980 nm, so the difference between the two states refractive indices is likely to be much larger in general at these higher wavelengths. As there are no studies which have published seeing this effect in either data or a model, there is no direct comparison we can make to support these conclusions. However it is clear from comparing between previous

studies[89,152,154] that in the near IR range there is a much larger variation in the refractive indices of both the monoclinic and rutile phases for different groups and fabrication conditions, so it seems likely that our specific fabrication process created films which had larger differences between monoclinic and rutile n while other studies did not. This may be why other studies that published their TR data as a function of temperature through the VO_2 transition near this wavelength did not observe these bumps while we did.[89,152,155]

Interestingly, according to the model alone, if all other parameters are kept identical for a given film but the difference between monoclinic and rutile refractive indices is increased, the interference starts to have an even larger effect, causing even more oscillations in the signal to appear in the region of the transition. It is somewhat clear this would happen if we recall how the TR coefficients are ultimately determined by sinusoidal functions of the complex refractive index, therefore large phase changes gives us a larger window into the oscillatory nature of these properties. Another difference that was seen between fits of samples where this interference was observed versus those where it was not observed, was that the real refractive index was always higher in the insulating state while the imaginary refractive index always lower in the insulating state. For samples without the bumps, the refractive indices in the insulating state were either both higher than the metallic state, both lower than the metallic state, or there was only a very small difference between metallic and insulating state indices. Why this difference exists is not apparently clear, as it is totally possible, according to our model, for interference effects to appear outside of this trend, as long as the differences between either the real indices of refraction or the imaginary indices of refraction are large enough.

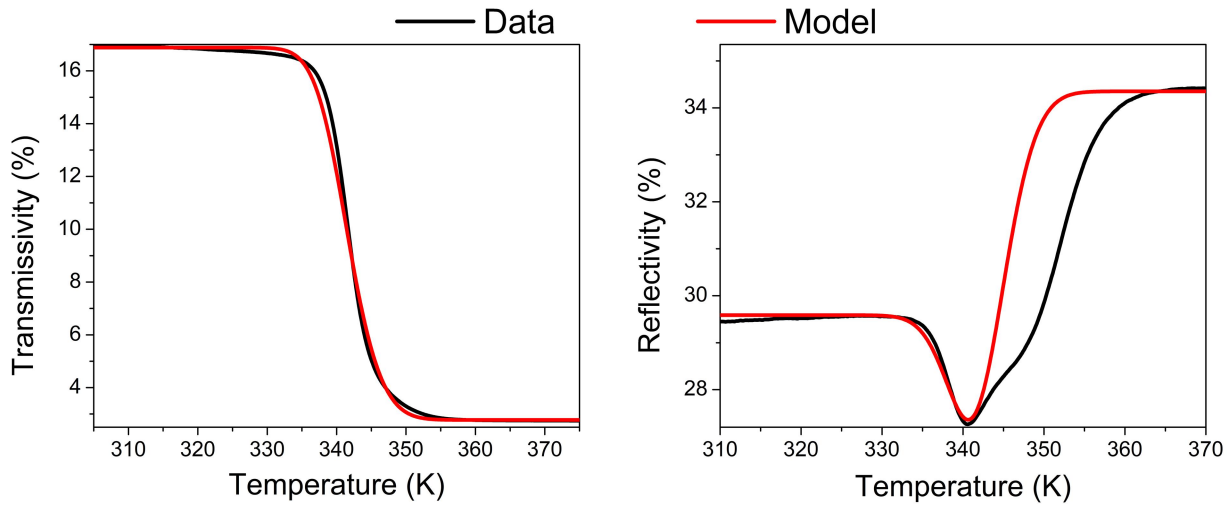

Figure 5.14. Example of a fit of the model to a transmission/reflection data set for the VO_2 film showing anomalous behavior at transition. For the 200 nm film on r-cut with 980 nm light incident. Refractive indices fit to be 1.58 + 0.65j for metallic state and 1.72 + 0.25j for the insulating state.

The model was also able to successfully reproduce all of the different types of switching behavior. The conditions for the different type of switching are also determined by the complicated algebra that is responsible for the appearance of the bumps, and it is also a very complex interplay between the thickness, wavelength, and refractive indices that ultimately determines the switching. Roughness makes this determination even more difficult, as the roughness layer seems to have a moderate effect on the likelihood of different switching behaviors. However it is a bit more algebraically obvious in this case why the different behaviors we observed might occur. We see that the different type of switching behavior of the transmission is ultimately determined by the denominator in Equation 5.11, as the numerator does not change through the transition. So if the denominator becomes larger through the transition, the transmission will decrease, whereas if the denominator decreases the transmission will decrease. We see from Table 5.2 that the refractive index will always decrease for the samples with an increase in transmissivity, consistent with what we would expect. However

many samples with a decrease also have a decrease in the refractive indices, albeit the decrease tended to be much smaller. This is due to the fact that both the thickness and the wavelength have a weighted effect on how much a change in index will cause changes in the denominator in a positive or negative manner, so thicker films collected at higher wavelengths tend to have negative switching in the transmission rather than positive switching.

For the anomalous sample that was previously discussed in section 5.2, which both had an apparent double switching event and was the only sample which showed an increase in reflectivity at the transition, the model was only able to partially replicate the qualitative behavior observed. We see in Figure 5.14 that the model of the transmissivity alone is a good fit of the data. The reflectivity also shows good fitting for the first half of the transition, even replicating the downward bump at the beginning. However the apparent double switching behavior was not able to be replicated, and would most likely require some modification of the model to account for a secondary transition. Thus the model cannot help explain why this sample showed this anomalous behavior in the reflectivity. And yet the upward switching was very easy to reproduce, as theoretically if the samples go from a lower absolute index to a higher one there should be an increase in reflectivity. How much larger the change has to be to have an increase in the reflectivity is determined by the roughness, the thickness, and the wavelength in a similar manner to the switching behaviors described above.

Attenuation for all of the fits was always less than 2%, small in comparison to the reflectivity for all samples. The initial beam intensity's attenuation through the setup without a sample present is already accounted for, and therefore the attenuation determined by the model is mainly representative of the diffuse reflections that occurred in the system. Thus the

contributions of diffuse reflectivity are small, as we had already assumed in our model given the low roughness of our films.

Table 5.2. Overview of fitted indices of refraction for both the monoclinic and rutile phases of our samples at each wavelength. The first two columns describe the substrate and thicknesses, while the real and imaginary components of the refractive indices are separated into separate columns. These columns are separated into different crystal states and wavelengths.

Substrate	Thickness (nm)	Wavelength											
		405 nm				635 nm				980 nm			
		Monoclinic		Rutile		Monoclinic		Rutile		Monoclinic		Rutile	
		n	k	n	k	n	k	n	k	n	k	n	k
c-cut	200	-	-	-	-	-	-	-	-	1.82	0.28	1.53	0.65
	100	-	-	-	-	-	-	-	-	2.48	0.24	2.11	0.71
	50	-	-	-	-	2.09	0.21	1.96	0.24	3.35	0.16	2.88	0.42
r-cut	200	-	-	-	-	-	-	-	-	1.72	0.25	1.58	0.65
	100	1.94	0.37	2	0.38	1.55	0.35	1.4	0.46	2.52	0.15	2.13	0.47
	50	1.55	0.58	1.51	0.54	2.1	0.14	1.98	0.16	-	-	-	-
a-cut	100	-	-	-	-	1.53	0.2	1.49	0.26	1.42	0.32	1.95	0.64
	50	-	-	-	-	2.14	0.18	1.99	0.23	2.68	0.17	2.58	0.42

There is one other concern about the accuracy of the model beyond those already described above, and that is the lack of clear trend in the refractive indices between films with different thicknesses. Based on all previous studies results, a lack of clear trend is expected when comparing the refractive indices of different wavelength, as VO_2's refractive index varies largely with wavelength. However, assuming all other fabrication parameters are the same, we would expect the different thickness films to have similar refractive indices for a single wavelength in their respective monoclinic and rutile states. It is possible that the way the roughness is treated in the model simply is not sufficient for our films, which can also have oxidation layers and other

surface impurities. However it could also be due to the different crystalline quality at different thicknesses, as the films are more stressed the closer they are to the substrate interface. Previous studies did find that the optical properties are extremely sensitive to fabrication conditions,[89,152,154] therefore this is not an unlikely explanation. The fact that the fits for films of the same thickness but deposited onto different substrates showed less than 10% differences in the real indices of refraction for both the metallic and insulating states would also seem to suggest that it is less likely to be purely due to surface impurities, as the films for different substrates show such different surface morphology.

5.5 Conclusions

Sputtered VO_2 films of various thicknesses on various substrates were fabricated to determine the difference in their optical properties. The electrical transport across the VO_2 transition was used to confirm the quality of the sputtered films. Electrical transport properties of films deposited on the different substrates only showed minor differences, with the most distinct being that the a-cut sample had a higher temperature and larger hysteresis MIT. The XRD pattern of a c-cut film confirmed the crystallization of VO_2. AFM images were taken, and both roughness and particle size extracted for each film. Films deposited on c-cut were much rougher than those deposited on the other substrates, and thicker films were generally rougher than thinner ones. The transmissivity and reflectivity typically both decreased at the transition, however for many of the thinner films the transmissivity increased instead. Most of the data collected at 980 nm also showed a downward bump at the higher temperature end of the transition. A few films also showed either a downward or upward bump during the transition at other wavelengths. There was no clear trend in the magnitude of the change in either the

transmissivity or the reflectivity that helped explain why certain samples showed larger changes than others.

A model for the reflectivity and transmissivity for the films was developed by combining the representative matrix model and the single layer roughness model, and then modeling the transitional behavior as a Gaussian distribution of monoclinic and rutile grains. This model was then implemented using MATLAB, and fits refined using a Levenberg-Marquardt algorithm. Only 60% of the samples' data was able to be reasonably fit using the developed model, possibly due to both limitations of the model and variations in angle during data collection. The model was able to fit typical data sets well, but was less successful at replicating the end behaviors of the transition than more refined models have demonstrated. The model was also successful in reproducing the bumps seen in many of the data sets, suggesting purely interference is the mechanism behind their appearance. The main distinction between samples that showed these interference effects and those that did not was the magnitude of the change in refractive index from monoclinic to rutile, which was much larger for samples with interference. According to the model, the attenuation was less than 2% for all samples, suggesting scattering was very low as originally assumed.

Chapter 6. Summary

6.1 Summary of Results

In Chapter 3 we discussed studies into the coupling between vanadium oxide compounds and ferromagnetic compounds in various composite mixtures. Ball milling techniques alone did not produce appreciable coupling in the composites, however when combined with sintering showed very promising results which reproduced the coupling effects previously observed in thin films. Although no VO_2 composites with strong coupling were able to be fabricated, V_2O_3 composites were able to be optimized for magnetic changes of over 56%, and the limitations of the fabrication parameters determined.

Chapter 4 went over the development of a sol-gel synthesis technique for VO_2 films, W doping in VO_2 films, and the magnetic properties of Ni deposited on top of these films. Sol-gel synthesized bilayer films were shown to have smaller but comparable magnetic changes to sputtered bilayers, confirming their feasibility for further applications. Doping was shown to be easier and generally more feasible using the sol-gel techniques. Doped bilayers showed a shift in temperature of the magnetic properties comparable to the shift in the MIT already well-known in VO_2 films, opening up the possibility for room temperature applications. The fact that the magnetic properties were also reduced with increased doping strongly suggested that the previously seen reduction in the MIT with increased doping is due to structural effects, not increased carriers as other groups have postulated.

Chapter 5 was a discussion of results seen in optical studies of different VO_2 films, as well as an overview of a model for transmission and reflection of VO_2 films and the results of its

implementation. What was originally thought to be anomalous bumps in some of the data was determined from the model to be due to normal interference effects. Interference effects were only seen in films that had large changes in the refractive index between VO_2's two states. Multiple different qualitative trends were seen for different films at different wavelengths, however the mechanism behind why certain films behaved qualitatively differently was not able to be determined from the model.

6.2 Outlook

There are several questions left open from the research described above that future experimentation could possibly resolve. As we only used a ball milling technique for $VO_2/CoFe_2O_4$ composites, it is ambiguous as to whether or not successful magnetic coupling in this type of composite can be produced if a sintering technique is employed, or whether $CoFe_2O_4$ would degrade too easily for this to be a feasible process. Determining whether other FM and SPT containing compounds could produce similar results in composites is worthwhile, as there are several other candidates that have been proven to be promising in the analogous film systems. Particle size also seems to be a large factor in milling processes in general, but our studies leave open the question as to how exactly different initial and final particle sizes in the different compounds affect the coupling. There are also other types of milling processes that allow for larger environmental control, which may allow for the optimization of this technique. Finally, there are several different sintering atmospheres, such as minute oxygen gas concentrations, which have been shown to reduce vanadium oxide systems to VO_2 in a more controlled manner, so investigating whether these sintering techniques can isolate a VO_2/FM composite with good coupling is a priority for any future fabrication attempts.

Although the sol-gel technique was proven to be effective in producing the first layer for hybrid structures, it still relied on sputtering the FM. Developing a sol-gel technique for the FM layer as well, and determining the extent of the coupling for a resultant heterostructure, could reveal how flexible and scalable the fabrication technique for these hybrid structures is for industrial applications. Why there is an absolute change in resistance for higher doping concentrations, and determining why this was seen and if there is a way to maintain more consistent results, is still a pressing issue. It is also worthwhile to attempt to try to optimize the transition when there are higher doping concentrations, potentially finding ways to degrade the transition less while maintaining higher doping concentrations.

There are a lot of unresolved questions from the study into the optical transition of VO_2. Although we were able to determine some trends in how the qualitative behavior of our reflectivity and transmissivity curves changed with thickness and wavelength, and how the samples with different behaviors showed different relationships with their refractive indices, the actual mechanisms behind the different behaviors were not clearly determined. More in depth XRD measurements, XPS, and TEM studies to correlate with optical measurements may shed light on this question. Improvements to the model could be potentially made by instead modeling the transition using a percolative model, and the fitting of data improved by correlating with the electrical transport properties.

References

[1] Z. Yin, M. Tordjman, Y. Lee, A. Vardi, R. Kalish, and J.A. Alamo, Sci. Adv. **4**, (2018).

[2] Z. Zhong and P. Hansmann, Phys. Rev. B **93**, (2016).

[3] V. Augustyn, J. Mater. Res. **Spec. Iss.**, (2016).

[4] R.I. Zainullina and V. V Ustinov, Physics-Uspekhi **61**, 719 (2018).

[5] G.N. Pirogora, N.M. Panich, R.I. Korosteleva, and Y. V Voronin, Russ. Chem. Bull. **45**, 2525 (1996).

[6] S. Stathopoulos, A. Khiat, M. Trapatseli, S. Cortese, and A. Serb, Sci. Rep. **7**, (2017).

[7] M. Yang, N. Qin, L.Z. Ren, Y.J. Wang, K.G. Yang, F.M. Yu, W.Q. Zhou, M. Meng, S.X. Wu, D.H. Bao, and S.W. Li, J. Phys. D. Appl. Phys. **47**, (2013).

[8] H. Chen and L. Wang, Bellstein J. Nanotechnol. **5**, 696 (2014).

[9] I.H. Lone, J. Aslam, N.R.E. Radwan, A.H. Bashal, A.F.A. Ajlouni, and A. Akhter, Nanoscale Res. Lett. **14**, (2019).

[10] J. Hwang, Magnetoelectric and Multiferroic Properties in Layered 3D Transition Metal Oxides, Florida State University, 2012.

[11] P. Sharma, F. Xiang, D. Shao, D. Zhang, and E.Y. Tsymbal, Sci. Adv. **5**, (2019).

[12] W. Araki, K. Takeda, and Y. Arai, J. Eur. Ceram. Soc. **36**, (2016).

[13] N.F. Mott, Rev. Mod. Phys. **40**, 677 (1968).

[14] B.J. Kim, Y.W. Lee, B.G. Chae, S.J. Yun, S.Y. Oh, H.T. Kim, and Y.S. Lim, Appl. Phys. Lett. (2007).

[15] F. Hong, B. Yue, N. Hirao, Z. Liu, and B. Chen, Sci. Rep. **7**, (2017).

[16] M. Amer and P. Boutinaud, Phys. Chem. Chem. Phys. **19**, 2591 (2017).

[17] J.H. Lee, W.S. Choi, H. Jeen, H. Lee, J.H. Seo, J. Nam, and M.S. Yeom, Sci. Rep. **7**, (2017).

[18] S.G. Ovchinnikov, J. Magn. Magn. Mater. **300**, 243 (2006).

[19] A. Chernyshov, M. Overby, X. Liu, J.K. Furdyna, Y. Lyanda-Geller, and L.P. Rokhinson, Nat. Phys. **5**, 656 (2009).

[20] D. Chiba, F. Matsukura, and H. Ohno, Appl. Phys. Lett. **89**, 0 (2006).

[21] C.A.F. Vaz, J. Phys. Condens. Matter **24**, 333201 (2012).

[22] L. Berger, Phys. Rev. B **54**, 9353 (1996).

[23] J.C. Slonczewski, J. Magn. Magn. Mater. **159**, L1 (1996).

[24] M. Tsoi, A.G.M. Jansen, J. Bass, W.-C. Chiang, M. Seck, V. Tsoi, and P. Wyder, Phys. Rev. Lett. **80**, 4281 (1998).

[25] A. Kirilyuk, A. V Kimel, and T. Rasing, Rev. Mod. Phys. **88**, 39904 (2016).

[26] V. Peña, T. Gredig, J. Santamaria, and I.K. Schuller, Phys. Rev. Lett. **97**, 1 (2006).

[27] S.P. Bennett, A.T. Wong, A. Glavic, A. Herklotz, C. Urban, I. Valmianski, M.D. Biegalski, H.M. Christen, T.Z. Ward, and V. Lauter, Sci. Rep. **6**, 22708 (2016).

[28] S. Sahoo, Phys. Rev. B **76**, (2007).

[29] I.O. Livares, L.S. Ánchez, J.P. Arra, R.L. Arrea, A.G. Riol, M.M. Enghini, P. Omm, L. Ang, B. Ilzen, J. Eo, J. Ocquet, P. Ablo, and S. Anchis, Opt. Express **26**, (2018).

[30] P. Markov, R.E. Marvel, H.J. Conley, K.J. Miller, R.F. Haglund, and S.M. Weiss, ACS Photonics **2**, 1175 (2015).

[31] J. Guo, H. Zhou, J. Wang, W. Liu, and M. Cheng, Artif. Cells, Nanomedicine, Biotechnol. **46**, 58 (2018).

[32] J. Wang, H. Zhou, G. Guo, T. Cheng, X. Peng, X. Mao, J. Li, and X. Zhang, Int. J. Nanomedicine **12**, 3121 (2017).

[33] D. Eden, (1981).

[34] B. Wang, N. Li, J. Lai, W. Xie, S. Wang, S. Wang, J. Su, E. Cai, and Z. Chi, in *Int. Photonics Optoelectron. Meet.* (Optical Society of America, Wuhan, 2018), p. OT4A.58.

[35] N. Inomata, L. Pan, M. Toda, and T. Ono, in *2016 IEEE 29th Int. Conf. Micro Electro Mech. Syst.* (2016), pp. 1042–1045.

[36] M.A. Baqir and P.K. Choudhury, J. Opt. Soc. Am. B **36**, F123 (2019).

[37] C.H. Griffiths and H.K. Eastwood, J. Appl. Phys. (1974).

[38] A. Magnéli, Acta Chem. Scand. **2**, 501 (1948).

[39] S. Andersson and L. Jahnberg, Ark. Kemi **21**, 1963 (n.d.).

[40] H.A. Wriedt, Bull. Alloy Phase Diagrams (1989).

[41] U. Schwingenschlögl and V. Eyert, Ann. Phys. **13**, 475 (2004).

[42] A.D. Wadsley, Acta Crystallogr. **10**, 261 (1957).

[43] S. Kachi, K. Kosuge, and H. Okinaka, J. Solid State Chem. (1973).

[44] J.R. Gannon and R.J.D. Tilley, J. Solid State Chem. (1978).

[45] F.J. Morin, Phys. Rev. Lett. **3**, 34 (1959).

[46] Z. Yang, C. Ko, and S. Ramanathan, Annu. Rev. Mater. Res. (2011).

[47] A. Pergament, G. Stefanovich, and A. Velichko, J. Sel. Top. Nano Electron. Comput. (2014).

[48] A.L. Pergament, G.B. Stefanovich, A.A. Velichko, and S.D. Khanin, Condens. Matter Lead. Edge 1 (2007).

[49] J. Lauzier, Studies of Tuning Magnetic Properties of Ferromagnetic Heterostructures, Colorado State University, 2020.

[50] R.E. Word, S.A. Werner, W.B. Yelon, J.M. Honig, and S. Shivashankar, Phys. Rev. B **23**, 3533 (1981).

[51] J. De La Venta, S. Wang, T. Saerbeck, J.G. Ramírez, I. Valmianski, and I.K. Schuller, Appl. Phys. Lett. **104**, (2014).

[52] R.M. Moon, J. Appl. Phys. **41**, 883 (1970).

[53] N.B. Aetukuri, A.X. Gray, M. Drouard, M. Cossale, L. Gao, A.H. Reid, R. Kukreja, H. Ohldag, C.A. Jenkins, E. Arenholz, K.P. Roche, H.A. Dürr, M.G. Samant, and S.S.P. Parkin, Nat. Phys. (2013).

[54] P. Hansmann, A. Toschi, G. Sangiovanni, T. Saha-Dasgupta, S. Lupi, M. Marsi, and K. Held, Phys. Status Solidi **250**, 1251 (2013).

[55] M. Imada, A. Fujimori, and Y. Tokura, Rev. Mod. Phys. **70**, 1039 (1998).

[56] A. Tanaka, J. Phys. Soc. Japan **71**, 1091 (2002).

[57] I. Lo Vecchio, J.D. Denlinger, O. Krupin, B.J. Kim, P.A. Metcalf, S. Lupi, J.W. Allen, and A. Lanzara, Phys. Rev. Lett. **117**, (2016).

[58] F. Grandi, A. Amaricci, and M. Fabrizio, Phys. Rev. Res. **2**, (2019).

[59] T. Driscoll, H.T. Kim, B.G. Chae, B.J. Kim, Y.W. Lee, N.M. Jokerst, S. Palit, D.R. Smith, M. Di Ventra, and D.N. Basov, Science (80-.). (2009).

[60] M.J. Dicken, K. Aydin, I.M. Pryce, L.A. Sweatlock, E.M. Boyd, S. Walavalkar, J. Ma, and H.A. Atwater, Opt. Express (2009).

[61] D. Ruzmetov, G. Gopalakrishnan, C. Ko, V. Narayanamurti, and S. Ramanathan, J. Appl. Phys. (2010).

[62] H.T. Kim, B.J. Kim, S. Choi, B.G. Chae, Y.W. Lee, T. Driscoll, M.M. Qazilbash, and D.N. Basov, J. Appl. Phys. (2010).

[63] E. Strelcov, Y. Lilach, and A. Kolmakov, Nano Lett. (2009).

[64] J.M. Baik, M.H. Kim, C. Larson, C.T. Yavuz, G.D. Stucky, A.M. Wodtke, and M. Moskovits, Nano Lett. (2009).

[65] T.C. Chang, X. Cao, S.H. Bao, S.D. Ji, H.J. Luo, and P. Jin, Adv. Manuf. (2018).

[66] A. Cavalleri, C. Tóth, C.W. Siders, J.A. Squier, F. Ráksi, P. Forget, and J.C. Kieffer, Phys. Rev. Lett. **87**, 237401 (2001).

[67] G. Stefanovich, A. Pergament, and D. Stefanovich, J. Phys. Condens. Matter **12**, 8837 (2000).

[68] J. Cao, E. Ertekin, V. Srinivasan, W. Fan, S. Huang, H. Zheng, J.W.L. Yim, D.R. Khanal, D.F.

Ogletree, J.C. Grossman, and J. Wu, Nat. Nanotechnol. (2009).

[69] T. Kikuzuki and M. Lippmaa, Appl. Phys. Lett. (2010).

[70] P. Baum, D.-S. Yang, and A.H. Zewail, Science (80-.). **318**, 788 LP (2007).

[71] T.M. Rice, H. Launois, and J.P. Pouget, Phys. Rev. Lett. (1994).

[72] R.E. Peierls, *Quantum Theory of Solids* (Oxford University Press, Oxford, 2001).

[73] G. Grüner, Rev. Mod. Phys. **60**, 1129 (1988).

[74] H.W. Verleur, A.S. Barker Jr., and C.N. Berglund, Phys. Rev. **172**, (1968).

[75] S. Shin, S. Suga, M. Taniguchi, M. Fujisawa, H. Kanzaki, A. Fujimori, H. Daimon, Y. Ueda, K. Kosuge, and S. Kachi, Phys. Rev. B (1990).

[76] J.P. Pouget, H. Launois, T.M. Rice, P. Dernier, A. Gossard, G. Villeneuve, and P. Hagenmuller, Phys. Rev. B **10**, 1801 (1974).

[77] E. Abreu, M. Liu, J. Lu, K.G. West, S. Kittiwatanakul, W. Yin, S.A. Wolf, and R.D. Averitt, New J. Phys. **14**, 1 (2012).

[78] M. Liu, H.Y. Hwang, H. Tao, A.C. Strikwerda, K. Fan, G.R. Keiser, A.J. Sternbach, K.G. West, S. Kittiwatanakul, J. Lu, S.A. Wolf, F.G. Omenetto, X. Zhang, K.A. Nelson, and R.D. Averitt, Nature **487**, 345 (2012).

[79] J.B. Goodenough, J. Solid State Chem. **3**, 490 (1971).

[80] C.J. Hearn, J. Phys. C Solid State Phys. (1972).

[81] S. Biermann, A. Poteryaev, A.I. Lichtenstein, and A. Georges, Phys. Rev. Lett. **94**, 26404 (2005).

[82] C. Weber, D.D. O'Regan, N.D.M. Hine, M.C. Payne, G. Kotliar, and P.B. Littlewood, Phys. Rev. Lett. **108**, 256402 (2012).

[83] S. Xu, X. Shen, K.A. Hallman, R.F. Haglund, and S.T. Pantelides, Phys. Rev. B (2017).

[84] J. Laverock, A.R.H. Preston, D. Newby, K.E. Smith, S. Sallis, L.F.J. Piper, S. Kittiwatanakul, J.W. Lu, S.A. Wolf, M. Leandersson, and T. Balasubramanian, Phys. Rev. B **86**, 195124 (2012).

[85] M.E.A. Warwick and R. Binions, J. Mater. Chem. A **2**, 3275 (2014).

[86] J.D. Ryckman, V. Diez-Blanco, J. Nag, R.E. Marvel, B.K. Choi, R.F. Haglund, and S.M. Weiss, Opt. Express **20**, 13215 (2012).

[87] K.J. Miller, R.F. Haglund, and S.M. Weiss, Opt. Mater. Express **8**, 2415 (2018).

[88] H. Fujiwara, *Spectroscopic Ellipsometry Principles and Applications* (2003).

[89] C. Wan, Z. Zhang, D. Woolf, C.M. Hessel, J. Rensberg, J.M. Hensley, Y. Xiao, A. Shahsafi, J. Salman, S. Richter, Y. Sun, M.M. Qazilbash, R. Schmidt-Grund, C. Ronning, S. Ramanathan, and M.A. Kats, Ann. Phys. **531**, (2019).

[90] Y. Muraoka and Z. Hiroi, Appl. Phys. Lett. **80**, 583 (2002).

[91] G. V Jorgenson and J.C. Lee, Sol. Energy Mater. **14**, 205 (1986).

[92] X. Tan, T. Yao, R. Long, Z. Sun, Y. Feng, H. Cheng, X. Yuan, W. Zhang, Q. Liu, C. Wu, Y. Xie, and S. Wei, Sci. Rep. **2**, 1 (2012).

[93] J.M. Reyes, M. Sayer, and R. Chen, Can. J. Phys. **54**, 408 (1975).

[94] Z.P. Wu, A. Miyashita, S. Yamamoto, H. Abe, I. Nashiyama, K. Narumi, and H. Naramoto, J. Appl. Phys. **86**, 5311 (1999).

[95] J.M. Booth and P.S. Casey, Phys. Rev. Lett. **103**, (2009).

[96] C. Tang, P. Georgopoulos, M.E. Fine, J.B. Cohen, M. Nygren, G.S. Knapp, and A. Aldred, Phys. Rev. B **31**, 1000 (1985).

[97] L. Whittaker, T.-L. Wu, C.J. Patridge, G. Sambandamurthy, and S. Banerjee, J. Mater. Chem. **21**, 5580 (2011).

[98] T. Yao, X. Zhang, Z. Sun, S. Liu, Y. Huang, Y. Xie, C. Wu, X. Yuan, W. Zhang, Z. Wu, G. Pan, F. Hu, L. Wu, Q. Liu, and S. Wei, Phys. Rev. Lett. **105**, 226405 (2010).

[99] A. Di Cicco, A. Congeduti, F. Coppari, J.C. Chervin, F. Baudelet, and A. Polian, Phys. Rev. B **78**, 33309 (2008).

[100] A. Romanyuk, R. Steiner, L. Marot, and P. Oelhafen, Sol. Energy Mater. Sol. Cells **91**, 1831 (2007).

[101] J. Okabayashi, Y. Miura, and T. Taniyama, Npj Quantum Mater. **4**, (2019).

[102] V. Nguyen, A. Ahmed, and R. Ramanujan, Adv. Mater. **24**, 4041 (2012).

[103] P. Manchanda, U. Singh, S. Adenwalla, and A. Kashyap, IEEE Trans. Magn. **50**, (2014).

[104] J. Hu, T. Yang, and L. Chen, Npj Comput. Mater. **62**, (2018).

[105] J. De La Venta, S. Wang, J.G. Ramirez, and I.K. Schuller, Appl. Phys. Lett. **102**, 10 (2013).

[106] J. Lauzier, L. Sutton, and J. de la Venta, J. Phys. Condens. Matter **30**, (2018).

[107] T. Saerbeck, J. de la Venta, S. Wang, J.G. Ramírez, M. Erekhinsky, I. Valmianski, and I.K. Schuller, J. Mater. Res. **29**, 2353 (2014).

[108] J. Lauzier, L. Sutton, and J. de la Venta, J. Appl. Phys. **122**, (2017).

[109] C. Urban, A. Quesada, T. Saerbeck, M.A. Garcia, M.A. De La Rubia, I. Valmianski, J.F. Fernández, and I.K. Schuller, Appl. Phys. Lett. **109**, (2016).

[110] J. Cai, F. Jelezko, and M.B. Plenio, Nat. Commun. **5**, (2014).

[111] J. Huang, R.C. O'Handley, and D. Bono, in *Proc.SPIE* (2003).

[112] F. Souza Jr, J. Marins, J. Pinto, G. Oliveira, C. Rodrigues, and L.M. Lima, J. Mater. Sci. **45**, 5012 (2010).

[113] L. Ferraris, F. Franchini, and E. Pošković, in *2016 IEEE Sensors Appl. Symp.* (2016), pp. 1–6.

[114] J. Lyubina, J. Phys. D. Appl. Phys. **50**, 53002 (2017).

[115] M. V Efremova, Y.A. Nalench, E. Myrovali, A.S. Garanina, I.S. Grebennikov, P.K. Gifer, M.A. Abakumov, M. Spasova, M. Angelakeris, A.G. Savchenko, M. Farle, N.L. Klyachko, A.G. Majouga, and U. Wiedwald, Beilstein J. Nanotechnol. **9**, 2684 (2018).

[116] M. Suresh, C. Anand, J.E. Frith, D.S. Dhawale, V.P. Subramaniam, E. Strounina, C.I. Sathish, K. Yamaura, J.J. Cooper-White, and A. Vinu, Sci. Rep. **6**, 21820 (2016).

[117] G. Engdahl, *Handbook of Giant Magnetostrictive Materials* (2000).

[118] B.D. Cullity and C.D. Graham, *Introduction to Magnetic Materials (2nd Edition)* (John Wiley and Sons, Hoboken, New Jersey, 2008).

[119] S. Guan, A. Rougier, O. Viraphong, D. Denux, N. Penin, and M. Gaudon, Inorg. Chem. **57**, 8857 (2018).

[120] T.G. Durai, K. Das, and S. Das, J. Nanosci. Nanotechnol. **7**, 1980 (2007).

[121] J.-H. Son, J. Wei, D. Cobden, G. Cao, and Y. Xia, Chem. Mater. **22**, 3043 (2010).

[122] P.A. Metcalf, S. Guha, L.P. Gonzalez, J.O. Barnes, E.B. Slamovich, and J.M. Honig, Thin Solid Films **515**, 3421 (207AD).

[123] C.B. Greenberg, Thin Solid Films (1983).

[124] E.N. Fuls, D.H. Hensler, and A.R. Ross, Appl. Phys. Lett. (1967).

[125] M. Borek, F. Qian, V. Nagabushnam, and R.K. Singh, Appl. Phys. Lett. (1993).

[126] S. Koide and H. Takei, J. Phys. Soc. Japan (1967).

[127] C.A.R. A. J. Lynch, *The History of Grinding* (2005).

[128] P. Khadka, J. Ro, H. Kim, I. Kim, J.T. Kim, H. Kim, J.M. Cho, G. Yun, and J. Lee, Asian J. Pharm. Sci. **9**, 304 (2014).

[129] A. Yahia, A. Attaf, H. Saidi, M. Dahnoun, C. Khelifi, A. Bouhdjer, A. Saadi, and H. Ezzaouia, Surfaces and Interfaces **14**, 158 (2019).

[130] S. Kim, A. Lipson, G.H. Miley, and R. Engineering, in *ICCR 9* (2002).

[131] S. F.M, Bell Syst. Tech. J. 711 (1958).

[132] P.J. Severin, Philips Res. Reports **26**, 279 (1971).

[133] L.J. Swartzendruber, Natl. Bur. Stand. 1 (1964).

[134] D. Ruzmetov, K.T. Zawilski, V. Narayanamurti, and S. Ramanathan, J. Appl. Phys. (2007).

[135] C. Ko and S. Ramanathan, J. Appl. Phys. **104**, 086105 (2008).

[136] M. Abdullah, J. Nano. Nanotech. **1**, 28 (2008).

[137] A.L. Patterson, Phys. Rev. **56**, 978 (1939).

[138] G. Zeng, Y. Duan, F. Besenbacher, and M. Dong, in *At. Force Microsc. Investig. into Biol. -*

From Cell to Protein (2012).

[139] P.G. Klemens, Int. J. Thermophys. **9**, 171 (1988).

[140] B.G. Chae and H.T. Kim, Phys. B Phys. Condens. Matter **405**, 663 (2010).

[141] M. Hada, K. Okimura, and J. Matsuo, Phys. Rev. B - Condens. Matter Mater. Phys. **82**, 2 (2010).

[142] M. Benkahoul, M. Chaker, J. Margot, E. Haddad, R. Kruzelecky, B. Wong, W. Jamroz, and P. Poinas, Sol. Energy Mater. Sol. Cells **95**, 3504 (2011).

[143] F. Guinneton, L. Sauques, J.-C. Valmalette, F. Cros, and J.-R. Gavarri, Thin Solid Films **446**, 287 (2004).

[144] M. Soltani, M. Chaker, E. Haddad, R. V Kruzelecky, and D. Nikanpour, J. Vac. Sci. Technol. A **22**, 859 (2004).

[145] Y. Zhao, J. Hwan Lee, Y. Zhu, M. Nazari, C. Chen, H. Wang, A. Bernussi, M. Holtz, and Z. Fan, J. Appl. Phys. **111**, 53533 (2012).

[146] J. Jian, A. Chen, Y. Chen, X. Zhang, and H. Wang, Appl. Phys. Lett. **111**, 153102 (2017).

[147] K. Pascoe, *Reflectivity and Transmissivity through Layered , Lossy Media : A User-Friendly Approach* (2001).

[148] C.K. Carniglia and D.G. Jensen, Appl. Opt. **41**, 3167 (2002).

[149] C.K. Carniglia and D.G. Jensen, in *Opt. Interf. Coatings* (Optical Society of America, Banff, 2001), p. TuB5.

[150] J.A. Holzer and C.C. Sung, J. Appl. Phys. **49**, 1002 (1978).

[151] Shawn Divitt, (2020).

[152] M. Currie, M.A. Mastro, and V.D. Wheeler, Opt. Mater. Express **7**, 1697 (2017).

[153] H.M. Pinto, R. Binions, Q. Mary, C. Piccirillo, and I. National, Mater. Sci. Forum **587**–**588**, 640 (2008).

[154] J.F. De Natale, P.J. Hood, and A.B. Harker, J. Appl. Phys. **66**, 5844 (1989).

[155] M. Currie, M.A. Mastro, and V.D. Wheeler, J. Vis. Exp. 1 (2018).

[156] L. Sutton, J. Lauzier, and J. de la Venta, J. Appl. Phys. **123**, 83902 (2018).

[157] L. Sutton, A. Blehm, J. Lauzier, K. Malone, G. Smith, M. Singh, and J. de la Venta, J. Supercond. Nov. Magn. **33**, 2493 (2020).

Appendix

The following is the main MATLAB code used for fitting the TR data collected in section 5.2, as well as outputting the fit and a model of T and R, and plotting against input data:

```
% Fitting algorithm for transmission/reflection data of VO2 across the
% transition
% Uses a nonlinear least squares (Levenburg-Marquard) algorithm to
% simultaneously fit T and R
% requires 3 functions - singlepointTR.m, Tmodel3_morphologyFunction_nohysteresis.m, and
Tmodel3_morphologyFunction_nohysteresiswAbsout.m

% clears variables and closes programs
clear all;
close all;

% open file and make temperature and TR arrays
t = readtable('VO456_635nm_heat.dat', 'ReadVariableNames', false);
A = table2array(t);
B = str2double(A);
B(1,:) = [];
Temp = B(:,1);
TR = B(:,2:3);

% substrate properties
saph_t = 500000;
saph_405_s = 1.788;
saph_405_p = 1.783;
saph_635_s = 1.765;
saph_635_p = 1.757;
saph_980_s = 1.756;
saph_980_p = 1.820;

% wavelengths
lambda_blue = 405;
lambda_red = 635;
lambda_infrared = 980;

% known film properties
t = 50; % thickness
hysteresis = 10;
roughness = 0.39;

% thickness of effective roughness single layer
d_eff = 2*roughness;

% defines other set parameters
y_sub = saph_635_s; % substrate medium admittance
```

```
lambda = lambda_red;

% film parameters for fitting
% transition parameters
T_t = 340.2; % transition temperature
W = 9; % transition width

% defines real and imaginary refractive indices for the insulating and
% metallic states
n_ins = 2.14;
k_ins = 0.18;
n_met = 1.99;
k_met = 0.23;

% unnacounted for loss
loss = 1.12;

theta = 20; % in degree

% thickness array of layers
d = [NaN, d_eff, t, saph_t, NaN];

% consolidate fitting parameters
fitparams1 = [T_t, W, n_ins, k_ins, n_met, k_met, loss, theta];
lb = [T_t, W, n_ins, k_ins, n_met, k_met,  loss, theta];
ub = [T_t, W, n_ins, k_ins, n_met, k_met,  loss, theta];

% define function handle for difference model
fitfun1 = @(fitparams1) Tmodel3_morphologyFunction_nohysteresis(fitparams1(1), fitparams1(2),
fitparams1(3), fitparams1(4), fitparams1(5), fitparams1(6), fitparams1(7), lambda, fitparams1(8), d_eff,
y_sub, d, Temp)-TR;

% fit options
options = optimoptions(@lsqnonlin, 'Algorithm', 'trust-region-reflective', 'MaxFunctionEvaluations',
100000, 'FiniteDifferenceStepSize', .0001, "StepTolerance", 1e-6);

% least squares fit
fit1 = lsqnonlin(fitfun1, fitparams1, lb, ub, options);

% build data points for fit
[transmission, reflection, absorption] = Tmodel3_morphologyFunction_nohysteresiswAbsout(fit1(1),
fit1(2), fit1(3), fit1(4), fit1(5), fit1(6), fit1(7), lambda, fit1(8), d_eff, y_sub, d, Temp);

% output data and fit
datafile = fopen('fitdata_VO556.txt','a');
fitfile = fopen('fit_VO556.txt','a');

fprintf(datafile, '%s\n\n', datetime);
fprintf(datafile, 'Temperature\tTransmission\tReflection\tAbsorption\n');
fprintf(datafile, '%d\t%d\t%d\t%d', [Temp, TR]);
fprintf(datafile, '\n\n');

fprintf(fitfile, '%s\n\n', datetime);
fprintf(fitfile, 'Best Fit: T_t = %d\nW = %d\nn_ins = %d\nk_ins = %d\nn_met = %d\nk_met = %d\nloss =
%d\ntheta = %d\n', fit1(1), fit1(2), fit1(3), fit1(4), fit1(5), fit1(6), fit1(7), fit1(8));
```

```
% plot the result against actual data
figure(1)
plot(Temp, TR(:,1))
hold on
plot(Temp, transmission)
title('Comparison of Transmission Model vs. Data');
xlabel('Temperature');
ylabel('Transmittance(%)');
legend({'data', 'model'},'Location','southwest')
hold off
grid

figure(2)
plot(Temp, TR(:,2))
hold on
plot(Temp, reflection)
title('Comparison of Reflection Model vs. Data');
xlabel('Temperature');
ylabel('Reflectance(%)');
legend({'data', 'model'},'Location','southwest')
hold off
grid

% plot full fit together
figure(3)
plot(Temp, transmission)
hold on
plot(Temp, reflection)
plot(Temp, absorption)
title('Comparison of RTA');
xlabel('Temperature');
ylabel('Transmittance(%)');
legend({'transmission', 'reflection', 'absorption'},'Location','southwest')
hold off
grid

% closes all files
fclose('all');
```

Initialization of fit parameters and their ranges need to be modified based on individual datasets; the tolerance values and fitting style may need to be varied as well. Data needs to be smoothed for optimal results, and separated into three tabulated columns (Temperature, Transmission, Reflection). Known film properties must be modified to correct values. The dependent function Tmodel3_morphologyFunction_nohysteresis.m, which defines the film system and creates a temperature variance for the admittance based on VO_2, is given below:

```
% Modelling only admittance assuming totally spectral reflection/transmission
```

```
% VO2 T dependence included
% absorption and attenuation added

clear all;
close all;

um = 1e-6;
nm = 1e-9;

%substrate
saph_t = 500000;
saph_405_s = 1.788;
saph_405_p = 1.783;
saph_635_s = 1.765;
saph_635_p = 1.757;
saph_980_s = 1.756;
saph_980_p = 1.820;

lambda_blue = 405;
lambda_red = 635;
lambda_infrared = 980;

% film properties
t = 50; %thicknress
T_t = 340.7260; %transition temperature
W = 8.8; %transition width
hysteresis = 10;
roughness = 0.4;

% define admittance for medium
n_ins = 2.09;
k_ins = 0.21;
n_met = 1.94;
k_met = 0.22;

y_VO2_ins = n_ins + k_ins*1i;
y_VO2_met = n_met + k_met*1i;

% define thin film structure
y_inc = 1; % incident medium admittance
y_sub = saph_635_s; % substrate medium admittance
theta = 20; % in degree
lambda = lambda_red;

%rmorphology add in
n_eff_ins = sqrt((n_ins^2 + 1)/2);
n_eff_met = sqrt((n_met^2 + 1)/2);
d_eff = 2*roughness;
k_eff_ins = (pi*((n_ins - 1)^2)*(n_ins + 1)*d_eff)/(4*n_eff_ins*lambda);
k_eff_met = (pi*((n_met - 1)^2)*(n_met + 1)*d_eff)/(4*n_eff_met*lambda);
y_eff_ins = n_eff_ins + k_eff_ins*1i;
y_eff_met = n_eff_met + k_eff_met*1i;

d = [NaN, d_eff, t, saph_t, NaN];

loss = 0;
```

```
%temperature range initialization
T_step = 0.1;
T_i = 300;
T_f = 400;
Tlength = (T_f - T_i)/T_step;

%memory allocation of output
r = zeros(Tlength,1);
t = zeros(Tlength,1);
R = zeros(Tlength,1);
T = zeros(Tlength,1);
A = zeros(Tlength,1);
Temp = zeros(1,Tlength);

Temp(1) = T_i;
for ii=1:Tlength
    y = [1, y_Tmodel(Temp(ii), T_t, W, y_eff_ins, y_eff_met), y_Tmodel(Temp(ii), T_t, W, y_VO2_ins,
y_VO2_met), y_sub, 1];
    [r(ii), t(ii), R(ii), T(ii), A(ii)] = singlepointTR(lambda, d, y, theta, 0);

    if ii ~= Tlength
        Temp(ii+1) = Temp(ii) + T_step;
    end

end

reflection = R*100-loss;
transmission = T*100-loss;
absorption = A*100-loss;

%plot the result
figure, plot(Temp,transmission);
hold on;
plot(Temp,reflection);
plot(Temp,absorption);
title('VO2 T and R');
xlabel('Temperature');
ylabel('Transmittance(%)');
legend({'transmission', 'reflection', 'absorption'},'Location','southwest')
grid on;

function [y_tmodel] = y_Tmodel(temp, T_t, W, y_VO2_ins, y_VO2_met)
    TD = (erf((temp-T_t)/(sqrt(2)*W))+1)/2;
    y_tmodel = (1-TD)*y_VO2_ins + TD*y_VO2_met;
end
```

The other dependent function, Tmodel3_morphologyFunction_nohysteresiswAbsout.m, is simply a modified version of this one, and is only modified so that it has the correct outputs to make plots with the model. The dependent function of this code is singlepointTR.m, which

calculates R, T, and A for a single temperature point. This is simply a slightly modified version of jreftran.m, and will be omitted here as it has been published by the author.[151]